Klaus Lang, Dipl.-Ing. BSc

Design of IM and SynRM machine based actuators for elevated temperature environments

DISSERTATION

zur Erlangung des akademischen Grades eines
Doktors der technischen Wissenschaften

eingereicht an der

Technischen Universität Graz

Betreuerin:
Univ.-Prof. Dr.-Ing. Annette Mütze
Institut für Elektrische Antriebstechnik und Maschinen
Technische Universität Graz

in Kooperation mit Kristl, Seibt & Co GmbH.

2015

for my parents

AFFIDAVIT

I declare that I have authored this thesis independently, that I have not used other than the declared sources/resources, and that I have explicitly indicated all material which has been quoted either literally or by content from the sources used. The text document uploaded to TUGRAZonline is identical to the present doctoral thesis.

Date

Signature

Contents

Table of contents i

Abstract iii

Zusammenfassung (in German) iv

Danksagungen (in German) v

1 Introduction 1
- 1.1 Motivation . . . 1
- 1.2 Specifications . . . 3
  - 1.2.1 The Cycle . . . 3
  - 1.2.2 The Mechanical System . . . 4
- 1.3 Thermal Modelling . . . 8

2 Induction Machine Modelling 11
- 2.1 Conceptional Design . . . 11
  - 2.1.1 Overview of the Methodology . . . 11
  - 2.1.2 Machine Size Estimation . . . 11
- 2.2 Equivalent Circuit . . . 15
  - 2.2.1 Calculation of the Equivalent Circuit Parameters . . . 15
- 2.3 Field Oriented Control (FOC) . . . 26
  - 2.3.1 Controller Design . . . 26
  - 2.3.2 Flux Optimisation . . . 30

3 Synchronous Reluctance Machine Modelling 32
- 3.1 Basic Principles . . . 32
- 3.2 Analytic Model . . . 34
  - 3.2.1 Direct - axis . . . 35
  - 3.2.2 Quadrature - axis . . . 37
  - 3.2.3 Comparison with FEM . . . 40
  - 3.2.4 Computation of the Mass Moment of Inertia . . . 42
- 3.3 Controller Design . . . 44
  - 3.3.1 Current Controller . . . 44
  - 3.3.2 Speed Controller - MTPA . . . 44
- 3.4 Cross Saturation . . . 48

4 Optimal Designs 52
- 4.1 Optimisation of the IM . . . 53
  - 4.1.1 Optimisation Criterion . . . 55
  - 4.1.2 Final Machine Design . . . 55

4.2 Optimisation of the SynRM . . . 57
4.2.1 Optimisation Criterion . . . 58
4.2.2 Final Machine Design . . . 58

5 Measurement Results 61
5.1 Friction in a Thread . . . 61
5.2 Measurement Results IM . . . 64
5.2.1 Deviation from Original Design . . . 64
5.2.2 Influence of Badly Estimated Parameters . . . 66
5.2.3 Parameter Identification . . . 72
5.2.4 Comparison: Measurement & Simulation . . . 72
5.2.5 Zero Torque Control . . . 78
5.3 Measurement Results SynRM . . . 79
5.3.1 Deviation from Original Design . . . 79
5.3.2 Parameter Identification . . . 80
5.3.3 Comparison: Measurement & Simulation . . . 82

6 Comparison of IM and SynRM 85
6.1 Simulation . . . 85
6.1.1 Load profile: Specification . . . 86
6.1.2 Load profile: Test bench . . . 89
6.2 Results from the Test Bench . . . 91
6.3 Simulation using Results from the Test Bench . . . 96

7 Conclusion 97

A Induction Machine Theory - Derivations 99
A.1 Fundamental Torque Relationship . . . 99
A.2 Linear Magnet Circuit . . . 101
A.3 Derivation of the Equivalent Circuit . . . 102
A.3.1 Transformation of the Rotor Variables to the Stator . . . 103
A.3.2 Transforming the Rotor Differential Equation to the Stator Fixed Coordinate System . . . 104
A.4 Transformation to the Rotor Flux Oriented Coordinate System . . . 106

B Synchronous Reluctance Machine - FEA Results 110

C Influence of Magnetisation Characteristic 112

D Pseudo Cycle 114

Bibliography 116

Glossary 122

Abstract

This work presents the design process of permanent magnet-free brushless AC (induction and synchronous reluctance) machines for a specific actuator application. The specifications include a high dynamic cycle, which should be repeatedly driven by the actuator within given tolerances in an elevated-temperature environment. Both demands given by the application with respect to maximum volume, torque-over-speed performance and the thermal limits of the insulation materials, which limit the maximal loss that may occur, have to be considered.

For the machine's conceptional design, a gross electro-magnetic approach coupled to a thermal model of the actuator is used to estimate the machine's main dimensions. In a subsequently refined design step, starting from the geometry, semi-analytic modelling approaches and suitable controller designs are implemented in an optimisation algorithm (genetic algorithm) to develop designs, appropriate for this application, within the predetermined limits. For this sample case application, the focus of the optimisation is on minimum losses to prevent the winding of the machine from thermal damage; but the structure of the electro-magnetic model and the genetic algorithm allow the presented design method to be also expanded to other applications and optimisation criteria.

The modelling approaches for the two machine types are validated with computations using the finite element method and measurement results of a benchmark study. Due to limitations of production accuracy, some differences between the manufactured motors and the computed optimal machine designs occur. Their influence on the performance of the machine is discussed.

The magnetisation characteristic of the electrical steel sheets is particularly influenced by the degradation caused by laser cutting. This will notably affect small machines with small teeth and can have a great impact on the inductances of the machines.

Both simulation and measurement results show that the IM and SynRM are able to fulfil the requirements determined by the specifications. A comparison between simulations and measurements for the IM as well as the SynRM is presented, focussing on their dynamic and loss performances. The IM is slightly preferable with respect to its dynamic behaviour and the realised position-control accuracy. However, the measured temperature increase indicates lower losses for the SynRM, which suggests it may be preferred for this application.

Zusammenfassung

Diese Arbeit beschreibt den Designprozess für bürstenlose Drehstrommaschinen ohne permanent Magneten (Asynchron- und Synchrone Relukanz Motoren) für eine bestimmte Aktuator Anwendung. Diese Applikation beinhaltet einen hoch dynamischen Zyklus, welcher wiederholt innerhalb festgelegter Toleranzen durchlaufen werden soll und eine erhöhte Umgebungstemperatur. Beide Anforderungen und die thermischen Grenzen der Isolation der Wicklung müssen berücksichtigt werden.

Um die grundlegenden Dimensionen der beiden Maschinen abzuschätzen wird ein grobes elektromagnetisches Model, welches an ein thermische Modell des Aktuators gekoppelt ist, verwendet. Im folgenden verfeinerten Designschritt werden semi-analytische Modelle der Maschinen und geeignete Regler in einem Optimierungsalgorithmus implementiert, um ein Motordesign innerhalb der zuvor festgelegten Grenzen zu berechnen, welches für diese Anwendung geeignet ist. Für diese exemplarische Anwendung zielt die Optimierung auf minimale Verluste, um die Wicklung der Maschinen vor thermischer Beschädigung zu bewahren. Die Struktur der Maschinenmodelle und des genetischen Algorithmus erlauben die verwendete Designmethode auch für andere Anwendungen und Optimierungskriterien zu nützen.

Die Modellierungsansätze der beiden Maschinen wurden mit Finite Elemente Rechnungen und Messergebnissen einer Benchmarkstudie validiert. Aufgrund gewisser Fertigungsgrenzen treten Unterschiede zwischen dem optimalen berechneten Design und den realisierten Maschinen auf. Dieser Einfluss auf die Leistung der Maschinen wird diskutiert.

Die Magnetisierungskennlinie der Elektrobleche wird durch das Laserschneiden beeinflusst. Das wirkt sich vorallem auf kleine Motoren aus und kann einen großen Einfluss auf die Induktivitäten der Maschinen haben.

Sowohl Simulations- als auch Messergebnisse zeigen, dass beide Maschinen für diese Anwendung geeignet sind. In dieser Arbeit wird ein Vergleich der Maschinen präsentiert mit Fokus auf Dynamik und Verluste. Die Asynchronmaschine hat kleine Vorteile in Hinblick auf dynamisches Verhalten. Jedoch, der gemessene Temperaturanstieg während des Betriebs zeigt geringere Verluste für die Synchrone Reluktanzmaschine. Aus diesem Grund ist sie für diese Anwendung zu bevorzugen.

Danksagungen

Diese Dissertation entstand im Rahmen einer wissenschaftlichen Kooperation des Instituts für elektrische Antriebstechnik und Maschinen an der Technischen Universität Graz, unter der Leitung von Frau Univ.-Prof. Dr.-Ing. Annette Mütze, und Kristl, Seibt & Co. GmbH.

Ein besonderer Dank gebührt Herrn Dr. Wilfried Rossegger, der durch seine großzügige Finanzierung dieses Projekt ermöglichte und Herrn Dietrich Sullmann, durch dessen Initiative ich an diesem Projekt teilnehmen durfte.

Des Weiteren möchte ich mich bei Prof. Mütze für die großartige und für mich bis jetzt einzigartige Zusammenarbeit, Organisation und Unterstützung während der gesamten Dauer dieser Arbeit bedanken. In diesem Zusammenhang dürfen auch meine Ansprechpartner bei KS, Stefan Pircher, Dr. Robert Bauer und Marcus Lang nicht fehlen, welche durch kritische Fragen und anregende Diskussionen einen maßgeblichen Beitrag zu dieser Arbeit geleistet haben.

Ein ganz besonderer Dank geht an dieser Stelle auch an Franz Voit, Anton Heilinger, Alexander Lurger und Michael Pagger, welche dieses Projekt mit viel Geduld und Herzblut von der mechanischen Seite aus in die Tat umsetzten.

Zu guter Letzt geht ein großes Danke an meine vielen Kollegen (in alphabetischer Reihenfolge) Dr. Johann Bacher, Stephan Dunkl, Martin Forstinger, Markus Freistätter, Dr. Thomas Haidinger, Dr. Werner Konrad, Klemens Kranawetter, Christian Paar und Martin Wipfler, die mir während der gesamten Dauer dieses Projekts mit Rat und Tat zur Seite standen.

Chapter 1

Introduction

1.1 Motivation

This work presents the design of induction and synchronous reluctance 'machine-based' actuators for a given application in an elevated-temperature environment and discusses their dynamic and loss performances. The basic concept of designing such an actuator is determined by the given application which demands

- high dynamic and exact positioning,
- maintenance-free operation,
- an elevated-temperature environment and
- low material costs.

Conventional actuators are based on the hydraulic or pneumatic principle and require additional components for their fluid supply, e.g. valves which in some cases are high-maintenance. Actuators based on linear electric machines have been replacing their hydraulic or pneumatic counterparts for many years (e.g. [1, 2, 3]). With respect to rotating actuators and the most recent literature, accounts typically refer to applications with much smaller devices than those of interest in the work reported on here (e.g. [4, 5, 6, 7]).

With the advent of power electronics-based drives and the implementation of field-oriented control as state-of-the-art [8], squirrel cage induction machines (IMs) have become also appropriate for dynamic applications as well. While the market share of synchronous reluctance machines (SynRMs) is still relatively low, this type of machine has received renewed and heightened attention in the last years, as reflected by an increasing amount of literature on specific design-related questions (e.g. [9, 10, 11, 12, 13]). Both IMs and SynRMs are not only brushless machines and thus commonly considered to be low-maintenance, but they are also permanent magnet free, making their application also possible in elevated temperature environments, without the risk of demagnetisation (as already identified two decades ago, e.g. [14]) or the market uncertainty of rare-earth magnets [15, 16]. Both IMs and SynRMs may be appropriate machine types for such an application and, with a suitably designed vector control, they should be able to achieve the desired dynamic behaviour and accuracy [17, 18].

A comparison of an IM and a SynRM for steady-state operation, using the same stator, indicates preferences for the SynRM concerning rated torque [19, 20, 21] and temperature increase [22, 23, 24]. An elevated-temperature environment, as part of the work, provides a demanding operating context for the electric actuators. Such operating environments have become increasingly important, as for example reflected by activities in the fields of semiconductor devices and their assemblies (e.g. [25, 26, 27, 28, 29]). Furthermore, permanent magnet (PM) based

machines, despite an inevitable decrease in volume [30], do not provide a viable option, because of the additional costs, e.g. for external cooling to protect the permanent magnets (PMs) from thermal failure. In this context, a better insight into the design challenges of IMs and SynRMs for this field of application will complement the overall understanding of the comparison of these two types of machines.

When compared with the design criteria of other rotating electric machines, the mass moment of inertia of the rotor is also a key parameter for the machine design for the present actuator application, as for any application that demands a high degree of dynamics. Hence, the possibility of increasing the machine's air gap to reduce the copper loss occurring for a certain developed torque may at the same time increase the torque required to accelerate the rotor and thereby the loss.

For the rather small machines of interest in this work, the uncertainties inherent in manufacturing process are relatively high and may have a comparatively large influence on the machine's behaviour. The low-cost requirement of the application, on the other hand, does not allow for increased demands on the manufacturing accuracy. Therefore, the analysis of the influence of these uncertainties on the machine performances is an important factor in the evaluation thereof.

To address these questions, this work discusses two optimum machine designs, including the corresponding design processes tailored to the specific application, i.e. minimum loss designs offering a certain required dynamic performance, one for an IM and one for a SynRM. The finite element method has become the standard for the computation of electrical machines; though, depending on the problem, it could require long computing times. This is why simple and fast semi-analytical models for the computation of those two machine types must be developed, which can be used within an optimisation algorithm.

The final machine designs and the manufactured motors are compared with each other with regard to loss performance, temperature increase during operation and position control deviation. Furthermore, differences between the used controller designs and their influence on the machines' behaviour are discussed.

1.2 Specifications

The electrical machine should be integrated into a given mechanical system, located in an elevated-temperature environment, which may not be changed. Therefore, some parameters such as the shaft diameter of the machine, are determined by the application. In addition, the focus of the machine design is on minimum losses for the given application to prevent the insulation of the winding from thermal damaging.

Chapter 1.2.1 presents the example case cycle used to investigate the designs and to illustrate the methodology and performance and discusses its effect on the design process of the machine. In Section 1.2.2 the mechanical system of the actuator is introduced (see also Fig. 1.1) and Section 1.3 presents a simple thermal model to estimate the steady-state temperature of the actuator during operation.

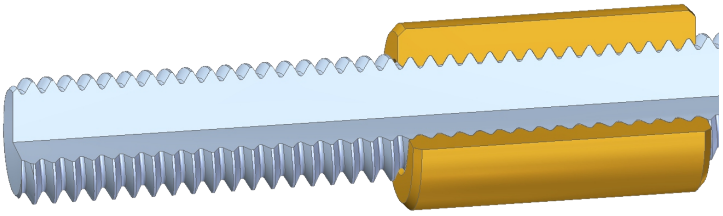

Figure 1.1: Sketch of the spindle, used to transform the circular motion of the motor into a linear motion of the actuator.

1.2.1 The Cycle

The cycle, shown in Fig. 1.2, includes short periods demanding a high degree of dynamic and relatively long still standing times, approximately 30 %. This cycle, specified by a customer, should be repeatedly driven by the actuator and forms the starting point of the design process.

The maximum linear adjusting range of this actuator is 14 mm. It is converted using an appropriate mechanic into an azimuthal angle. Consequently, a rotating electrical machine is used, not a linear drive. Of course, for the electrical machine a position controller has to be implemented to run through the cycle. In addition, the load of the cycle is position dependent. The given tolerances of the cycle are shown in Table 1.1, which means, the actuator has to be able to change its position within 0.1 s with an accuracy of 0.1 mm.

Table 1.1: Tolerances of the cycle of the linear distance x and the time t.

Variable	Value	Unit
Δx	± 0.1	mm
Δt	± 0.1	s

When compared with other applications, the cycle application brings forth the following additional challenges:

1. During the holding times of the cycle, no mechanical power is delivered to the system, but the motor still has to generate position depending holding torque, which causes losses. In these operating points the efficiency is zero.

2. The dynamic periods require a much higher torque than the average torque of the cycle. In these operating points the motor can be overloaded by a certain degree, which has to be considered in the design of the machine.

3. Each time the actuator has to change the position, the motor has to accelerate and brake its own torque of inertia. The rotor diameter d_{RO} of a rotating electrical machine impacts its torque of inertia with the fourth power, hence d_{RO} is also a key parameter for the design process.

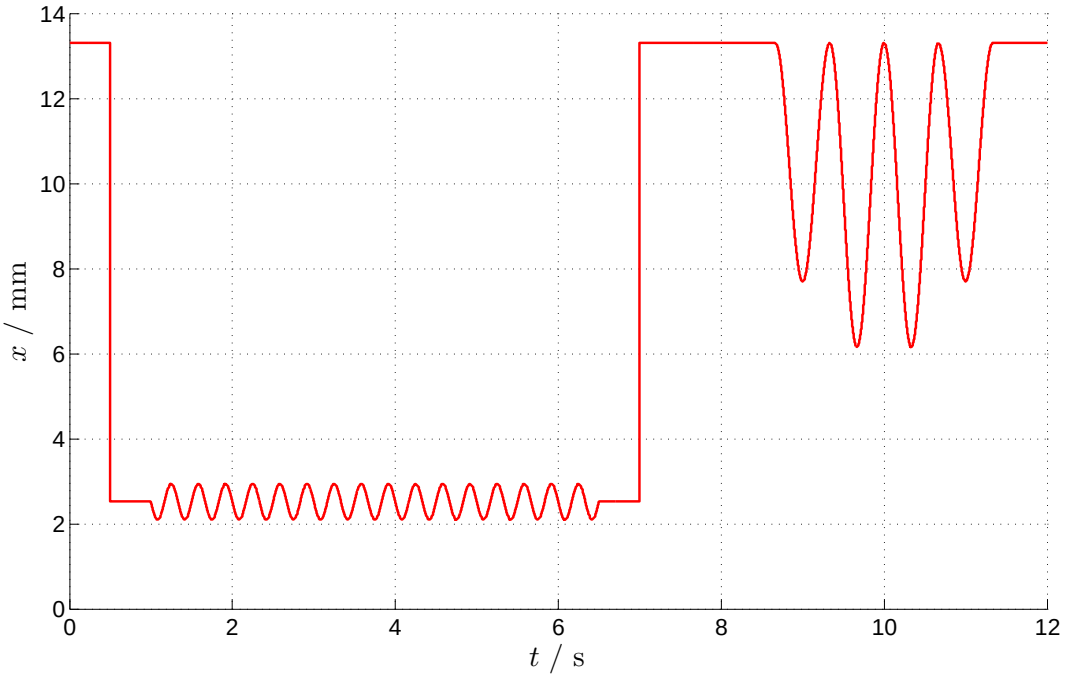

Figure 1.2: Cycle trajectory x, defined by a customer, as a function of time t that should be repeatedly driven by the actuator. It contains, relatively long resting times, dynamic phases (step function response of position) and phases of oscillation movement.

1.2.2 The Mechanical System

The actuator has to work against the force of a spring, proportional to the linear displacement,

$$F_{\mathrm{load}} = D_{\mathrm{spring}}\, x \quad .$$

This spring is prestressed, so that at the cycle position $x = 0\,\mathrm{mm}$ the counterforce is already approximately $50\,\mathrm{N}$.
The spindle forms the heart of the mechanical system and transforms the circular motion of the motor into a linear motion. The spindle pitch k_{spindle} determines the ratio between the linear and the rotary motion,

$$x = \frac{k_{\mathrm{spindle}}}{2\,\pi}\,\varphi \quad ,$$

and defines the maximal values of torque and speed for the motor to fulfil the cycle. Another important parameter for this system is the friction torque

$$T_{\text{fric}} = \frac{1}{2} F\, d_{\text{shaft}}\, \eta_{\text{fric}} + T_{\text{bearing}} \quad .$$

Unfortunately, the determination of the friction coefficient η_{fric} is very difficult. Therefore, for the simulations only an estimation of T_{fric} is used, considering a mean value for the force and a friction coefficient η_{fric} of approximately 5 %. The friction coefficient is influenced by the materials used and determined by an educated guess.

Table 1.2 summarises the parameters given by the mechanical system. A comparison of T_{fric} and T_{max} shows that this system is disproportionately highly influenced by the system friction.

Table 1.2: Summary of the parameters given by the mechanical system.

Description	Symbol	Value	Unit
Counterforce at $x = 14\,\text{mm}$	F_{max}	250	N
Counterforce at $x = 0\,\text{mm}$	F_{min}	50	N
Spindle pitch	k_{spindle}	1.6	mm
Load torque at $x = 14\,\text{mm}$	T_{max}	0.064	Nm
Load torque at $x = 0\,\text{mm}$	T_{min}	0.013	Nm
Friction torque of the system	T_{fric}	0.036	Nm
Diameter of the shaft	d_{shaft}	11	mm
Mass moment of inertia of the shaft	I_{shaft}	$3.5 \cdot 10^{-6}$	kgm^2
DC link voltage	U_{DC}	24	V

The cycle is, from a mathematical point of view, except for the two step changes in position, a "well behaved" function[1]. Certainly, the actuator will not be able to perform this abrupt change of the actuating variable immediately, but will react with some kind of delay.
For these step changes in position a preferable response of the system is shown in Fig. 1.3. An educated guess to estimate the trajectory of the actuator at $t = 7\,\text{s}$ leads to

$$x(t) = \left[-\frac{95-18}{2} \cos\left(\frac{2\,\pi\, t}{2\,\Delta t\, 0.80} \right) + 18 \right] \frac{x_{\text{max}}}{100} \quad , \tag{1.1}$$

which allows to compute the driving speed of the motor. Eq. (1.1) describes the position step of the cycle[2] and also considers a safety of 20 % of the time tolerance, as depicted in Table 1.1. The first derivative of x with respect to time results in the rotational speed of the motor

$$n(t) = \frac{30}{\pi} \frac{d}{dt} \left(\frac{2\,\pi}{k_{\text{spindle}}} x(t) \right)$$

to run through the cycle, depicted in Fig. 1.4. The maximal speed is given by

$$n_{\text{max}} = \frac{95-18}{2} \frac{x_{\text{max}}}{100} \frac{2\,\pi}{k_{\text{spindle}}} \frac{\pi}{\Delta t\, 0.80} \frac{30}{\pi} \quad . \tag{1.2}$$

Except for the two short periods demanding a high degree of dynamic, the rotational speed during the cycle is quite moderate. Therefore, the fundamental frequency of the motor supply

[1] Two times continuously differentiable.
[2] The numbers 95 and 18 in eq. (1.1) denote percent of the maximum linear adjusting range of the actuator.

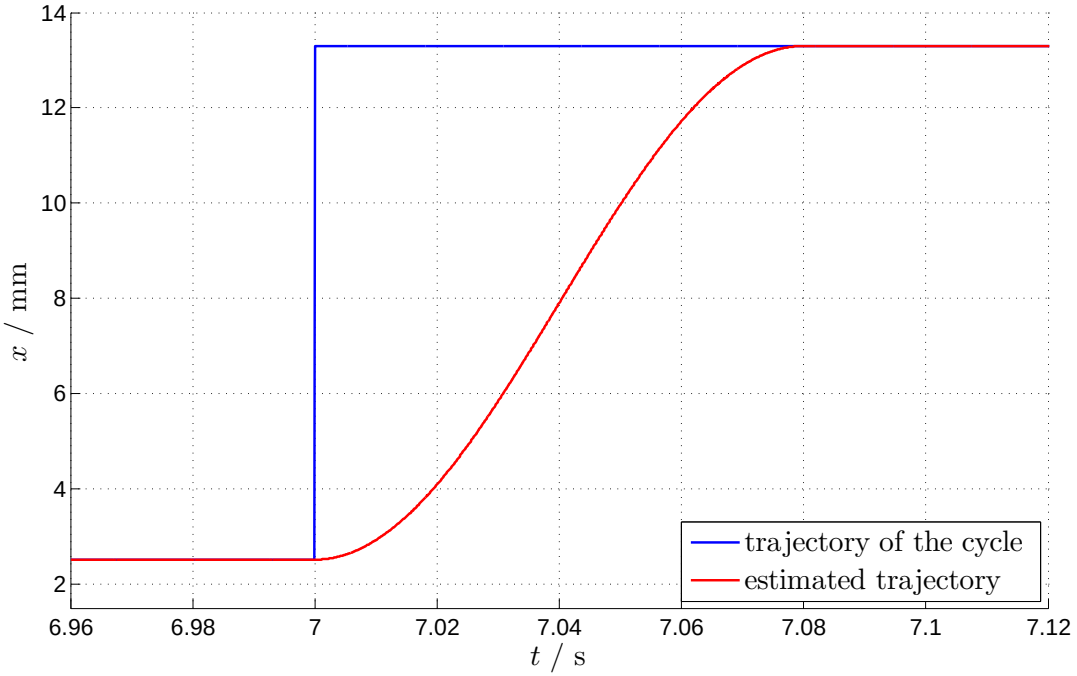

Figure 1.3: Comparison of the cycle trajectory (blue line) and the educated guess (red line), as depicted in eq. (1.1).

voltage will be low as well. Since iron losses depend on the frequency of the supply voltage, they can be neglected in the simulations in good approximation.

The torque, which has to be generated by the motor during the cycle, is calculated in exactly the same manner as outlined above and results in

$$T_{\text{motor}} = I \frac{d^2}{dt^2} \left(\frac{2\,\pi}{k_{\text{spindle}}} x\,(t) \right) + T_{\text{load}}\,(x) + T_{\text{fric}} \quad . \tag{1.3}$$

An evaluation of eq. (1.3), using a mass moment of inertia for the complete system of

$$I = 1.35 \cdot 10^{-5}\,\text{kgm}^2 \quad ,$$

corresponding to a hollow cylinder with an inner diameter of d_{shaft}, an outer diameter of 22 mm and a length of 60 mm, gives the maximum motor torque

$$T_{\text{motor max}} \approx 0.50\,\text{Nm} \quad , \tag{1.4}$$

and the effective torque

$$T_{\text{RMS}} \approx 0.06\,\text{Nm} \quad . \tag{1.5}$$

T_{RMS} is used as a basis for the design process of the IM (Section 2.1.2). A graph of eq. (1.3) is shown in Fig. 1.5.

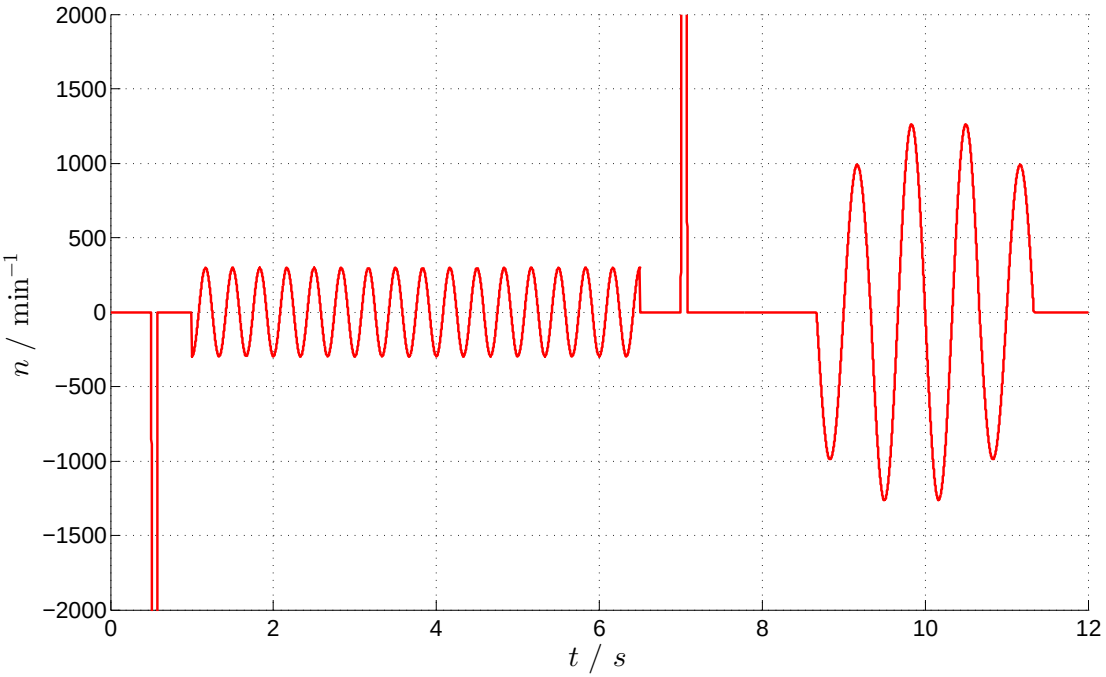

Figure 1.4: Rotational speed of the motor n as a function of time t required to run through the cycle, as described by eq. (1.1), parameters from Table 1.2.

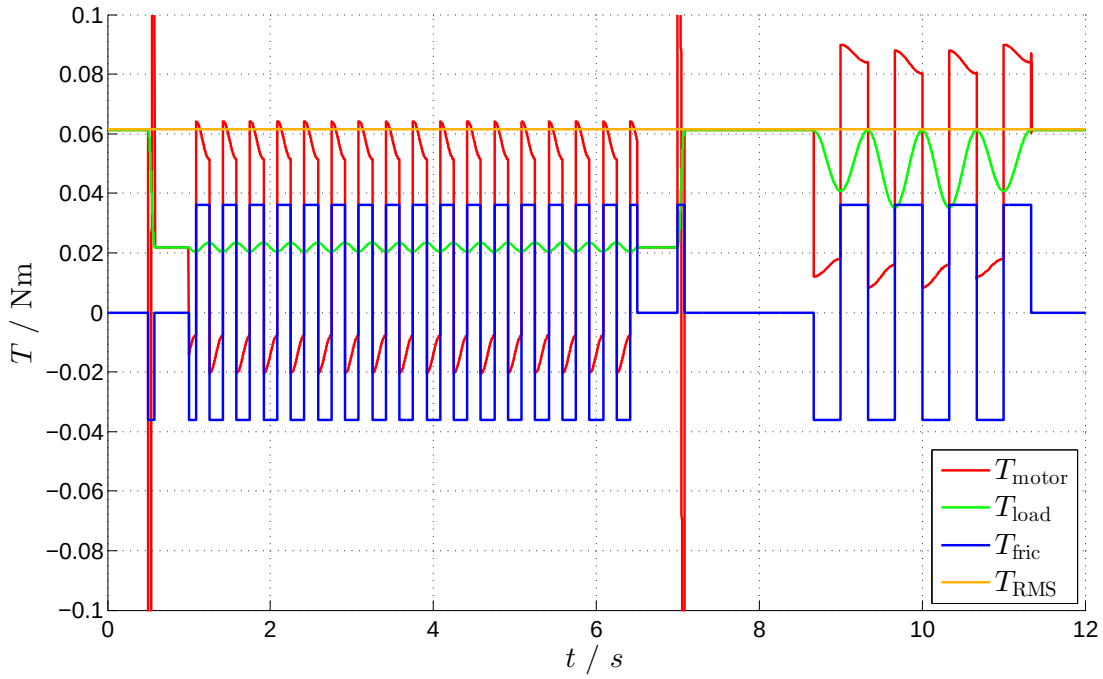

Figure 1.5: The torque T_{motor} (red line), which has to be generated by the motor during the cycle as a function of time t. For comparison also T_{RMS} (orange line, the effective value of T_{motor}), T_{load} (green line) and T_{fric} (blue line) are plotted separately.

1.3 Thermal Modelling

The machines have to be designed to operate at an ambient temperature of about $T_{\mathrm{amb}} = 100\,^{\circ}\mathrm{C}$. A simplified thermal model of the actuator was developed to estimate its steady-state temperature. Within this model, the electric machine of the actuator is described as a cylinder with the outer dimensions of the machine (c.f. Section 2.1) constantly fed with thermal energy.

For about 30 % of the driving cycle, the actuator is at rest, making self-cooling impossible and at the same time, cooling with an external fan would exceed its financial limits. Therefore, the increase of the winding temperature T_{winding} during operation is an important factor for the machine design.

The model considers:

1. Free convection: Only free instead of forced convection is considered [31, Chapter Fa] due to the absence of external cooling for the machine. For the computation of the heat flow $\dot{Q}$ via convection the cylinder barrel and the base area are treated separately.

   - Cylinder barrel: The heat-transfer coefficient λ_{fluid}, the kinematic viscosity ν_{kin} and the Prandtl number Pr are selected from a database [31, Chapter Dbb] and are used for the computation of the heat flow according to eqs. (1.6) to (1.13).

$$\beta_{\mathrm{exp}} = \frac{1}{T_{\mathrm{amb}}} \tag{1.6}$$

$$l_{\mathrm{stream}} = d_{\mathrm{SO}}\,\frac{\pi}{2} \tag{1.7}$$

$$\mathrm{Gr} = \frac{g\,l_{\mathrm{stream}}^3}{\nu_{\mathrm{kin}}^2}\,\beta_{\mathrm{exp}}\,\left(T_{\mathrm{winding}} - T_{\mathrm{amb}}\right) \tag{1.8}$$

$$\mathrm{Ra} = \mathrm{Gr}\,\mathrm{Pr} \tag{1.9}$$

$$f_{\mathrm{Pr}} = \left[1 + \left(\frac{0.559}{\mathrm{Pr}}\right)^{9/16}\right]^{-16/9} \tag{1.10}$$

$$\mathrm{Nu} = \left[0.752 + 0.387\,\left(\mathrm{Ra}\,f_{\mathrm{Pr}}\right)^{1/6}\right]^2 \tag{1.11}$$

$$\alpha_{\mathrm{heat}} = \mathrm{Nu}\,\frac{\lambda_{\mathrm{fluid}}}{l_{\mathrm{stream}}} \tag{1.12}$$

$$\dot{Q} = \pi\,d_{\mathrm{SO}}\,l_{\mathrm{Fe}}\,\alpha_{\mathrm{heat}}\,\left(T_{\mathrm{winding}} - T_{\mathrm{amb}}\right) \tag{1.13}$$

   - Base area: The heat flow of the cylinder base area is calculated similarly, where the values of some parameters differ, see eqs. (1.14) to (1.17).

$$l_{\mathrm{stream}} = d_{\mathrm{SO}} \tag{1.14}$$

$$f_{\mathrm{Pr}} = \left[1 + \left(\frac{0.492}{\mathrm{Pr}}\right)^{9/16}\right]^{-16/9} \tag{1.15}$$

$$\mathrm{Nu} = \left[0.825 + 0.387\,\left(\mathrm{Ra}\,f_{\mathrm{Pr}}\right)^{1/6}\right]^2 \tag{1.16}$$

$$\dot{Q} = \frac{d_{\mathrm{SO}}^2\,\pi}{4}\,l_{\mathrm{Fe}}\,\alpha_{\mathrm{heat}}\,\left(T_{\mathrm{winding}} - T_{\mathrm{amb}}\right) \tag{1.17}$$

2. Radiation: In the given application, the actuator is located in a chamber that is large compared to its size. Radiation towards infinity can thus be assumed with good approximation [32, Chapter 7]. Due to the surface characteristics of the machine, the emissivity coefficient is estimated to 0.8, which gives a heat flow of

$$\dot{Q} = \sigma_{\mathrm{B}}\, \epsilon\, A_{\mathrm{cyclinder}} \left(T^4_{\mathrm{winding}} - T^4_{\mathrm{amb}}\right) \quad , \tag{1.18}$$

with

$$\sigma_{\mathrm{B}} \approx 5.67 \cdot 10^{-8} \frac{\mathrm{W}}{\mathrm{m^2\,K^4}} \quad . \tag{1.19}$$

3. Thermal conduction: This heat flow occurs mainly along the machine mounting, such as the shaft and the mounting pads/screws. For simplification, all such paths are treated as one and described by one thermal resistance R_{therm}, equivalent to an iron rod of 12 mm diameter and 100 mm length, as derived from the application. The heat flow via thermal conduction is given by

$$\dot{Q} = \frac{T_{\mathrm{winding}} - T_{\mathrm{amb}}}{R_{\mathrm{therm}}} \quad . \tag{1.20}$$

An estimation of the steady-state temperature, using the conceptional thermal modelling approach presented in this Section, indicates that the maximal mean copper loss $\overline{P}_{\mathrm{Cu}}$ to run through the cycle at $T_{\mathrm{amb}} = 100\,^{\circ}\mathrm{C}$ must not exceed 24 W. Under these circumstances the motor would reach an over-temperature ($T_{\mathrm{winding}} - T_{\mathrm{amb}}$) of about 80 K, as illustrated in Fig. 1.6a, which is at the thermal limit of the winding's insulation.

We note that the results indicate a strong sensitivity of the steady-state temperature towards the thermal coupling between the machine and the ambient, notably the thermal resistance of the heat conduction R_{therm}. Fig. 1.6b illustrates this sensitivity for different values[3] of R_{therm} and assumed total losses (here: copper losses, see Section 1.2.2) of 24 W. Thus, a modification of the mounting arrangement might allow for an additional reduction of the volumes of the machines that meet the thermal and dynamic requirements. Since both types of machines investigated showed to fulfil the original design specifications, this path has not been investigated further.

[3] $k = 1$ fits to the original computation of Fig. 1.6a.

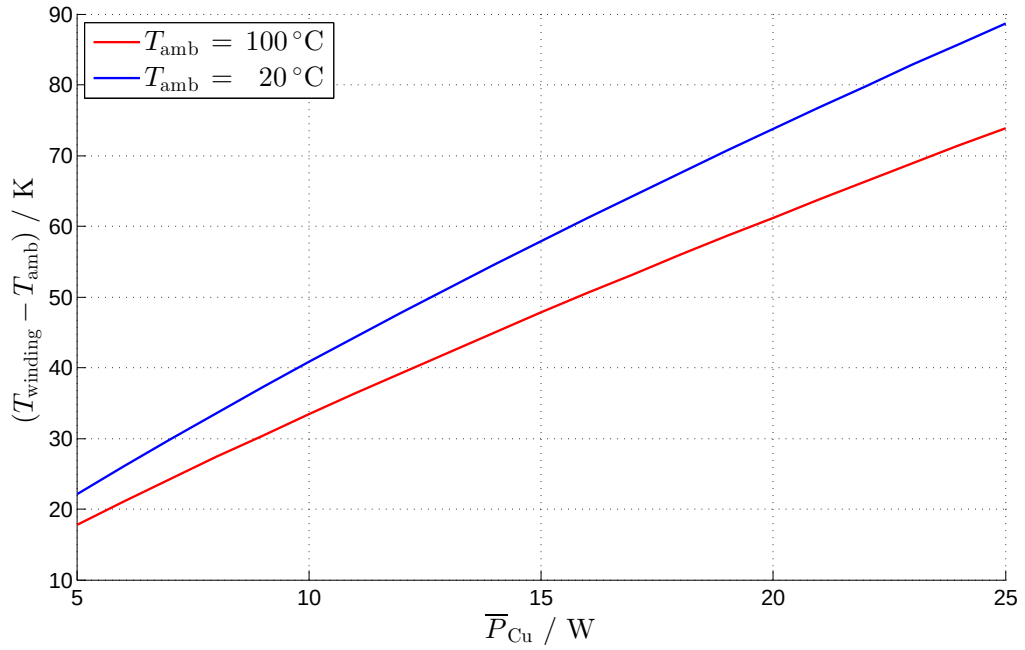

(a) Steady-state temperature of the motor as a function of the mean copper losses $\overline{P}_{\mathrm{Cu}}$ using the modelling approach presented in this Section. T_{amb} indicates the ambient temperature.

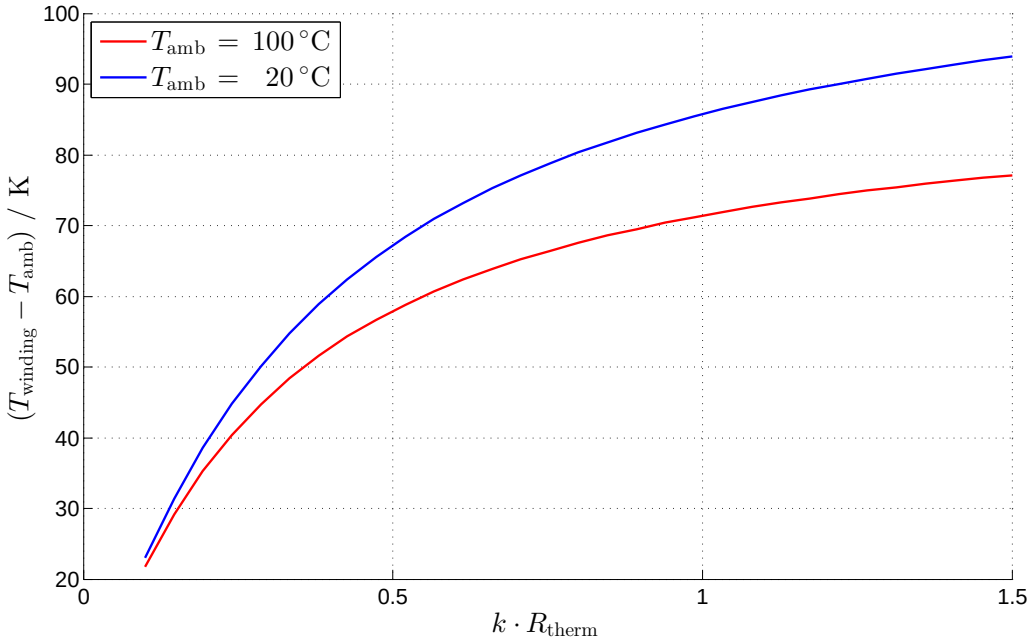

(b) Steady-state temperature of the motor as a function of the thermal resistance of the heat conduction R_{therm} assuming copper losses of 24 W. $k = 1$ fits to the original computation of Fig. 1.6a.

Figure 1.6: Results of the thermal model.

Chapter 2

Induction Machine Modelling

Section 2.1 presents a method to determine the outer dimensions of the machine, which are fixed in the further design process and act as constraints for the minimal loss design, presented in Section 4.1. Sections 2.2 and 2.3 discusse basic principles for simulating and controlling the induction machine. Various deviations for the IM modelling are reviewed in Appendix A.

2.1 Conceptional Design

2.1.1 Overview of the Methodology

A method to estimate the basic dimensions, the outer diameter d_{SO} and the active length l_{Fe} of an induction motor, is presented. This method requires prior knowledge of the inner dimensions of the motor (such as the ratio between outer diameter and bore diameter) and uses the maximal permitted losses, which are typically determined by the cooling to compute the allowed current sheet. To estimate the current linkage and the magnetic field density in the air gap, a linear magnetic characteristic is assumed. Using these electric and magnetic variables, as well as an educated guess for the rotor current angle, the torque is calculated.

The mechanical demands on the machine result from the defined cycle and are considered under two conditions, eqs. (2.1) and (2.2).

A schematic illustration of the method is shown in Fig. 2.1. In the computation all reasonable combinations of P_{Cu}, d_{SO} and l_{Fe} are used to identify a compromise between, on the one hand, a machine with a small volume and, on the other hand, low losses.

The results of the method, the outer diameter d_{SO} and the active length l_{Fe}, are used as astarting point of a refined design in which details, such as the number of slots or the winding are determined, as discussed in Section 4.1.

2.1.2 Machine Size Estimation

The relations derived in Appendices A.1 and A.2 are used to estimate the main dimensions of the machine, considering the mechanical constraints, determined by the cycle (Section 1.2.2). But, to this aim, some additional assumptions have to be made.

1. The conductors in the motor (stator and rotor) are made of copper and a temperature of 100 °C is assumed.
2. The permitted losses P_{Cu} are divided in the ratio of 2:1 between stator and rotor.
3. The cross sectional area of the rotor bars is circularly shaped.
4. The diameter of the shaft d_{shaft} is 11 mm, as depicted in Table 1.2.

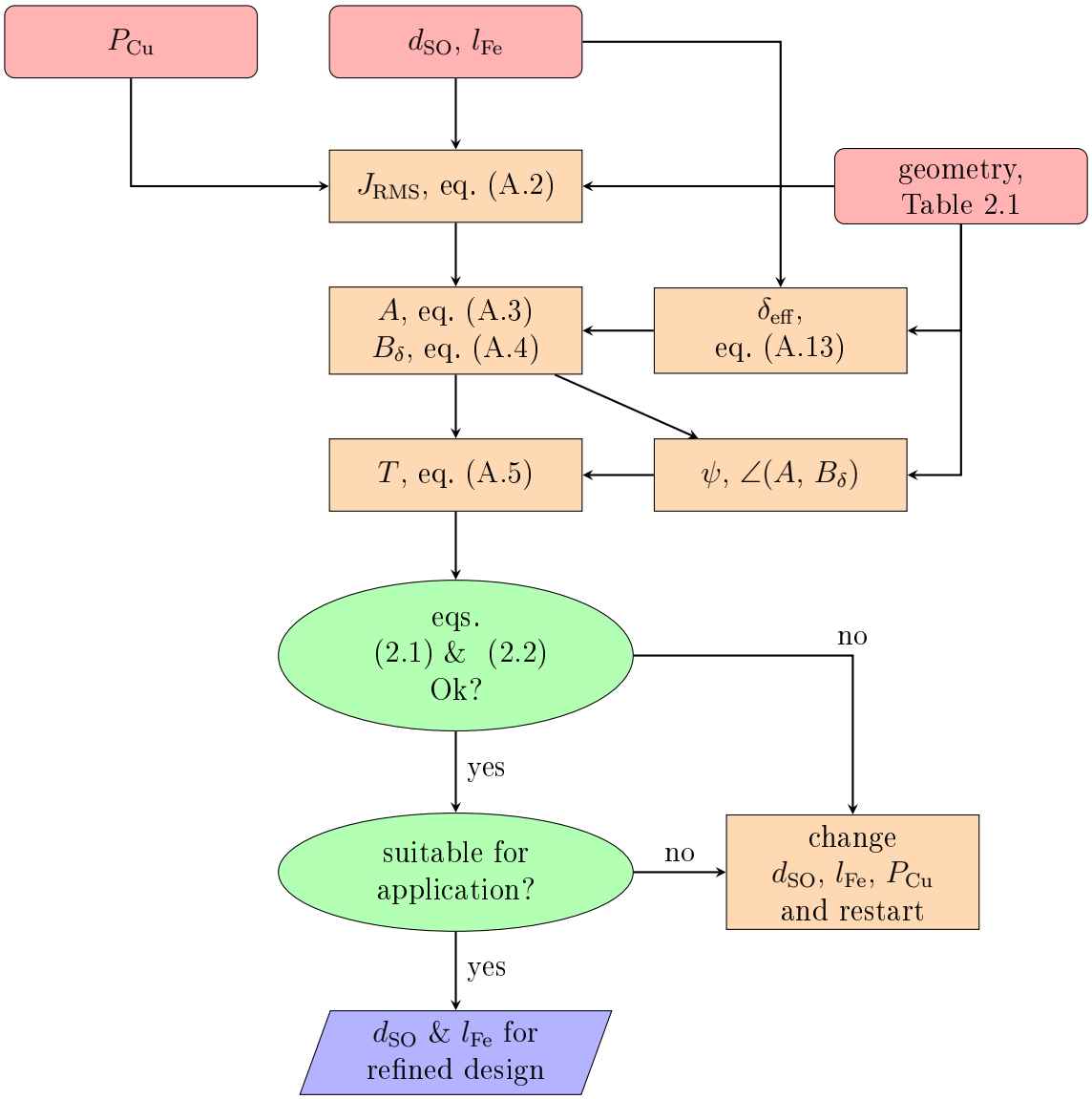

Figure 2.1: Schematic illustration of the computation to choose suitable values for the outer dimensions of the machine.

5. The other required starting points, for the geometry and material of the motor, are listed in Table 2.1.

Table 2.1: Starting points for sizing the machine

Description	Symbol	Value	Unit
Ratio of air-gap diameter and outer diameter	d_δ/d_{SO}	0.525	-
Ratio of height slot-tooth layer and height of stator	$h_{\mathrm{ST}}/(h_{\mathrm{ST}}+h_{\mathrm{SJ}})$	0.440	-
Ratio of height slot-tooth layer and height of rotor	$h_{\mathrm{RT}}/(h_{\mathrm{RT}}+h_{\mathrm{RJ}})$	0.480	-
Ratio of tooth-width and slot pitch stator	$a_{\mathrm{S}}/\tau_{\mathrm{SSP}}$	0.250	-
Ratio of tooth-width and slot pitch rotor	$a_{\mathrm{R}}/\tau_{\mathrm{RSP}}$	0.333	-
Width of the short-circuit ring[1]	a_{SCR}	5.0	mm
Air gap length	δ	0.2	mm
Carter factor	k_{C}	1.2	-
Relative permeability of the iron sheet	μ_{r}	310	-
Slot fill factor	k_{sff}	0.5	-
Phase angle of rotor current	ψ_{R}	-124	°

These values originate from a machine used in a benchmark study and are used to give a rough estimation of the developed torque for two different cases.

1. Loss equivalent torque

   Given the permitted losses, the machine has to produce at least a torque, which causes the same losses as if the machine would drive through the defined cycle.

   In contrast to eq. (A.6), which supposes linear magnetic properties and steady state operation, the relationship between copper losses and torque of a field oriented controlled induction motor is similar to a separately excited DC machine (see Section 2.3.1). Therefore, this loss equivalent torque is given by the effective value of the torque T_{RMS} [33, Chapter 8.3], which has to be generated by the motor during the cycle,

$$\overline{T}_{\mathrm{motor}} \;\geq\; T_{\mathrm{RMS}} \;=\; \sqrt{\frac{1}{\tau}\int_0^{\tau} \left[T_{\mathrm{motor}}\left(t\right)\right]^2 dt} \;\approx\; 0.061\,\mathrm{Nm} \quad . \tag{2.1}$$

2. Angular acceleration

   The machine has to achieve the required angular acceleration,

$$\ddot{\varphi} \;\geq\; \frac{1}{I}\left(T_{\mathrm{motor}} - T_{\mathrm{mech}}\right) \approx 3.25 \cdot 10^4\,\mathrm{rad/s^2} \quad , \tag{2.2}$$

   to fulfil the cycle, if it is overloaded temporarily by

$$\frac{T_{\mathrm{motor\,max}}}{T_{\mathrm{RMS}}} \;=\; \frac{0.50\,\mathrm{Nm}}{0.06\,\mathrm{Nm}} \;\approx\; 8 \quad .$$

[1] The height of the short circuit ring is equal to the rotor height.

Fig. 2.2 shows the results of the calculation. In terms of color, the surface plot shows the required permitted losses in Watt to fulfil the conditions of eqs. (2.1) and (2.2) as a function of the outer diameter d_{SO} and the active length l_{Fe}. According to this Figure, a machine with

$$l_{\mathrm{Fe}} = 60\,\mathrm{mm} \quad \text{and} \quad d_{\mathrm{SO}} = 40\,\mathrm{mm} \tag{2.3}$$

might be a suitable compromise between volume, permitted losses and portion of end windings.

In the subsequent design process of the motor, the outer dimensions (eq. (2.3)) are fixed and the machine is optimised within these limits.

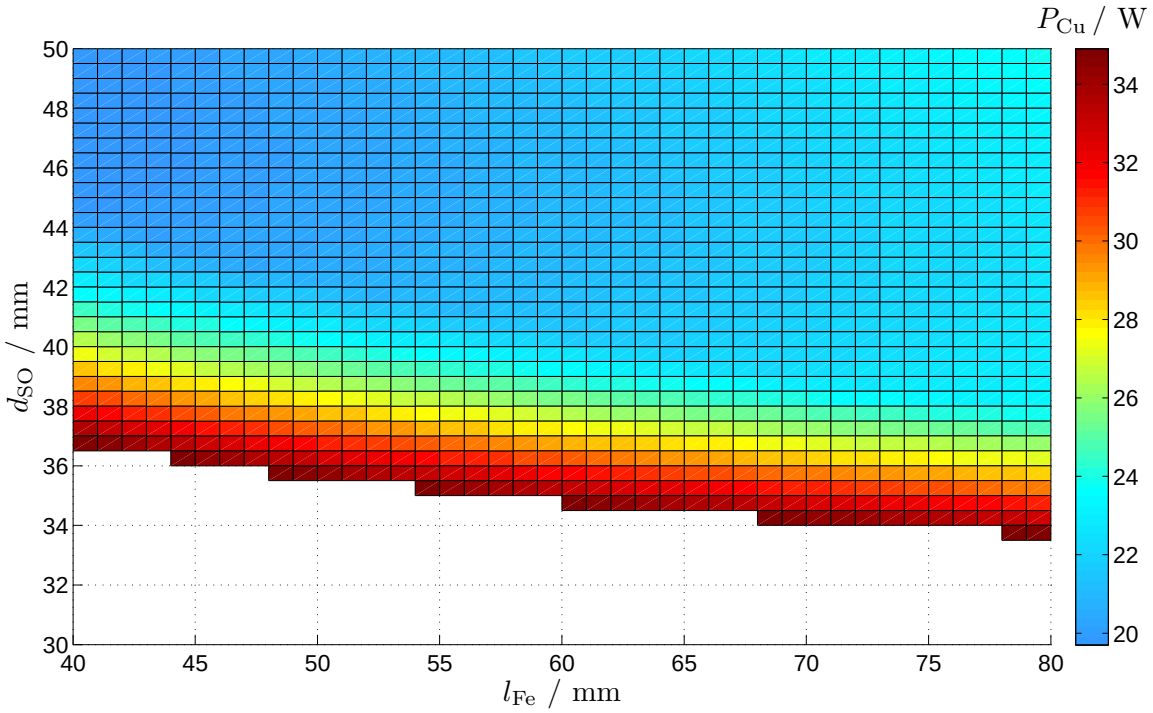

Figure 2.2: In terms of color, the required permitted losses P_{Cu} in Watt to fulfil the conditions in eqs. (2.1) and (2.2) as a function of outer diameter d_{SO} and active length l_{Fe}. The computation is performed for $p = 1$.

2.2 Equivalent Circuit

A fundamental wave model of the IM is reviewed in Appendix A.3, which is used for simulation purposes. Section 2.2.1 discusses the computation of the equivalent circuit parameters.

2.2.1 Calculation of the Equivalent Circuit Parameters

An essential task for simulating electrical machines is the computation of the underlying model parameters. The more exact these parameters are calculated, the better are the simulation results. For the presented model of the induction machine five parameters are needed, whereby the calculation of R_S, R_R and $L_{\mathrm{S}\sigma}$ is straight-forward and is reviewed in detail in [34, 35].

A more complicated challenge is the computation of the leakage inductance of the rotor $L_{\mathrm{R}\sigma}$ and the main inductance L_h, considering their non-linearities. This is why, this Section focuses on these parameters.

If additional results of a finite element analysis [36] are available, it is possible to improve the model parameters. In the context of this work, steady state characteristics of the induction machine are computed using the equivalent circuit parameters and are fitted to the results of the finite element method. Further details are given in Section 2.2.1.3.

2.2.1.1 Rotor slot leakage inductance

The leakage inductance of a machine can be calculated as the sum of different leakage inductances [37, Chapter 4], such as slot leakage inductance, end winding leakage inductance and tooth tip leakage inductance.

An essential component for an induction motor is the slot leakage inductance. For a round slot (sketched in Fig. 2.3) Richter [38, eq. 381] gives the slot permeance factor λ,

$$\lambda \;=\; 0.47 + 0.066\,\frac{d_\mathrm{bar}}{a_\mathrm{RSO}} + \frac{h_\mathrm{bar}}{a_\mathrm{RSO}} \quad , \tag{2.4}$$

which is proportional to the inductance. Eq. (2.4) is only applicable for open rotor slots, since

$$\lim_{a_\mathrm{RSO}\to 0} \lambda \;=\; \infty \quad .$$

The inductance of closed rotor slots, which are often used for IMs, depends highly on the properties of the material and the saturation of the flux bridge. Richter also treats this topic in [39, Fig. 114].

Another semi-analytic approach has been developed in the context of this work and is presented at this point. On the one hand, this ansatz is based on a finite element calculation to identify the saturation of the flux bridge. On the other hand a "virtual slot opening width" is defined.

That means, determining a region of the flux bridge, which is saturated to a certain degree (blue area in Fig. 2.3) with the help of the finite element calculation. For that region the average of the relative permeability μ_r using the magnetisation characteristic of the iron sheet is computed. The remaining part of the flux bridge is neglected in this consideration.

Defining this virtual slot opening width leads back to the original eq. (2.4) to calculate the slot permeance factor λ, except that the result has to be multiplied with the mean value of μ_r of the saturated region in the flux bridge.

The proposed method is, strictly speaking, only valid for a specific point of operation of the machine, but a comparison with results of a finite element calculation shows a suitable agreement for steady state characteristics for this application.

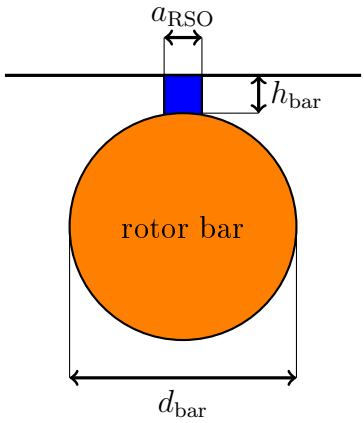

Figure 2.3: Sketch of a round rotor slot. The blue area illustrates the region of the flux bridge which is saturated to a certain level. Its width can be used to calculate the slot permeance factor according to eq. (2.4).

2.2.1.2 Main Inductance

In consideration of saturation, the calculation of the main inductance is based on an accurate calculation of the magnet circuit of the machine for various magnetising currents $\hat{I}_\mu$, c.f. Fig. A.2.

The magnet circuit is divided into different regions (air gap, yoke and slot-teeth layer for stator and rotor) to calculate the required current linkage for a given saturation state but, in contrast to the deviation in Appendix A.2, the non-linear magnetisation characteristic of the iron sheet is considered.

The entire computation of the main inductance can be divided into three interlaced calculations, which are based on [40, Chapter 2]. Within these calculations iterative loops are needed to obtain self-consistent results.

1. Current linkage of the slot-tooth layer

   The aim of this calculation is to obtain the magnetic voltage drop of the slot-tooth layer

   $$\hat{U}_{\delta\,\mathrm{slot\,tooth}} = \hat{U}_\delta + \hat{U}_{\mathrm{ST}} + \hat{U}_{\mathrm{RT}} \quad , \tag{2.5}$$

   for different values of $\hat{B}_\delta$ and to consider that a certain part of the magnetic flux, entering the slot pitch, will also flow across the slot. The computation of the magnetic voltage over the air gap $\hat{U}_\delta$ is straight forward, according to eq. (A.8).

   The challenge is the computation of $\hat{U}_{\mathrm{ST}}$ and $\hat{U}_{\mathrm{RT}}$. The problem is equivalent to a parallel connection of a constant magnetic resistance (slot) and a variable one (tooth), which can only be solved iteratively and has to be performed for every desired value of $\hat{B}_\delta$, separately for stator and rotor.

   The different steps of the computation are listed below and illustrated in Fig. 2.4 for the slot-tooth region of the stator. However, the approach is the same for the rotor.

   - At the beginning of the iteration an initial guess for the flux density in the tooth is needed. Certainly, the better the start value is estimated, the faster the iteration converges. A suitable initial guess might be

     $$\hat{B}_{\mathrm{S\,tooth}} = \hat{B}_\delta \frac{\tau_{\mathrm{SSP}}}{a_{\mathrm{S}}} \quad . \tag{2.6}$$

- In the next step the magnetic field strength of the tooth $H_{\mathrm{S\,tooth}}$ is computed using the magnetisation characteristic of the iron sheet and subsequently the magnetic flux density in the slot via

$$\hat{B}_{\mathrm{S\,slot}} = \mu_0 \, H_{\mathrm{S\,tooth}} \quad . \tag{2.7}$$

- The flux densities of tooth and slot give the magnetic flux entering the slot pitch,

$$\Phi_{\mathrm{SSP}} = \Phi_{\mathrm{S\,slot}} + \Phi_{\mathrm{S\,tooth}} = \left[\hat{B}_{\mathrm{S\,tooth}} \, a_{\mathrm{S}} + \hat{B}_{\mathrm{S\,slot}} \, (\tau_{\mathrm{SSP}} - a_{\mathrm{S}})\right] l_{\mathrm{Fe}} \quad . \tag{2.8}$$

- Φ_{SSP} is used to compute a new estimation of the air gap flux density,

$$\hat{B}^*_{\delta} = \frac{\Phi_{\mathrm{SSP}}}{\tau_{\mathrm{SSP}} \, l_{\mathrm{Fe}}} \quad . \tag{2.9}$$

These steps are repeated until the resulting flux density of the air gap $\hat{B}^*_{\delta}$ equals the target value $\hat{B}_{\delta}$.

At the end of the iteration, the last value of $H_{\mathrm{S\,tooth}}$ is used to calculate the magnetic voltage drop of the slot-tooth layer.

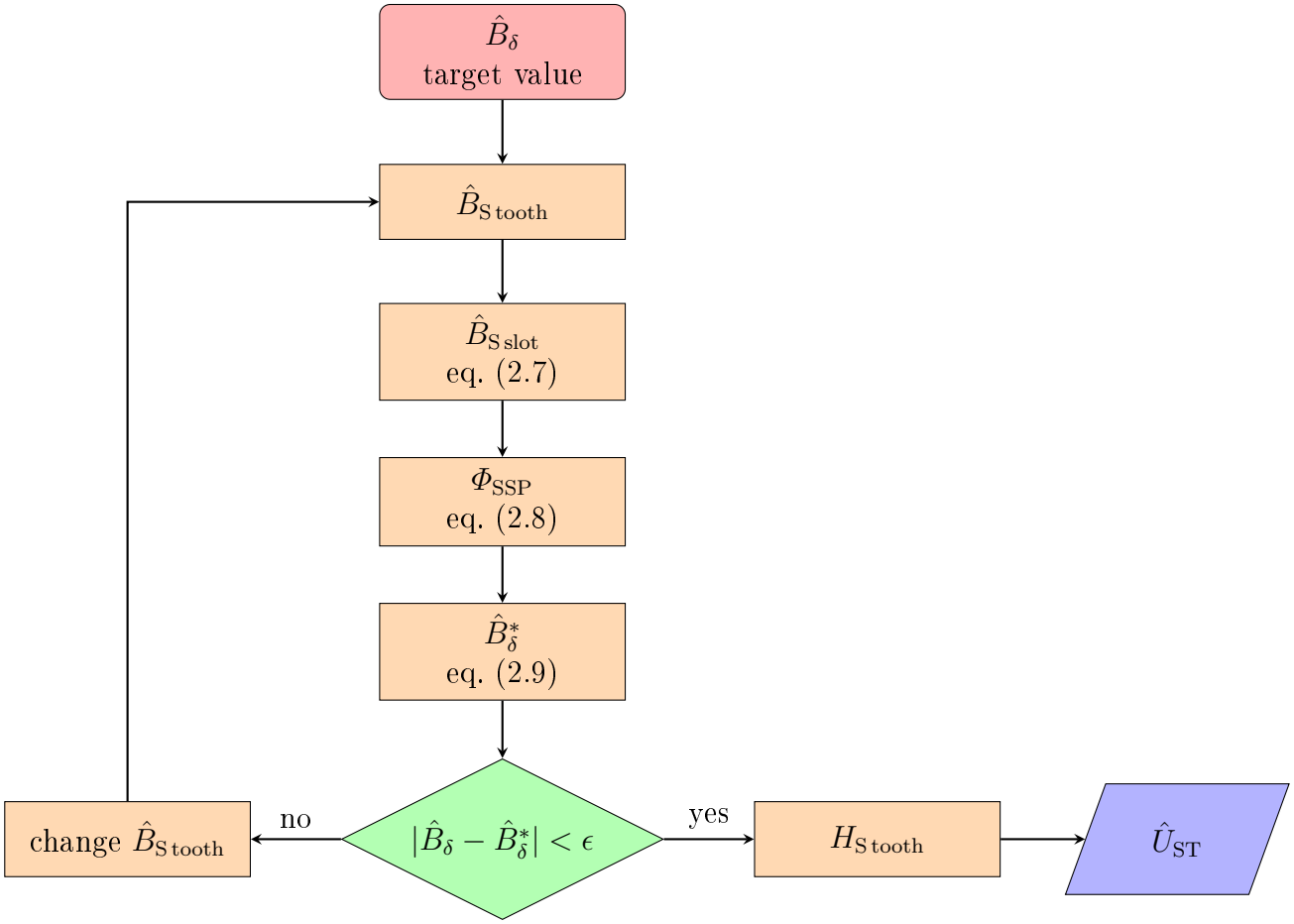

Figure 2.4: Schematic illustration of the iteration to compute the magnetic voltage drop of the slot-tooth region $\hat{U}_{\mathrm{ST}}$ for a given $\hat{B}_{\delta}$.

2. Current linkage of the yokes

   For the calculation of the required current linkage of the yokes $\hat{U}_{\mathrm{SJ}}$ and $\hat{U}_{\mathrm{RJ}}$, the previously obtained result of the slot-tooth layer ($\hat{U}_{\delta\,\mathrm{slot\,tooth}}$ as a function of $\hat{B}_\delta$) is needed. Again, the computation can be divided into different steps, listed below and illustrated in Fig. 2.5 and has to be performed separately for stator and rotor.

   - As input for the computation, a specific value of $\hat{B}^*_\delta$ is needed, which is converted into the maximum value of current linkage of the slot-tooth layer $\hat{U}^*_{\delta\,\mathrm{slot\,tooth}}$ using the previously obtained results.
   - The distribution of the magnetomotive force of the slot-tooth layer $U_{\delta\,\mathrm{slot\,tooth}}$ across a pole pitch is estimated to be trapezoidal, defined as follows.

$$U_{\delta\,\mathrm{slot\,tooth}} = \begin{cases} \frac{3}{\tau_\mathrm{p}}\,\hat{U}^*_{\delta\,\mathrm{slot\,tooth}}\,x & 0 \le x < \frac{\tau_\mathrm{p}}{3} \\ \hat{U}^*_{\delta\,\mathrm{slot\,tooth}} & \frac{\tau_\mathrm{p}}{3} \le x < \frac{2\,\tau_\mathrm{p}}{3} \\ -\frac{3}{\tau_\mathrm{p}}\,\hat{U}^*_{\delta\,\mathrm{slot\,tooth}}\,x + 3\,\hat{U}^*_{\delta\,\mathrm{slot\,tooth}} & \frac{2\,\tau_\mathrm{p}}{3} \le x < \tau_\mathrm{p} \end{cases}$$

     The current linkage distribution is converted, using again the results of the previous computation to obtain the flux density in the slot-tooth layer $B_{\delta\mathrm{ST}}$ across a pole pitch.

   - For simplification, only the peak fundamental value $\hat{B}^1_{\delta\mathrm{ST}}$ of $B_{\delta\mathrm{ST}}$ is used to calculate the maximum flux density in the yoke region

$$\hat{B}^1_\mathrm{J} = \frac{\Phi_\mathrm{J}}{l_\mathrm{Fe}\,h_\mathrm{J}} = \frac{\Phi_\mathrm{p}}{2\,l_\mathrm{Fe}\,h_\mathrm{J}} \overset{\text{eq. (A.10)}}{=} \frac{\tau_\mathrm{p}}{\pi\,h_\mathrm{J}}\,\hat{B}^1_{\delta\mathrm{ST}} \quad . \tag{2.10}$$

   - The flux density in the yoke B_J is approximated sinusoidal and converted into the magnetic field strength in the yoke H_J using the magnetisation characteristic of the iron sheet.
   - The magnetic voltage drop of the yoke is the product of the mean value of the magnetic field strength $\overline{H_\mathrm{J}}$ and the average length of the magnetic field lines in the yoke,

$$\hat{U}_\mathrm{J} = \overline{H_\mathrm{J}}\,l_\mathrm{HJ} \quad . \tag{2.11}$$

3. Main inductance

   For the computation of the main inductance, the machine is assumed to be in no-load operation (no current flow in rotor, cf. Fig. A.2) for a given stator voltage U_S and stator voltage angular frequency ω_S. In addition, detailed information on the geometry of the motor is needed to calculate the leakage inductance $L_{\mathrm{S}\sigma}$ and the ohmic resistance R_S of the stator.

   The problem results in an iteration containing different steps, listed below and illustrated in Fig. 2.6, which has to be performed for every desired value of U_S.

   - The iteration starts with an educated guess for the main inductance L_h, which is used to compute the voltage drop

$$U_\mathrm{h} = \mathrm{i}\,\omega_\mathrm{S}\,L_\mathrm{h}\,\frac{U_\mathrm{S}}{R_\mathrm{S} + \mathrm{i}\,\omega_\mathrm{S}\,(L_\mathrm{h} + L_{\mathrm{S}\sigma})} \quad .$$

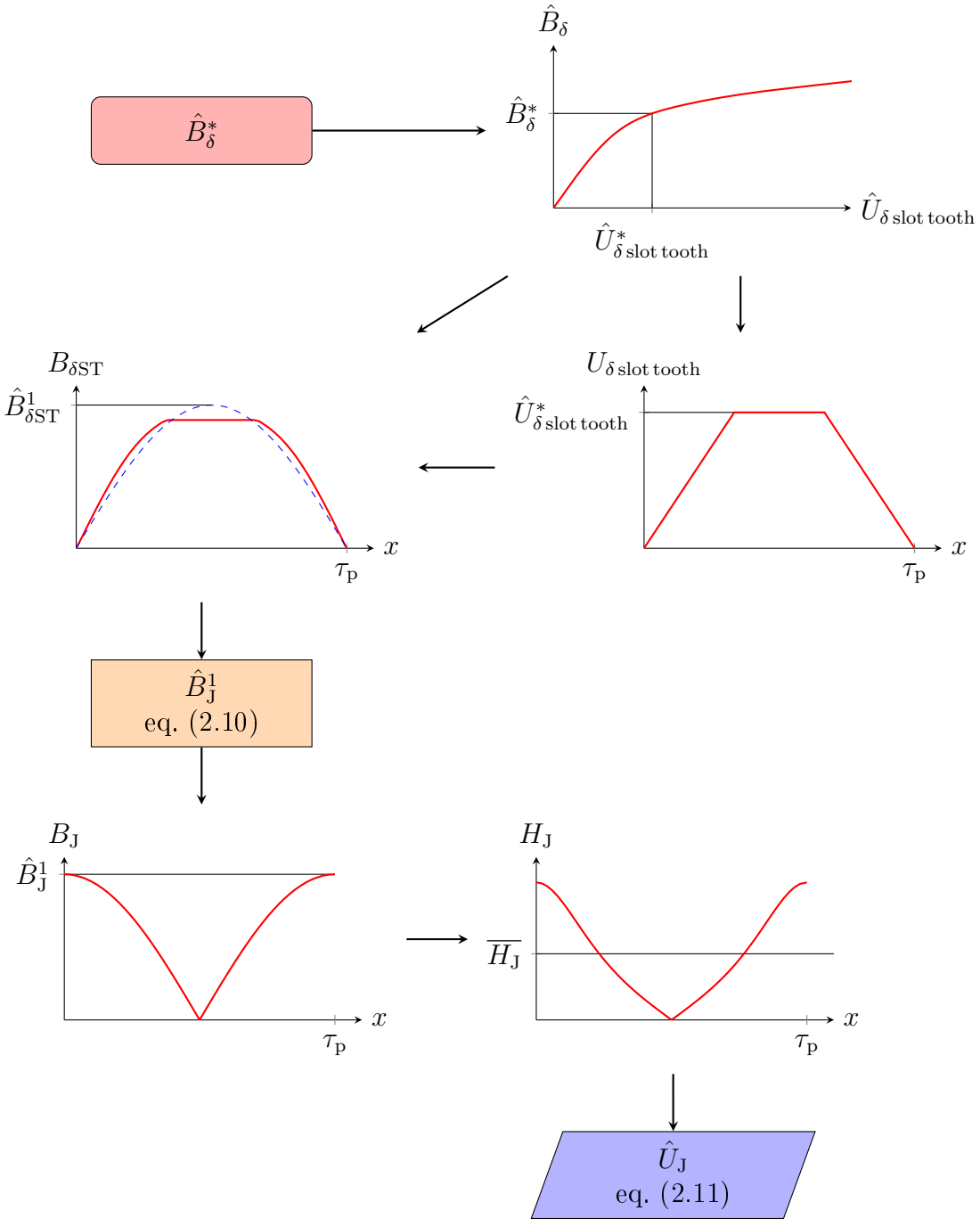

Figure 2.5: Schematic illustration to compute required current linkage of the yokes.

A suitable initial guess might be

$$\left| \frac{\mathrm{i}\,\omega_\mathrm{S}\,L_\mathrm{h}}{R_\mathrm{S} + \mathrm{i}\,\omega_\mathrm{S}\,(L_\mathrm{h} + L_{\mathrm{S}\sigma})} \right| \approx 0.85 \quad ,$$

or, if results of finished iterations are available, that value of L_h with the stator voltage nearest to the present one.

- U_h is used to calculate the magnetic flux

$$\Phi_\mathrm{p} = \frac{\sqrt{2}\,U_\mathrm{h}}{\omega_\mathrm{S}\,\xi\,w_\mathrm{str}} \tag{2.12}$$

and the magnetic flux density in the air gap

$$\hat{B}_\delta = \frac{\pi\,\Phi_\mathrm{p}}{2\,\tau_\mathrm{p}\,l_\mathrm{Fe}} \quad .$$

- $\hat{B}_\delta$ serves as an input for the computation of the magnetic voltage drop of the slot-tooth layer and the yokes. Their sum gives an expression (eq. (A.7)) for the required current linkage for one pole of the machine, which is used to compute the magnetizing current in this operation point,

$$I_\mu = \frac{1}{2}\,\frac{\hat{U}_\mathrm{p}\,\pi\,p}{\sqrt{2}\,m\,\xi w_\mathrm{str}} \quad , \tag{2.13}$$

according to [37, eq. (3.60)].

- Ohm's law gives a new estimation for the main inductance

$$L_\mathrm{h}^* = \frac{U_\mathrm{h}}{\omega_\mathrm{S}\,I_\mu} \quad . \tag{2.14}$$

These steps are repeated until the k^th iteration of L_h equals the $(k-1)^\mathrm{th}$ one, within a specified tolerance limit. To increase the stability of the iteration it is beneficial to introduce a relaxation parameter f [41, Chapter 10].

$$L_\mathrm{h}^*(k) = (1-f)\,\frac{U_\mathrm{h}}{\omega_\mathrm{S}\,I_\mu} + f\,L_\mathrm{h}^*(k-1) \quad , \quad f \in (0,\,1) \quad .$$

2.2.1.3 Improving the equivalent circuit parameters

In this work standard minimisation algorithms [42, Chapter 10] are used to adjust the parameters of the equivalent circuit, such that steady state characteristics of the induction machine (no-load curve, current-slip curve and torque-slip curve) computed using the model, derived in Section A.3, are in agreement with the results of a finite element simulation. This method is similar to the method of least squares.

The results of the FEA, presented in Figs. 2.7 to 2.9, are obtained using a two-dimensional transient simulation. Within the simulation, the voltage, its frequency and the slip are fixed and the current respectively the torque is computed by averaging over several electric periods, after the transient effect has decayed. The underlying geometry of the presented FEA results is shown in Fig. 4.3.

To keep the dimensions of the minimisation space as small as possible, the stator ohmic resistance R_S is assumed to be correct and is therefore not changed. The computation is divided into two steps.

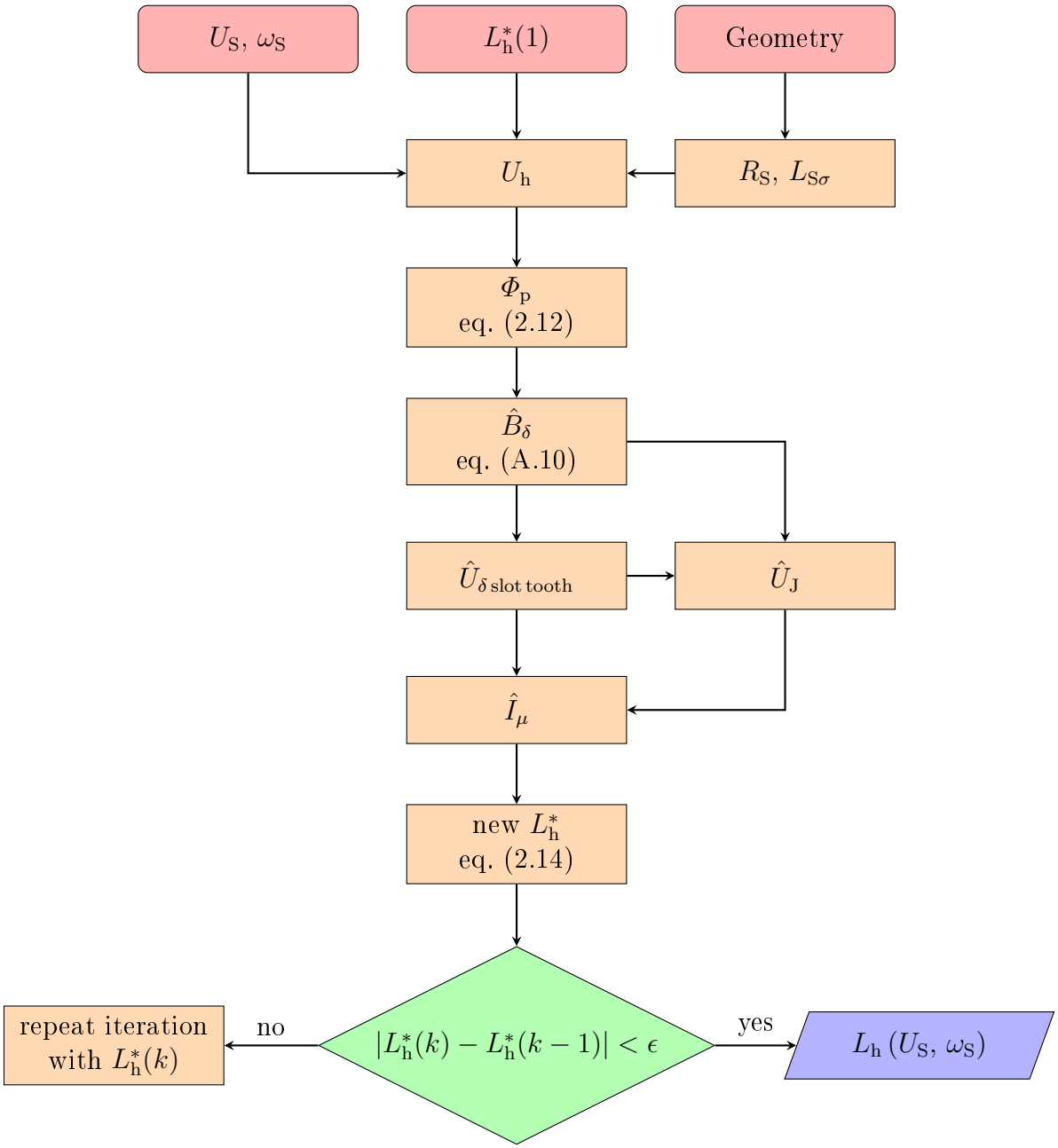

Figure 2.6: Schematic illustration of the iteration to compute the main inductance L_h for a given stator voltage and stator voltage angular frequency.

1. The no-load curve (I_μ as a function of U_S)
   At no-load the rotor does not carry any current and the parameters R_R and $L_{\mathrm{R}\sigma}$ (cf. Fig. A.2) do not have any impact. Thus, only two minimisation parameters $f_{\mathrm{L}_{\mathrm{S}\sigma}}$ and f_{L_h}, defined in eq. (2.17), are left over.

   Mathematically formulated, the problem yields

$$\min_{f_{\mathrm{L}_{\mathrm{S}\sigma}}\, f_{L_\mathrm{h}}} \chi^2 = \sum_i \frac{\left[I_\mu\left(U_\mathrm{S}\right)_\mathrm{i} - I_{\mu\,\mathrm{FEM}}\left(U_\mathrm{S}\right)_\mathrm{i}\right]^2}{\left[I_{\mu\,\mathrm{FEM}}\left(U_\mathrm{S}\right)_\mathrm{i}\right]^2} \quad . \tag{2.15}$$

   The result of the computation is illustrated in Fig. 2.7.

2. The current-slip (I_S as a function of s) and the torque-slip (T_motor as a function of s) curve

   For this minimisation the previously obtained results ($L_{\mathrm{S}\sigma\,\mathrm{fit}}$ and $L_{\mathrm{h\,fit}}$) are used. Therefore, again only two parameters, $f_{\mathrm{L}_{\mathrm{R}\sigma}}$ and f_{R_R} defined in eq. (2.17), have to be varied. The challenge of this problem is that both, the current-slip and the torque-slip curve, should be in good agreement with the finite element analysis, which can be formulated mathematically as

$$\min_{f_{\mathrm{L}_{\mathrm{R}\sigma}}\, f_{R_\mathrm{R}}} \chi^2 = \sum_i \frac{\left[I_\mathrm{S}\left(s\right)_\mathrm{i} - I_{\mathrm{S\,FEM}}\left(s\right)_\mathrm{i}\right]^2}{\left[I_{\mathrm{S\,FEM}}\left(s\right)_\mathrm{i}\right]^2} + \frac{\left[T_\mathrm{motor}\left(s\right)_\mathrm{i} - T_{\mathrm{motor\ FEM}}\left(s\right)_\mathrm{i}\right]^2}{\left[T_{\mathrm{motor\ FEM}}\left(s\right)_\mathrm{i}\right]^2} \quad . \tag{2.16}$$

   The results of the computation are shown in Figs. 2.8 and 2.9.

An important part of the minimisation is to set physically reasonable constraints for the factors, given in eq. (2.17), because even if the result of the minimisation would describe the data of the finite element analysis perfectly it need not be correct.

$$L_{\mathrm{S}\sigma\,\mathrm{fit}} = f_{\mathrm{L}_{\mathrm{S}\sigma}} L_{\mathrm{S}\sigma} \qquad L_{\mathrm{h\,fit}} = f_{L_\mathrm{h}} L_\mathrm{h} \qquad L_{\mathrm{R}\sigma\,\mathrm{fit}} = f_{\mathrm{L}_{\mathrm{R}\sigma}} L_{\mathrm{R}\sigma} \qquad R_{\mathrm{R\,fit}} = f_{R_\mathrm{R}} R_\mathrm{R} \tag{2.17}$$

The result of the minimisation of eqs. (2.15) to (2.17) used for the graphs in Figs. 2.7 to 2.9, are presented in Table 2.2. These values are also used for the loss computation of the final machine design resulting from the GA (see Section 4.1.2).

Table 2.2: Result of the minimisation of eqs. (2.15) to (2.17). The underlying geometry is the final machine design, shown in Fig. 4.3.

Parameter	Value
$f_{\mathrm{L}_{\mathrm{S}\sigma}}$	1.49
f_{L_h}	0.92
$f_{\mathrm{L}_{\mathrm{R}\sigma}}$	1.32
f_{R_R}	1.03

2.2.1.4 Computation of the Mass Moment of Inertia

For an application, which demands a high degree of dynamic, the mass moment of inertia is a key parameter for the machine design. Certainly, to obtain reasonable simulation results an accurate knowledge of this parameter is indispensable.

The geometry of the IM (c.f. Fig. 4.3) allows to compute its mass moment of inertia analytically using the parallel-axis theorem. For the computation of a more complex object see Section 3.2.4.

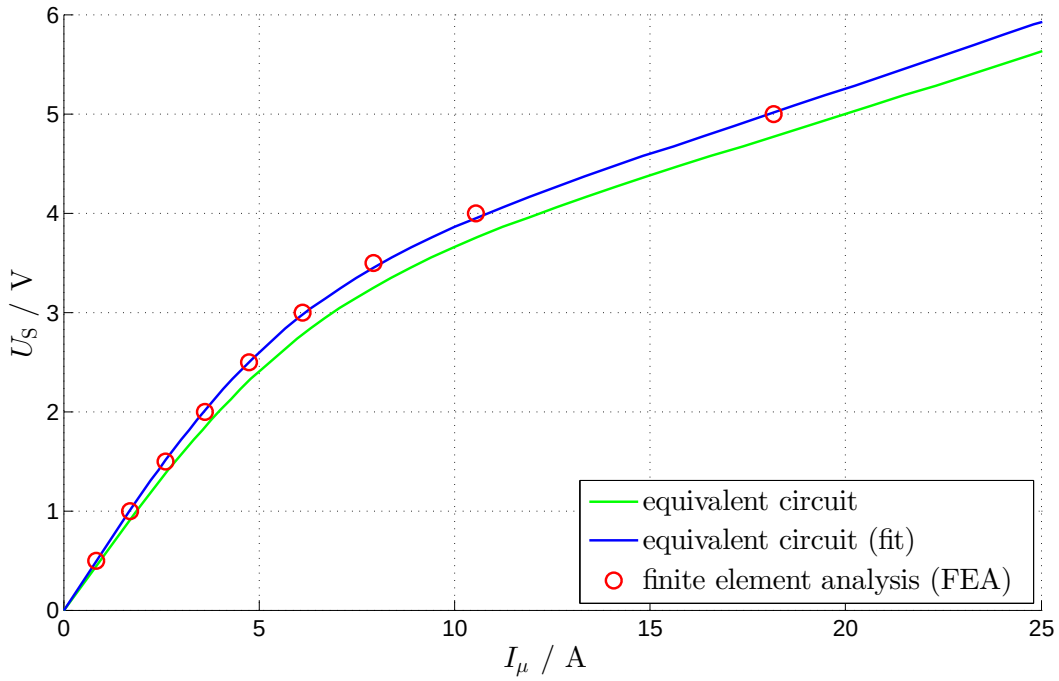

Figure 2.7: The green line indicates the no-load curve calculated using the equivalent circuit parameters as described in this Section, the red rings show the results of a finite element analysis and the blue line is computed with the optimised parameters, according to eq. (2.15). The stator voltage frequency of the computation is 50 Hz.

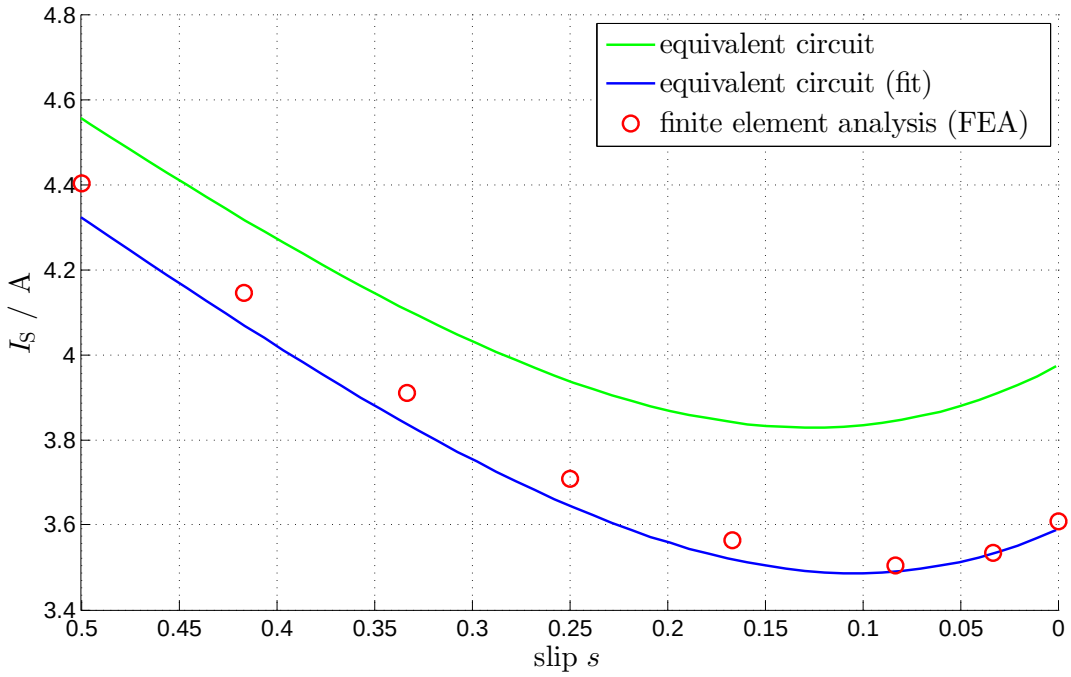

Figure 2.8: The green line indicates the current-slip curve calculated using the equivalent circuit parameters as described in this Section, the red rings show the results of a finite element analysis and the blue line is computed with the optimised parameters, according to eq. (2.16). The stator voltage of the computation is 2 V and its frequency 50 Hz.

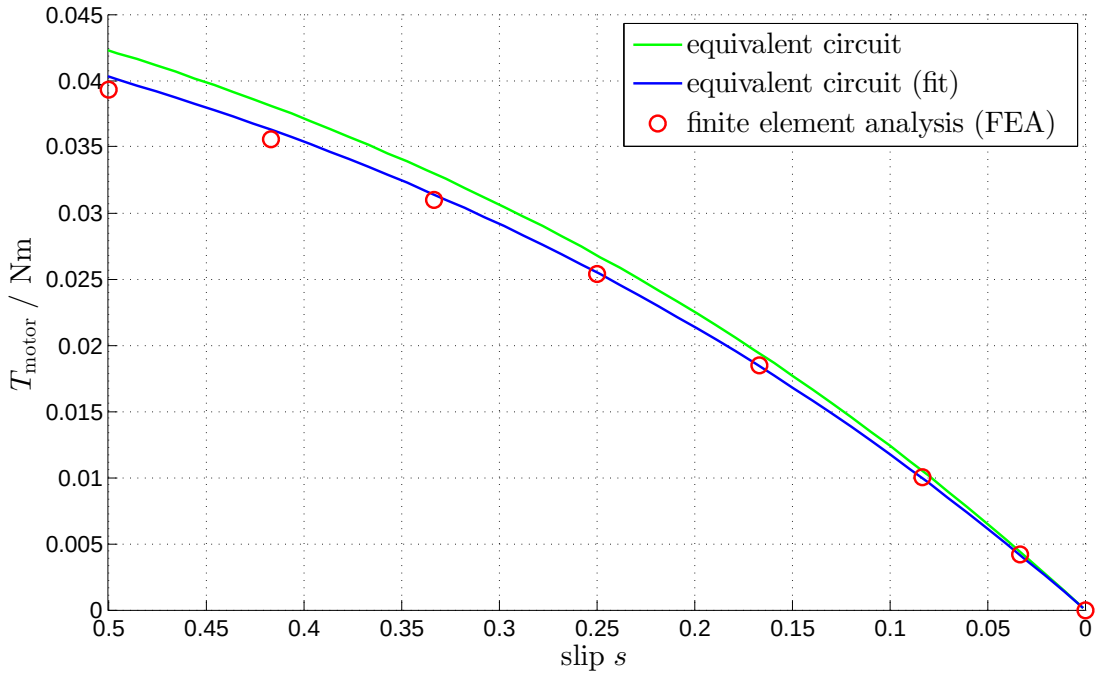

Figure 2.9: The green line indicates the current-torque curve calculated using the equivalent circuit parameters as described in this Section, the red rings show the results of a finite element analysis and the blue line is computed with the optimised parameters, according to eq. (2.16). The stator voltage of the computation is 2 V and its frequency 50 Hz.

2.3 Field Oriented Control (FOC)

Field oriented control for IMs first proposed by Hasse [43], respectively Blaschke [44], enables IM for high dynamic operation. The mathematical background is derived in Appendix A.4 and gives an overview of FOC of an IM. Section 2.3.1 treats the design of the controller and a method to estimate the nominal value of the rotor flux for minimum loss operation at a given load is presented in Section 2.3.2.

2.3.1 Controller Design

For controlling an electrical machine it is preferable to be able to adjust the magnetic flux and torque independently of each other, similar to a separately excited DC machine. This aim can be achieved by transforming eqs. (A.22) to (A.25) into the rotor flux oriented coordinate system (ΨCS).

A schematic overview of the implemented controller design is illustrated in Fig. 2.10. It consists of a current controller, a superposed speed, respectively flux controller and a position controller. This kind of cascaded controller design [45, 46] has the advantage that the controllers can be designed from the inside out. The details of the underlying FOC are not shown, due to reasons of confidentiality.

Except for the position controller, proportional-integral (PI) controllers including Anti-Windup [47] strategies are used. In general, the relation of input $e(t)$ and output $u(t)$ of a PI controller is given by

$$u\left(t\right) = k_{\mathrm{P}} \left[e\left(t\right) + \frac{1}{T_{\mathrm{I}}} \int_0^t e\left(\tau\right) d\tau \right] \quad . \tag{2.18}$$

In this context, k_{P} represents the controller's gain, a tuning parameter of the proportional part and T_{I}, the reset time, a tuning parameter of the integral part of the controller. The transfer function $R(s)$, the Laplace transformation of eq. (2.18), results in

$$G_{\mathrm{R}}\left(s\right) = \frac{u\left(s\right)}{e\left(s\right)} = k_{\mathrm{P}} \left(1 + \frac{1}{s\, T_{\mathrm{I}}} \right) \quad . \tag{2.19}$$

The tuning parameters of the controllers have to be adjusted to their control paths, shown below.

- Current controller

  After subtracting the compensation voltage from eq. (A.42) the control path for the d-current-controller[2] results in

  $$u_{\mathrm{Sd}}(t) = R\, i_{\mathrm{Sd}}(t) + L_\sigma \frac{d}{dt} i_{\mathrm{Sd}}\left(t\right) \quad \circ\!\!-\!\!\bullet \quad u_{\mathrm{Sd}}(s) = R\, i_{\mathrm{Sd}}(s) + L_\sigma\, s\, i_{\mathrm{Sd}}\left(s\right) \quad ,$$

  and accordingly the transfer function

  $$G_{\mathrm{S}}\left(s\right) = \frac{i_{\mathrm{Sd}}\left(s\right)}{u_{\mathrm{Sd}}\left(s\right)} = \frac{1}{R + s\, L_\sigma} = \frac{1}{R} \frac{1}{1 + s \underbrace{\frac{L_\sigma}{R}}_{T_{\mathrm{C}}}} = \frac{1}{R} \frac{1}{1 + s\, T_{\mathrm{C}}} \tag{2.20}$$

[2] Non-linearities of the power converter are neglected in this consideration.

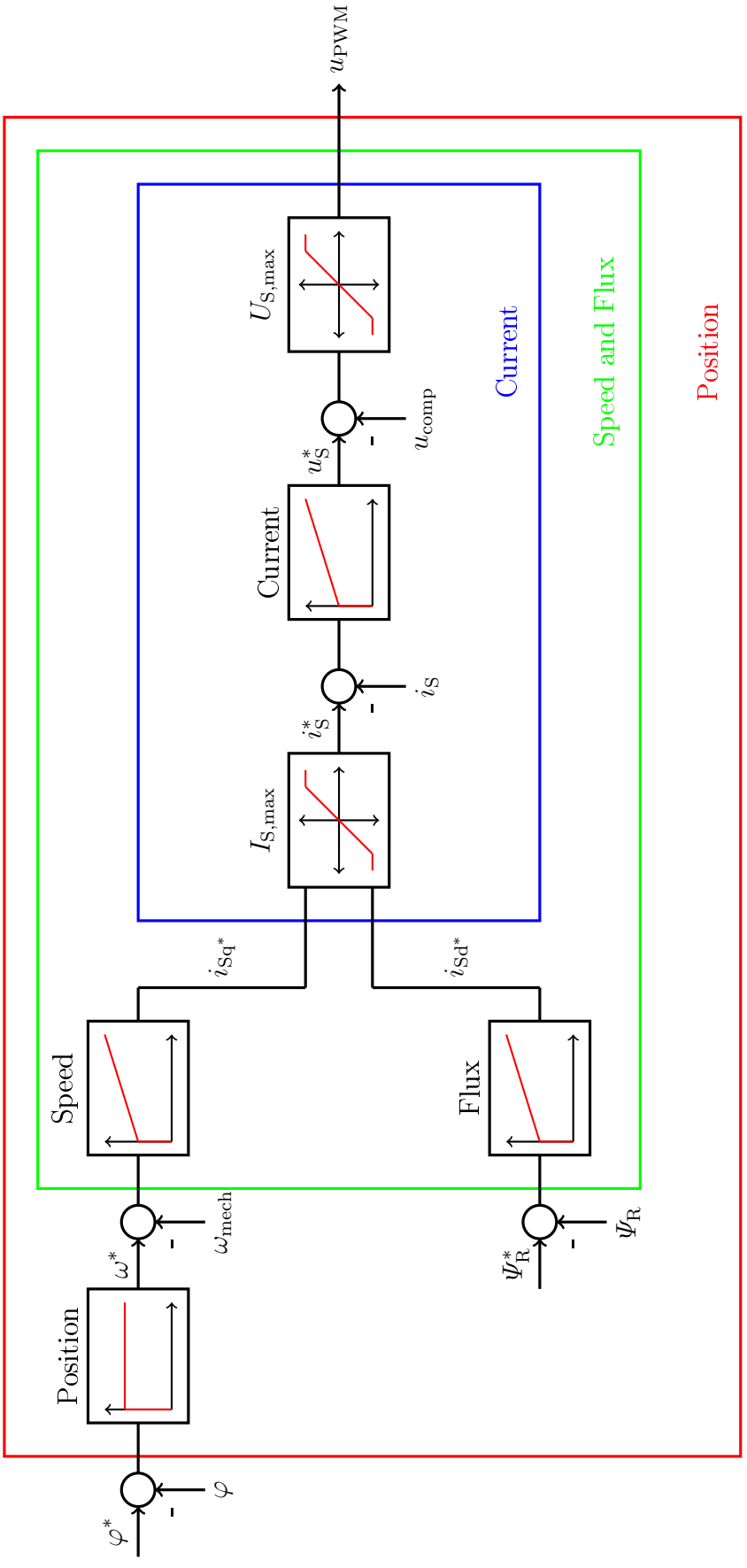

Figure 2.10: Schematic illustration of the cascaded controller for the induction motor. The details of the underlying FOC are not shown, due to reasons of confidentiality. The command variables are marked with a $*$ superscript. $I_{\mathrm{S,max}}$ and $U_{\mathrm{S,max}}$ denote the maximum value of current and voltage of the power converter respectively, u_{PWM} the output voltage of the pulse modulated inverter. The actual position φ and speed ω_{mech} are obtained from a rotary encoder.

is obtained. Through reducing the dominant pole, the open loop transfer function G_0 gives,

$$G_0(s) = G_R G_S = \frac{k_P}{R}\frac{1+sT_I}{sT_I}\frac{1}{1+sT_C} \overset{T_I=T_C}{=} \frac{k_P}{R}\frac{1}{sT_I} \quad . \tag{2.21}$$

The magnitude optimum criterion [46, Chapter 3] does not provide a unique solution for the transfer function in eq. (2.21), which means the parameter k_p and accordingly the gain crossover frequency can be chosen arbitrarily from that point of view. In practice, k_p should be fitted to the system requirements.

The control path for the q-current-controller is identical to that of the d-current (cf. eq. (A.41)), which means two identical controllers have to be implemented. One to control i_{Sd}, the other for i_{Sq}.

Since every power converter is restricted to a certain maximum of current $I_{S,max}$ and voltage $U_{S,max}$ these conditions,

$$I_{S,max} \geq \sqrt{{i^*_{Sd}}^2 + {i^*_{Sq}}^2} \quad \text{and} \quad U_{S,max} \geq \sqrt{{u^*_{Sd}}^2 + {u^*_{Sq}}^2} \quad ,$$

have to be considered in the controller design as well[3].

One possible strategy to realise the controller is outlined in the following.

- The rotor flux Ψ_R is set to a constant value, thus eq. (A.44) reduces to

$$\dot{\Psi}_{Rd} = 0 = \frac{R_R}{L_h + L_{R\sigma}}(L_h i_{Sd} - \Psi_{Rd}) \quad , \tag{2.22}$$

  and causes a specific value of i^*_{Sd}, which is also constant.

- To control the q-component a method similar to the one presented in [48] is implemented. But, in contrast to [48], in this controller design, priority is given to the d-component of the current and only the rest of the current reserve is available for i^*_{Sq} to generate torque (cf. eq. (A.46)), which means

$$i^*_{Sq,max} = \sqrt{I^2_{S,max} + {i^*_{Sd}}^2} \quad .$$

The voltage limitation is implemented exactly in the same manner.

- Flux controller

The rotor flux control path is given by eq. (A.44),

$$\frac{d}{dt}\Psi_R(t) = \frac{R_R}{L_h + L_{R\sigma}}(L_h i_{Sd}(t) - \Psi_R(t)) \quad \circ\!\!-\!\!\bullet$$

$$s\Psi_R(s) = \frac{R_R}{L_h + L_{R\sigma}}(L_h i_{Sd}(s) - \Psi_R(s)) \quad ,$$

which results in the transfer function

$$G_S(s) = \frac{\Psi_R(s)}{i_{Sd}(s)} = \frac{L_h}{1 + s\underbrace{\frac{L_h + L_{R\sigma}}{R_R}}_{T_\Psi}} = L_h\frac{1}{1+sT_\Psi} \quad . \tag{2.23}$$

[3] Command variables are marked with a $*$ superscript.

Eq. (2.23) has the same structure as eq. (2.20) and thus the tuning parameters of the controller are also chosen in the same manner.

As already mentioned, during operation, the rotor flux is set to a certain constant value Ψ_{R}^*. Research has shown that the copper losses during the driving cycle are highly affected by Ψ_{R}^*. This is discussed in more detail in Section 2.3.2.

- Speed controller

  Assuming a constant rotor flux and a rotor flux oriented coordinate system, the torque of the induction machine is proportional to i_{Sq}, as described in eq. (A.46). Therefore, a torque demand causes a required q-current, which is realised by the subordinated current controller.

  The delay of the rotational speed relative to the torque, caused by the mechanical inertia of the system and the subordinated current controller makes the computation of the tuning parameters of the speed controller more complex than the one of the current or the flux because an exact knowledge of the control path is needed. This topic is not discussed at this point.

  Another more practice-related method to determine the tuning parameters of a controller was introduced by Ziegler and Nichols [49] and was used to estimate the parameters for the speed controller. In short, this method uses simple experiments/simulations to obtain information on the dynamic behaviour of the system and is used to determine the tuning parameters of the controller in this work.

- Position controller

  The position controller is implemented as a proportional controller, because its control path already contains an integral part,

$$\varphi(t) \;=\; \int_0^t \omega(\tau) d\tau \quad .$$

  To avoid overshooting the deceleration of the machine has to be considered in the controller design as well. Assuming constant deceleration, the output of the position controller ω^* is limited by the motor torque and mass moment of inertia of the system,

$$\omega^* \;=\; \sqrt{2\,\dot{\omega}\,\Delta\varphi} \;=\; \sqrt{2\,\frac{T_{\mathrm{motor}}}{I}\,\Delta\varphi} \quad .$$

  Using this approach, ω^* is proportional to the square root of the control deviation $\Delta\varphi = (\varphi^* - \varphi)$.

  To also ensure a suitable controller performance for small deviations $\Delta\varphi$ a linear part also is implemented in addition.

$$\omega^* \;=\; \begin{cases} \mathrm{sgn}(\Delta\varphi)\, k_{\mathrm{P}}\, |\Delta\varphi| & |\Delta\varphi| \le \varphi_0 \\ \mathrm{sgn}(\Delta\varphi)\, k_{\mathrm{P}}\, \sqrt{\varphi_0\, |\Delta\varphi|} & |\Delta\varphi| > \varphi_0 \end{cases} \tag{2.24}$$

  The tuning parameters, including some safety, can be estimated using Tables 1.1 and 1.2 and eq. (1.4), which result in

$$\varphi_0 \;\approx\; 1.3\,\frac{\Delta x}{k_{\mathrm{spindle}}} \;\approx\; 30\,^\circ \quad \text{and} \quad k_{\mathrm{P}} \;\le\; \sqrt{\frac{2\,T_{\mathrm{motor\ max}}}{\varphi_0\, I_{\mathrm{system}}}} \;\approx\; 350 \quad .$$

2.3.2 Flux Optimisation

Eq. (A.46) gives the torque of the induction machine in a reference frame oriented to the rotor flux,

$$T_{\text{motor}} = \frac{3}{2} p \frac{L_{\text{h}}}{L_{\text{h}} + L_{\text{R}\sigma}} \Psi_{\text{Rd}}^{\Psi} i_{\text{Sq}}^{\Psi} \quad .$$

The controller design (Section 2.3.1) implies that the rotor flux Ψ_{R} is controlled to be constant on its command value. Thereby, also the d-axis current i_{Sd} is determined. If the choice of Ψ_{R} does not fit to the actual operating point, it would cause more losses than necessary.

A controller design by adjusting the rotor flux to the torque and speed requirements can be obtained at the cost of a lower dynamic behaviour of the machine [50]. However, the idea to adjust Ψ_{R} to obtain minimal losses can be adopted for the complete cycle, at least on average. This can be achieved, either, via trial and error, through simulating or operating the machine for the given cycle and to calculate P_{Cu}, or using an approximation, presented below.

In the steady state, the copper losses of an induction machine are given by

$$P_{\text{Cu}} = \frac{3}{2} \left[R_{\text{S}} \left| i_{\text{S}} \right|^2 + R_{\text{R}} \left| i_{\text{R}} \right|^2 \right] \quad , \tag{2.25}$$

and eq. (2.22) for the rotor flux reduces to

$$\Psi_{\text{R}} = L_{\text{h}} \, i_{\text{Sd}} \quad . \tag{2.26}$$

A adaptation of eq. (A.25) gives an expression for the rotor current,

$$i_{\text{R}} = \frac{1}{L_{\text{h}} + L_{\text{R}\sigma}} \Psi_{\text{R}} - \frac{L_{\text{h}}}{L_{\text{h}} + L_{\text{R}\sigma}} i_{\text{S}} = \frac{L_{\text{h}}}{L_{\text{h}} + L_{\text{R}\sigma}} i_{\text{Sd}} - \frac{L_{\text{h}}}{L_{\text{h}} + L_{\text{R}\sigma}} \left(i_{\text{Sd}} + \mathrm{i} \, i_{\text{Sq}} \right) \quad , \tag{2.27}$$

in the rotor flux oriented reference frame. Combining eqs. (2.26) and (2.27) with eq. (2.25) results in

$$P_{\text{Cu}} = \frac{3}{2} \left[R_{\text{S}} \left(i_{\text{Sd}}^2 + i_{\text{Sq}}^2 \right) + R_{\text{R}} \frac{L_{\text{h}}^2}{(L_{\text{h}} + L_{\text{R}\sigma})^2} i_{\text{Sq}}^2 \right] \quad . \tag{2.28}$$

If additionally the torque, eq. (A.46),

$$T_{\text{RMS}} = \frac{3}{2} p \frac{L_{\text{h}}}{L_{\text{h}} + L_{\text{R}\sigma}} \Psi_{\text{R}} \, i_{\text{Sq}} \quad ,$$

is inserted into eq. (2.28), a relation between the copper losses and the effective torque T_{RMS} (= loss equivalent torque) of the given cycle (eq. (2.1)) as a function of i_{Sd} is obtained,

$$P_{\text{Cu}} = \frac{3}{2} R_{\text{S}} \, i_{\text{Sd}}^2 + \left(R_{\text{S}} + R_{\text{R}} \frac{L_{\text{h}}^2}{(L_{\text{h}} + L_{\text{R}\sigma})^2} \right) \frac{T_{\text{RMS}}^2 \, (L_{\text{h}} + L_{\text{R}\sigma})^2}{L_{\text{h}}^4 \, p^2} \frac{2}{3} \frac{1}{i_{\text{Sd}}^2} \quad . \tag{2.29}$$

If the main inductance is assumed constant, an analytic expression can be given for the optimal flux value $\Psi_{\text{R}\,\text{opt}}$, c.f. [51, Section 10.3.8],

$$\left. \frac{d}{d i_{\text{Sd}}} P_{\text{Cu}} \right|_{L_{\text{h}} = \text{const.}} \stackrel{!}{=} 0 = 3 \, R_{\text{S}} \, i_{\text{Sd}} - \left(R_{\text{S}} + R_{\text{R}} \frac{L_{\text{h}}^2}{(L_{\text{h}} + L_{\text{R}\sigma})^2} \right) \frac{T_{\text{RMS}}^2 \, (L_{\text{h}} + L_{\text{R}\sigma})^2}{L_{\text{h}}^4 \, p^2} \frac{4}{3} \frac{1}{i_{\text{Sd}}^3}$$

$$\Rightarrow \Psi_{\text{R}\,\text{opt}} = \sqrt[4]{\left(\frac{(L_{\text{h}} + L_{\text{R}\sigma})^2}{p^2} + \frac{R_{\text{R}} \, L_{\text{h}}^2}{R_{\text{S}} \, p^2} \right) T_{\text{RMS}}^2 \frac{4}{9}} \quad . \tag{2.30}$$

Otherwise, if the non-linearity of L_h is considered, the minimisation problem

$$\min_{i_\mathrm{Sd}} P_\mathrm{Cu} = \frac{3}{2} R_\mathrm{S} i_\mathrm{Sd}^2 + \left(R_\mathrm{S} + R_\mathrm{R} \frac{L_\mathrm{h}^2 (i_\mathrm{Sd})}{(L_\mathrm{h} (i_\mathrm{Sd}) + L_{\mathrm{R}\sigma})^2} \right) \frac{T_\mathrm{RMS}^2 (L_\mathrm{h} (i_\mathrm{Sd}) + L_{\mathrm{R}\sigma})^2}{L_\mathrm{h}^4 (i_\mathrm{Sd}) p^2} \frac{2}{3} \frac{1}{i_\mathrm{Sd}^2} \quad , \quad (2.31)$$

has to be solved numerically.

Fig. 2.11 shows simulation results of the average copper loss $\overline{P_\mathrm{Cu}}$ (red line) of an induction machine to run through the cycle as a function of the rotor flux Ψ_R. As already mentioned, $\overline{P_\mathrm{Cu}}$ is highly affected by Ψ_R. The blue $\times$ indicates the approximation for the minimal loss nominal value of the rotor flux, according to eq. (2.31).

A further reduction of the copper losses could be achieved by reducing the nominal value of the rotor flux during the still standing phases of the cycle (in the extreme case to zero), similar to *zero torque control*, presented in Section 5.2.5. This modification of the controller design was tested in preliminary studies with the result that the required dynamic behaviour cannot be achieved, if the duration of the resting phases is not known. Note, the specified cycle is only used as a starting point for the design process. For the final application, the actuator should be able to move to any position within its defined adjusting range and tolerances. Therefore this control strategy would, in principle, be applicable for the specific cycle, but not for the final application of the actuator.

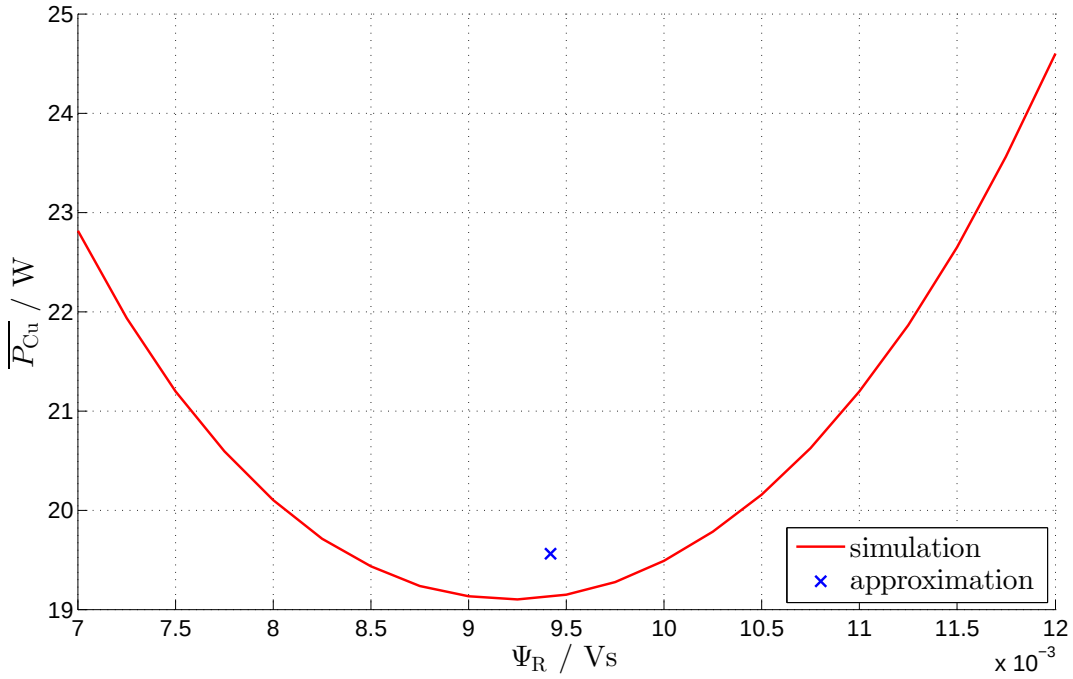

Figure 2.11: Simulation results of the average copper loss $\overline{P_\mathrm{Cu}}$ (red line) of the induction machine, defined in Table 4.3, to run through the cycle as a function of the rotor flux Ψ_R. The blue $\times$ indicates the approximation for the minimal loss nominal value of the rotor flux, according to eq. (2.31).

Chapter 3

Synchronous Reluctance Machine Modelling

The first Section of this Chapter treats some basics of the Synchronous Reluctance Machine (SynRM), the d-q-model and the torque equations. Section 3.2 describes an analytical model to estimate the magnetising inductances in direct (d) and quadrature (q) axis for the use within the GA loss minimisation routine (c.f. Section 4.2)[1]. The controller design for the SynRM is presented in Section 3.3, followed by a modelling approach to consider cross saturation based on finite element analysis in Section 3.4. This modelling approach is used for the comparison with measurement results in Section 5.3.

3.1 Basic Principles

The working principle of a cageless-rotor synchronous reluctance machine is based on the anisotropy of its rotor [9], typically realised by internal rotor flux barriers. The only contribution to its torque originates from the reluctance torque, due to the different magnetic resistances in direct d- and q-axis. The winding of the stator is similarly structured like that of an induction machine and is the only current-carrying part.

If core losses can be neglected, as in the case of this application, the voltage equations [52] in stator fixed reference frame[2] (a-b) are given by eqs. (3.1) to (3.3).

$$u_{\mathrm{S}}^{\mathrm{S}} = i_{\mathrm{S}}^{\mathrm{S}} R_{\mathrm{S}} + \frac{d\Psi^{\mathrm{S}}}{dt} \tag{3.1}$$

$$\omega_{\mathrm{R}} = p\,\omega_{\mathrm{mech}} \tag{3.2}$$

$$\beta_{\mathrm{R}} = \beta_{\mathrm{R0}} + \int_0^t \omega_{\mathrm{R}}(\tau)\,d\tau \tag{3.3}$$

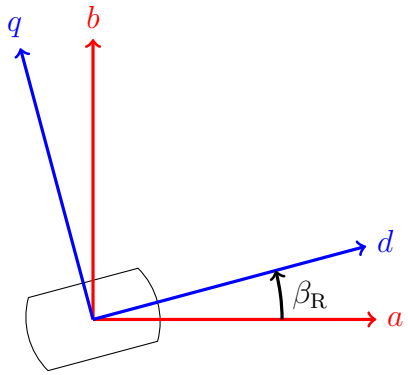

Figure 3.1: Illustration of the relation between the stator (a-b) and the rotor fixed d-q coordinate system.

[1] Note, within the presented analytical model L_{d} and L_{q} are assuemed to be constant.
[2] The superscript denotes in which coordinate system the variable is defined (S ...stator, R ...rotor)

Transforming eq. (3.1) into the rotor fixed coordinate system, using eq. (A.26), results in

$$\begin{aligned} u_{\mathrm{S}}^{\mathrm{R}}\,\mathrm{e}^{\mathrm{i}\,\beta_{\mathrm{R}}} &= i_{\mathrm{S}}^{\mathrm{R}}\,R_{\mathrm{S}}\,\mathrm{e}^{\mathrm{i}\,\beta_{\mathrm{R}}} + \frac{d}{dt}\left(\Psi^{\mathrm{R}}\,\mathrm{e}^{\mathrm{i}\,\beta_R}\right) \\ u_{\mathrm{S}}^{\mathrm{R}} &= i_{\mathrm{S}}^{\mathrm{R}}\,R_{\mathrm{S}} + \dot{\Psi}^{\mathrm{R}} + \mathrm{i}\,\Psi^{\mathrm{R}}\,\underbrace{\frac{d\beta_{\mathrm{R}}}{dt}}_{\omega_{\mathrm{R}}} \quad . \end{aligned} \tag{3.4}$$

Splitting eq. (3.4) into its real (d) and imaginary (q) part yields the d-q-model equations:

$$\dot{\Psi}_{\mathrm{d}} = u_{\mathrm{d}} - i_{\mathrm{d}}\,R_{\mathrm{S}} + \omega_{\mathrm{R}}\,\Psi_{\mathrm{q}} \quad , \quad \Psi_{\mathrm{d}} = L_{\mathrm{d}}\,i_{\mathrm{d}} \tag{3.5}$$

$$\dot{\Psi}_{\mathrm{q}} = u_{\mathrm{q}} - i_{\mathrm{q}}\,R_{\mathrm{S}} - \omega_{\mathrm{R}}\,\Psi_{\mathrm{d}} \quad , \quad \Psi_{\mathrm{q}} = L_{\mathrm{q}}\,i_{\mathrm{q}} \tag{3.6}$$

The corresponding space phasor diagram is shown in Fig. 3.2. Per definition, L_{d} and L_{q} include the magnetising inductance for the corresponding direction and the leakage inductance of the stator.

$$i_{\mathrm{S}} = i_{\mathrm{d}} + \mathrm{i}\,i_{\mathrm{q}} \tag{3.7}$$

$$\beta = \arctan\frac{i_{\mathrm{q}}}{i_{\mathrm{d}}} \tag{3.8}$$

$$\Psi_{\mathrm{h}} = \Psi_{\mathrm{d}} + \mathrm{i}\,\Psi_{\mathrm{q}} \tag{3.9}$$

$$\gamma = \arctan\frac{\Psi_{\mathrm{q}}}{\Psi_{\mathrm{d}}} \tag{3.10}$$

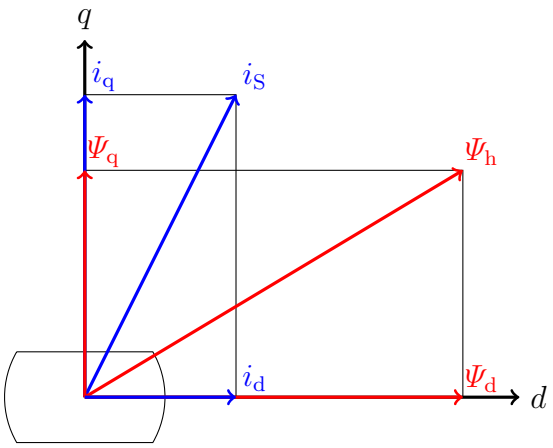

Figure 3.2: Space phasor diagramm fixed in the rotor reference frame.

For simulations it is essential to compute the inductances L_{d} and L_{q} as accurately as possible. However, L_{d} is influenced not only by i_{d} but also by i_{q} and vice versa [53].

$$\Psi_{\mathrm{d}} = L_{\mathrm{d}}(i_{\mathrm{d}}, i_{\mathrm{q}})\,i_{\mathrm{d}} \quad , \quad \Psi_{\mathrm{q}} = L_{\mathrm{q}}(i_{\mathrm{d}}, i_{\mathrm{q}})\,i_{\mathrm{q}} \tag{3.11}$$

This so called cross magnetic saturation can be considered in simulations using a two-dimensional lookup table extracted from finite element calculations.

For steady-state, eqs. (3.5) and (3.6) respectively reduce to

$$U_{\mathrm{d}} = I_{\mathrm{d}}\,R_{\mathrm{S}} - \omega_{\mathrm{R}}\,L_{\mathrm{q}}I_{\mathrm{q}} \quad \text{and} \quad U_{\mathrm{q}} = I_{\mathrm{q}}\,R_{\mathrm{S}} + \omega_{\mathrm{R}}\,L_{\mathrm{d}}I_{\mathrm{d}} \quad .$$

The torque generated by the machine can be derived from the effective power balance according to [54, Chapter 10.2].

$$\begin{aligned} T_{\mathrm{motor}} &= \frac{P}{\omega_{\mathrm{mech}}} = \frac{3}{\omega_{\mathrm{mech}}}\left[\Re(\underline{U}\,\underline{I}^{*}) - \underline{I}^{2}\,R_{\mathrm{S}}\right] = \frac{3}{\omega_{\mathrm{mech}}}\left[U_{\mathrm{d}}\,I_{\mathrm{d}} + U_{\mathrm{q}}\,I_{\mathrm{q}} - R_{\mathrm{S}}(I_{\mathrm{d}}^2 + I_{\mathrm{q}}^2)\right] \\ &= \frac{3}{\omega_{\mathrm{mech}}}\left(-\omega_{\mathrm{R}}\,L_{\mathrm{q}}I_{\mathrm{q}}\,I_{\mathrm{d}} + \omega_{\mathrm{R}}\,L_{\mathrm{d}}I_{\mathrm{d}}I_{\mathrm{q}}\right) \\ &= 3\,p\,\left(L_{\mathrm{d}} - L_{\mathrm{q}}\right)\,I_{\mathrm{d}}\,I_{\mathrm{q}} = \frac{3}{2}\,p\,\left(L_{\mathrm{d}} - L_{\mathrm{q}}\right)\,i_{\mathrm{d}}\,i_{\mathrm{q}} \end{aligned} \tag{3.12}$$

Two aspects essential for the machine design follow directly from eq. (3.12).

1. The inductance difference between d and q-axis should be as large as possible to achieve maximum torque within the limits of allowable volume. This is achieved using so called flux barriers in the rotor. The optimal shape and number of the flux barriers have been discussed by various publications, e.g. [10, 55, 13].

2. Assuming a constant stator current $i_\mathrm{S} = \sqrt{i_\mathrm{d}^2 + i_\mathrm{q}^2}$ and constant inductances the machine produces its maximal torque if $i_\mathrm{d} = i_\mathrm{q}$. This may be taken into consideration in the controller design.

$$\begin{aligned} \frac{\partial}{\partial i_\mathrm{q}} T_\mathrm{motor} &= \frac{\partial}{\partial i_\mathrm{q}} \left(\frac{3}{2} p \left(L_\mathrm{d} - L_\mathrm{q} \right) \sqrt{i_\mathrm{S}^2 - i_\mathrm{q}^2}\, i_\mathrm{q} \right) \stackrel{!}{=} 0 \\ 0 &= -\frac{1}{2} \left(i_\mathrm{S}^2 - i_\mathrm{q}^2 \right)^{-\frac{1}{2}} 2\, i_\mathrm{q}^2 + \sqrt{i_\mathrm{S}^2 - i_\mathrm{q}^2} \\ i_\mathrm{q}^2 &= i_\mathrm{S}^2 - i_\mathrm{q}^2 = i_\mathrm{d}^2 \end{aligned} \tag{3.13}$$

3.2 Analytic Model

To compute L_d and L_q of a SynRM either analytic or finite element methods may be used. At this point, a gross analytic model to estimate the inductances of the SynRM is presented, whereby the d- and q-axis are treated separately and independently from each other, i.e., cross saturation (see eq. (3.11)) is not considered. This model is used within the GA-based minimisation routine (see Section 4.2).

For the rotor geometry, flux barriers of a certain number and width, with one width for a given design are used. The shape of the flux barriers is based on circles, as shown in Figs. 3.3a and 3.5a.

The method uses constant stator current as input to compute the magnetomotive force

$$\hat{\Theta} = \frac{3}{2} \frac{2}{\pi} \hat{I}_\mathrm{S} \frac{w_\mathrm{str}}{p} \quad . \tag{3.14}$$

To develop the analytic equations, the rotor cross section is simplified into segments and translated into an equivalent magnetic circuit (see Figs. 3.3 and 3.5). Because of symmetry, only half a pole has to be modelled.

A few assumptions have been made [56]:

1. The flux enters the rotor perpendicular to the air gap surface and only at specific positions.

2. The current linkage is sinusoidally distributed, but for the computation in the equivalent circuit an averaged value is used.

3. The surface of the stator is smooth, which means, no influence of slotting.

4. The magnetisation characteristic of the iron sheet is linear.

The challenge is the computation of the resistances in the magnet circuit, which depend, amongst others on the saturation of the machine and the magnetisation characteristic of the iron sheet. This topic is treated subsequently for d- and q-axis separately.

The equivalent magnetic circuit is solved by applying Kirchhoff's laws, which results in a system of linear equations. The outcome, the magnetic flux, is used to compute the flux density in the

air gap (see Figs. 3.4 and 3.6). The component of the fundamental wave $\hat{B}_{\delta 1}$ is extracted and used to calculate the main flux linkage

$$\Psi_{\mathrm{h}}(\hat{I}_{\mathrm{S}}, \beta) \;=\; \frac{2}{\pi}\,\tau_{\mathrm{p}}\,l_{\mathrm{Fe}}\,w_{\mathrm{str}}\,\xi\hat{B}_{\delta 1}(\hat{I}_{\mathrm{S}}, \beta) \quad , \tag{3.15}$$

and finally the magnetising inductance

$$L \;=\; \frac{\Psi_{\mathrm{h}}}{\hat{I}_{\mathrm{S}}} \quad .$$

In the following, the computation is shown for a rotor cross section with two flux barriers, but it is also adjustable for several barriers.

3.2.1 Direct - axis

For the calculation of the d-axis, the stator current phase angle β is zero, i.e., $\hat{I}_{\mathrm{S}} \;=\; \hat{I}_{\mathrm{d}}$. Thus, the distribution of the current linkage is given by

$$\Theta(\varphi) \;=\; \hat{\Theta}\,\cos(p\,\varphi) \quad .$$

The current linkages occurring in the equivalent circuit are averaged depending on the geometry (Fig. 3.3a) and are calculated as follows:

$$\varphi_{\mathrm{AB}} \;=\; (\varphi_{\mathrm{B1}} + \varphi_{\mathrm{A2}})\,\frac{1}{2} \tag{3.16}$$

$$\varphi_{\mathrm{BC}} \;=\; (\varphi_{\mathrm{C1}} + \varphi_{\mathrm{B2}})\,\frac{1}{2} \tag{3.17}$$

$$\Theta_{\mathrm{A}} \;=\; \frac{1}{\varphi_{\mathrm{AB}}}\int_{0}^{\varphi_{\mathrm{AB}}} \Theta(\varphi)d\varphi \tag{3.18}$$

$$\Theta_{\mathrm{B}} \;=\; \frac{1}{(\varphi_{\mathrm{BC}} - \varphi_{\mathrm{AB}})}\int_{\varphi_{\mathrm{AB}}}^{\varphi_{\mathrm{BC}}} \Theta(\varphi)d\varphi \tag{3.19}$$

$$\Theta_{\mathrm{C}} \;=\; \frac{1}{(\varphi_{\mathrm{C2}} - \varphi_{\mathrm{BC}}}\int_{\varphi_{\mathrm{BC}}}^{\varphi_{\mathrm{C2}}} \Theta(\varphi)d\varphi \tag{3.20}$$

The current linkage between φ_{C2} and $\pi/(2p)$ is neglected in this consideration.

The equivalent circuit contains two different types of magnetic resistances, R_{Jx} and R_{x}, treated in detail below. For the entire computation, the relative permeability is assumed with $\mu_{\mathrm{r}} = 310$.[3]

- $R_{\mathrm{Jx}},\; x \;\in [A, B, C]$

  R_{Jx} consider the magnetic voltage drop in the stator yoke.

$$\begin{aligned}
r_{\mathrm{J}} \;&=\; d_{\mathrm{SI}}/2 + h_{\mathrm{ST}} + h_{\mathrm{SJ}}/2 \\
R_{\mathrm{JA}} \;&=\; \frac{r_{\mathrm{J}}\,\Delta\varphi_{\mathrm{AB}}}{\mu_0\,\mu_{\mathrm{r}}\,h_{\mathrm{SJ}}\,l_{\mathrm{Fe}}} \quad , \quad \Delta\varphi_{\mathrm{AB}} \;=\; \frac{\varphi_{\mathrm{B1}} + \varphi_{\mathrm{B2}}}{2} - \frac{\varphi_{\mathrm{A2}}}{2} \\
R_{\mathrm{JB}} \;&=\; \frac{r_{\mathrm{J}}\,\Delta\varphi_{\mathrm{BC}}}{\mu_0\,\mu_{\mathrm{r}}\,h_{\mathrm{SJ}}\,l_{\mathrm{Fe}}} \quad , \quad \Delta\varphi_{\mathrm{BC}} \;=\; \frac{\varphi_{\mathrm{C1}} + \varphi_{\mathrm{C2}}}{2} - \frac{\varphi_{\mathrm{B1}} + \varphi_{\mathrm{B2}}}{2} \\
R_{\mathrm{JC}} \;&=\; \frac{r_{\mathrm{J}}\,\Delta\varphi_{\mathrm{C}}}{\mu_0\,\mu_{\mathrm{r}}\,h_{\mathrm{SJ}}\,l_{\mathrm{Fe}}} \quad , \quad \Delta\varphi_{\mathrm{C}} \;=\; \frac{\pi}{2\,p} - \frac{\varphi_{\mathrm{C1}} + \varphi_{\mathrm{C2}}}{2}
\end{aligned}$$

[3] This value originates from the assumed magnetisation characteristic of the iron sheet.

- $R_{\mathrm{x}},\ x \in [A, B, C]$

  R_{x} consists of the magnetic voltage drop of the flux path $R_{\mathrm{x,\,path}}$, the air gap $R_{\mathrm{x},\,\delta}$ and slot tooth layer $R_{\mathrm{x,\,slot\,tooth}}$. Due to the geometry, it is difficult to estimate these resistances accurately. In the computation, some degree of approximation is needed [57].

  The magnetic resistances of the flux paths are calculated via

$$R_{\mathrm{x,\,path}} = \frac{l_{\mathrm{arc\,eff}}}{\mu_0\,\mu_{\mathrm{r}}\,l_{\mathrm{Fe}}\,w_{\mathrm{path}}} \quad . \tag{3.21}$$

  In eq. (3.21), w_{path} denotes the minimum width and $l_{\mathrm{arc\,eff}}$ the effective length of the flux path. For path A, $l_{\mathrm{arc\,eff}}$ is taken to be 1/4 of the minimum arc length, for the others it is the mean length.

  The magnetic resistance of the air gap is computed as follows,

$$R_{\mathrm{x},\,\delta} = \frac{\delta\,k_{\mathrm{C}}}{\mu_0\,l_{\mathrm{Fe}}\,0.5\,d_{\mathrm{RO}}\,\Delta\varphi_{\mathrm{x}}} \quad \text{and} \tag{3.22}$$

  $\Delta\varphi_{\mathrm{x}}$ is defined according to

$$\begin{aligned}
\Delta\varphi_{\mathrm{A}} &= \frac{1}{2}\left(\varphi_{\mathrm{B1}} + \varphi_{\mathrm{A2}}\right) \quad , \\
\Delta\varphi_{\mathrm{B}} &= \frac{1}{2}\left(\varphi_{\mathrm{C1}} + \varphi_{\mathrm{B2}}\right) - \frac{1}{2}\left(\varphi_{\mathrm{B1}} + \varphi_{\mathrm{A2}}\right) \quad \text{and} \\
\Delta\varphi_{\mathrm{B}} &= \varphi_{\mathrm{C2}} - \frac{1}{2}\left(\varphi_{\mathrm{C1}} + \varphi_{\mathrm{B2}}\right) \quad .
\end{aligned}$$

  $R_{\mathrm{x,\,slot\,tooth}}$ considers the slotting of the stator and consequently higher flux densities and magnetic resistance per length compared to the yoke.

$$R_{\mathrm{A,\,slot\,tooth}} = \frac{h_{\mathrm{ST}}\,\tau_{\mathrm{SSP}}}{\mu_0\,\mu_{\mathrm{r}}\,l_{\mathrm{Fe}}\,0.5\,d_{\mathrm{SI}}\,\varphi_{\mathrm{A2}}\,a_{\mathrm{S}}} \tag{3.23}$$

$$R_{\mathrm{B,\,slot\,tooth}} = \frac{h_{\mathrm{ST}}\,\tau_{\mathrm{SSP}}}{\mu_0\,\mu_{\mathrm{r}}\,l_{\mathrm{Fe}}\,0.5\,d_{\mathrm{SI}}\,(\varphi_{\mathrm{B2}} - \varphi_{\mathrm{B1}})\,a_{\mathrm{S}}} \tag{3.24}$$

$$R_{\mathrm{C,\,slot\,tooth}} = \frac{h_{\mathrm{ST}}\,\tau_{\mathrm{SSP}}}{\mu_0\,\mu_{\mathrm{r}}\,l_{\mathrm{Fe}}\,0.5\,d_{\mathrm{SI}}\,(\varphi_{\mathrm{C2}} - \varphi_{\mathrm{C1}})\,a_{\mathrm{S}}} \tag{3.25}$$

  On average, the factor $a_{\mathrm{S}}/\tau_{\mathrm{SSP}}$ in eqs. (3.23) to (3.25) is the ratio between the area of the teeth and the entire area of the slot teeth layer.

The solution of the system of linear equations originating from the equivalent circuit is the magnetic fluxes $\Phi_{\mathrm{x}},\ x \in [A, B, C]$. They are used to compute the magnetic flux density in the

air gap as a function of the azimuthal angle φ.

$$
\begin{aligned}
B_\delta(\varphi) &= \frac{2\,\Phi_\mathrm{A}}{l_\mathrm{Fe}\,d_\delta\,\varphi_\mathrm{A2}} && , \quad 0 \leq \varphi < \varphi_\mathrm{A2} \\
B_\delta(\varphi) &= 0 && , \quad \varphi_\mathrm{A2} \leq \varphi < \varphi_\mathrm{B1} \\
B_\delta(\varphi) &= \frac{2\,\Phi_\mathrm{B}}{l_\mathrm{Fe}\,d_\delta\,(\varphi_\mathrm{B2} - \varphi_\mathrm{B1})} && , \quad \varphi_\mathrm{B1} \leq \varphi < \varphi_\mathrm{B2} \\
B_\delta(\varphi) &= 0 && , \quad \varphi_\mathrm{B2} \leq \varphi < \varphi_\mathrm{C1} \\
B_\delta(\varphi) &= \frac{2\,\Phi_\mathrm{C}}{l_\mathrm{Fe}\,d_\delta\,(\varphi_\mathrm{C2} - \varphi_\mathrm{C1})} && , \quad \varphi_\mathrm{C1} \leq \varphi < \varphi_\mathrm{C2} \\
B_\delta(\varphi) &= 0 && , \quad \varphi_\mathrm{C2} \leq \varphi < \frac{\pi}{2\,p}
\end{aligned}
$$

The result, shown in Fig. 3.4, is extrapolated for a complete pole pair and used to extract the component of the fundamental wave of the air gap flux density $\hat{B}_{\delta 1}$.

3.2.2 Quadrature - axis

For the computation of the q-axis, the stator current phase angle β is $\pi/2$, i.e., $\hat{I}_\mathrm{S} = \hat{I}_\mathrm{q}$. Thus, the distribution of the current linkage is given by

$$\Theta(\varphi) = \hat{\Theta}\,\sin(p\,\varphi) \quad .$$

The current linkages Θ_x, $x \in [A, B, C]$, occurring in the equivalent circuit are calculated according to eqs. (3.16) to (3.20). Θ_D, which is neglected in the consideration of the d-axis, is computed by

$$\Theta_\mathrm{D} = \frac{1}{(\frac{\pi}{2\,p} - \varphi_\mathrm{C2})} \int_{\varphi_\mathrm{C2}}^{\pi/2p} \hat{\Theta}\,\sin(p\,\varphi) d\varphi \quad . \tag{3.26}$$

For the computation of the equivalent circuit resistances, an infinite relative permeability of the ferromagnetic parts is assumed, except for the flux bridges. They are highly saturated for the given current linkage distribution.

Again, two different types of resistances, R_x and R_xy, can be distinguished within the equivalent circuit.

- R_x, $x \in [A, B, C, D]$

  R_x describes the magnetic voltage drop between rotor and stator, similar to $R_{\mathrm{x},\,\delta}$ in the computation of the d-axis. Though in this case, the flux bridges are saturated, which yield a larger resistance. For convenience, this is taken into account by assuming a relative permeability $\mu_\mathrm{r} = 1$ for regions between the flux barriers and the air gap.

$$R_\mathrm{A} = \frac{\delta\,k_\mathrm{C}}{\mu_0\,l_\mathrm{Fe}\,0.5\,d_\mathrm{RO}\,\varphi_\mathrm{A2}} \tag{3.27}$$

$$R_\mathrm{B} = \frac{\delta\,k_\mathrm{C}}{\mu_0\,l_\mathrm{Fe}\,0.5\,d_\mathrm{RO}\,(\varphi_\mathrm{B2} - \varphi_\mathrm{B1})} \tag{3.28}$$

$$R_\mathrm{C} = \frac{\delta\,k_\mathrm{C}}{\mu_0\,l_\mathrm{Fe}\,0.5\,d_\mathrm{RO}\,(\varphi_\mathrm{C2} - \varphi_\mathrm{C1})} \tag{3.29}$$

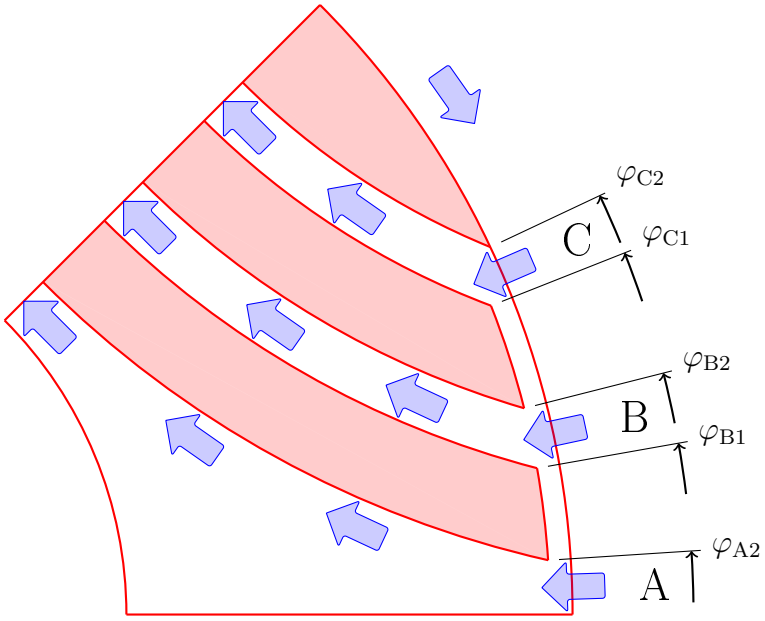

(a) Sketch of half a pole of the rotor cross section for the d-axis. The areas marked in red indicate material with $\mu_r = 1$, the white areas indicate iron and the blue arrows suggest the favoured direction of the magnetic flux.

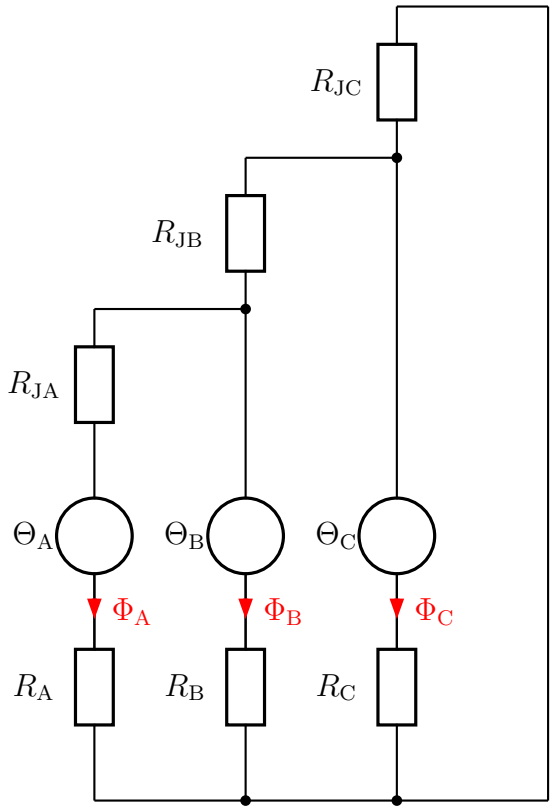

(b) Derived equivalent circuit for the d-axis from Fig. 3.3a.

Figure 3.3: Sketch of the rotor cross section and the derived equivalent circuit to compute the magnetising inductance for the d-axis.

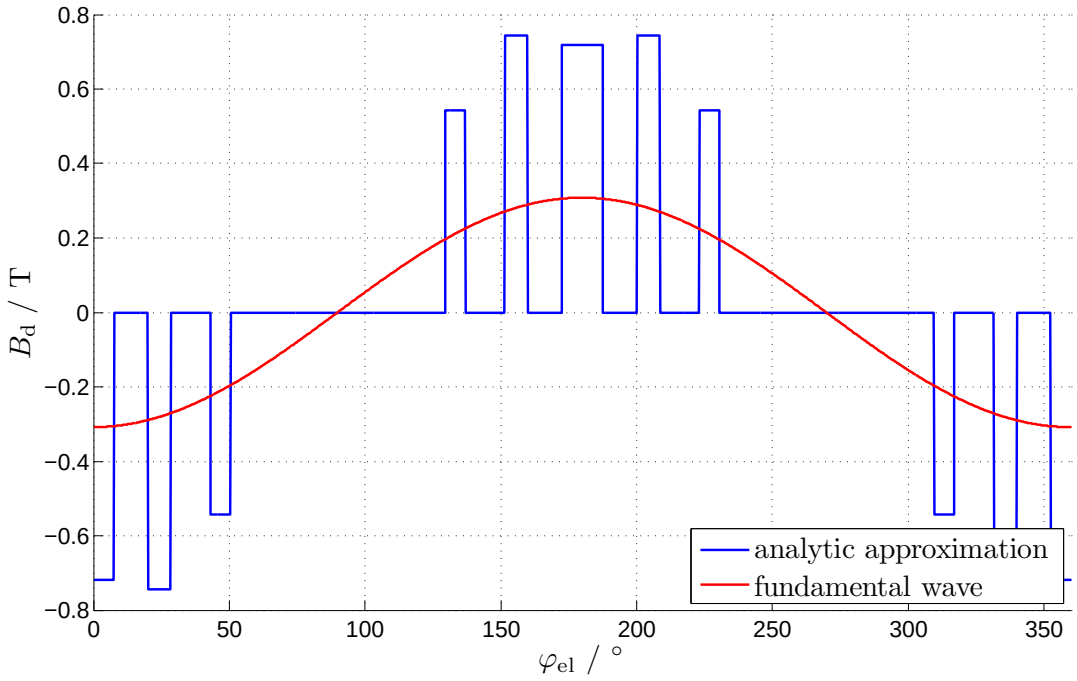

Figure 3.4: An example of the analytic approximation of the magnetic flux density in the air gap (blue line) and the corresponding fundamental wave (red line) for $\hat{I}_\mathrm{S} = \hat{I}_\mathrm{d}$.

An exception is given by the resistance R_D. For this case an additional flux barrier has to be considered, estimated with its average width $\overline{w}_\mathrm{barrier}$.

$$R_\mathrm{D} = \frac{\delta\, k_\mathrm{C} + \overline{w}_\mathrm{barrier}}{\mu_0\, l_\mathrm{Fe}\, 0.5\, d_\mathrm{RO}\, \left(\frac{\pi}{2p} - \varphi_\mathrm{C2}\right)} \tag{3.30}$$

- R_xy, x,y $\in [AB, BC]$

  These resistances correspond to the magnetic resistances between the flux paths A and B respectively B and C and are treated as a parallel connection of two resistances, R_bridge and R_barrier.

  Since the flux bridges are neglected in the computation of R_x, $x \in [A, B, C, D]$, they are considered in this case, computed according to

$$R_\mathrm{bridge} = \frac{w_\mathrm{barrier}}{\mu_0\, \mu_\mathrm{r,\,bridge}\, l_\mathrm{Fe}\, w_\mathrm{bridge}} \quad . \tag{3.31}$$

  In eq. (3.31), w_barrier denotes the width of the flux barrier and w_bridge the radial distance between the flux barrier and the air gap. $\mu_\mathrm{r,\,bridge}$ is a key parameter of the computation and may be determined with an educated guess or with the result of a finite element analysis.

  The computation of R_barrier is straight forward, using the mean length of the flux barrier $l_\mathrm{arc\,eff}$,

$$R_\mathrm{barrier} = \frac{w_\mathrm{barrier}}{\mu_0\, l_\mathrm{Fe}\, l_\mathrm{arc\,eff}} \quad .$$

The rest of the calculation is based on the same procedure as for the d-axis, except for the computation of the flux density in the air gap for an azimuthal angle $\varphi \geq \varphi_{C2}$. In contrast to the d-axis computation, it is given by

$$B_\delta(\varphi) = \frac{2\,\Phi_D}{l_{Fe}\,d_\delta\left(\frac{\pi}{2p} - \varphi_{C2}\right)} \quad , \quad \varphi_{C2} \leq \varphi < \frac{\pi}{2\,p} \quad .$$

Again the result, shown in Fig. 3.6, is extrapolated for a complete pole pair and the component of the fundamental wave $\hat{B}_{\delta 1}$ is extracted.

3.2.3 Comparison with FEM

A comparison of the presented analytic model and a finite element analysis for the magnetic flux density of the air gap as a function of the azimuthal angle φ is not expedient, because the presented method does not consider the slotting of the stator. But, if the component of the fundamental wave is also extracted from the FEM results and averaged over different rotor positions, the methods are comparable. For the FEM computations, again, transient simulations with fixed current and speed are performed.

Results for one specific operating point are shown in Table 3.1 and Fig. 3.9. Certainly, if the machine is more saturated, the results will differ more significantly, because within the analytical model, only a specific saturation state of the machine is considered.

Table 3.1: Comparison of the analytic model and a finite element analysis for the fundamental component of the flux density in the air gap $\hat{B}_{\delta 1}$ for one operating point (compare to Figs. 3.4 and 3.6).
Parameters of the computation: $\hat{\Theta} = 98\,\text{A}$, $d_\delta = 23\text{mm}$, $\mu_{r,\,\text{bridge}} = 30$, geometry according to Figs. 3.3a and 3.5a.

Axis	$\hat{B}_{\delta 1}$ FEM	$\hat{B}_{\delta 1}$ Analytic model
d	0.32 T	0.31 T
q	0.13 T	0.14 T

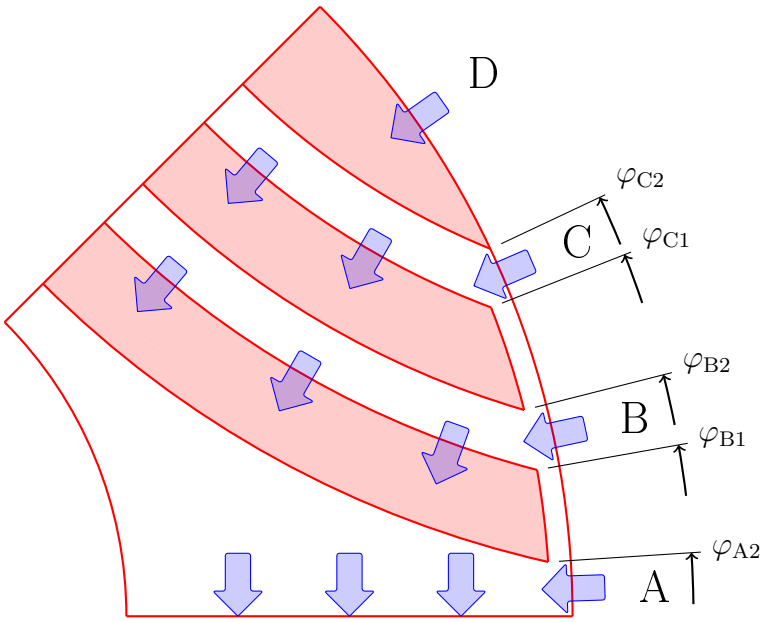

(a) Sketch of half a pole of the rotor cross section for the q-axis. The areas marked in red indicate material with $\mu_r = 1$, the white areas indicate iron and the blue arrows suggest the favoured direction of the magnetic flux.

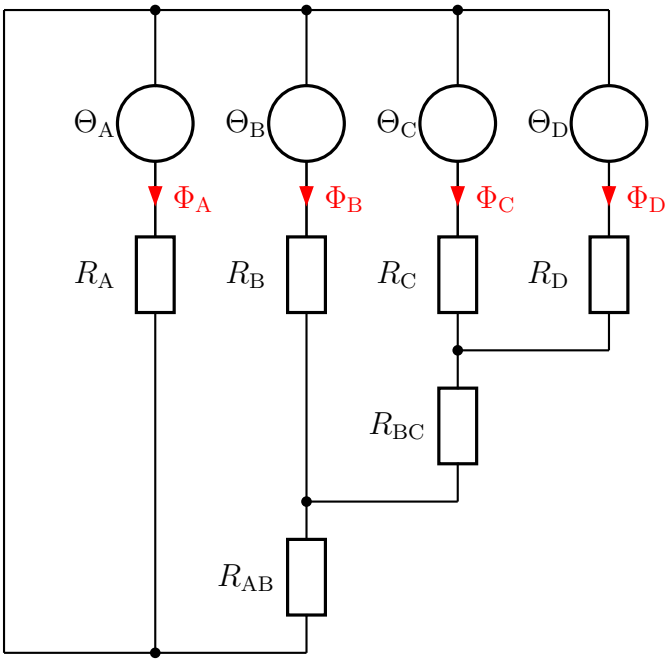

(b) Derived equivalent circuit for the q-axis from Fig. 3.5a.

Figure 3.5: Sketch of the rotor cross section and the derived equivalent circuit to compute the magnetising inductance for the q-axis.

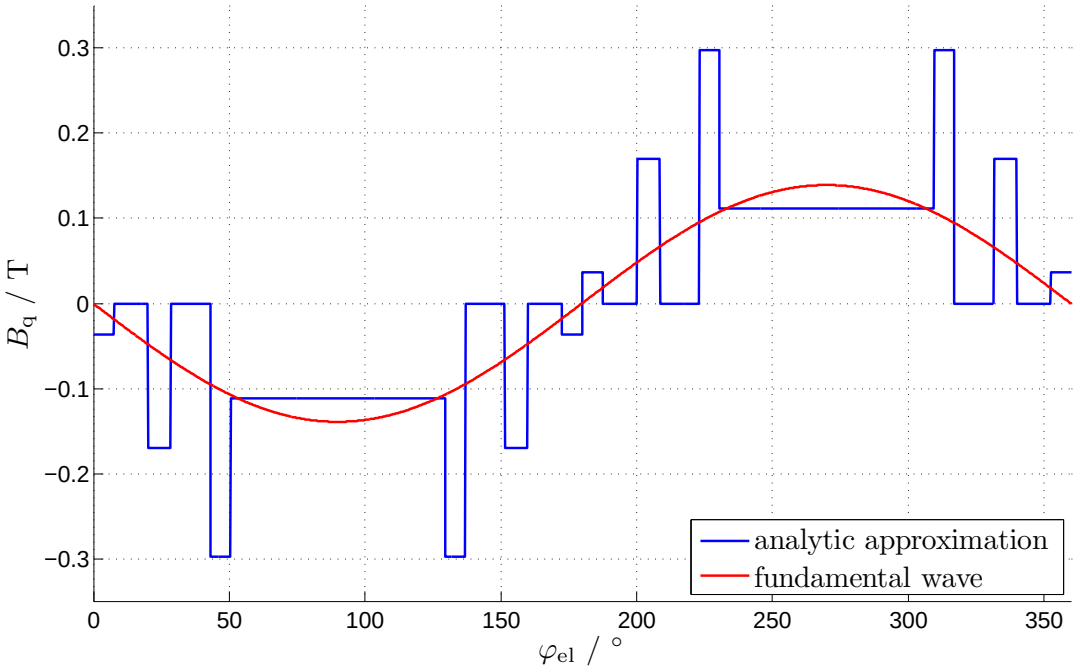

Figure 3.6: An example of the analytic approximation of the magnetic flux density in the air gap (blue line) and the corresponding fundamental wave (red line) for $\hat{I}_S = \hat{I}_q$.

3.2.4 Computation of the Mass Moment of Inertia

The mass moment of inertia I is computed, assuming a known mass distribution ρ_{mass}, by the volume integral

$$I = \rho_{mass} \int r^2 \, dV \quad . \tag{3.32}$$

For simple rotationally symmetrical objects eq. (3.32) can be solved analytically and/or using the parallel-axis theorem, discussed in various books on mechanics, such as [58].

If the geometry is more complex, such as the one of the selected rotor cross section of the SynRM, these analytic methods reach their limits and numerical methods have to be considered. A suitable approach is given by *simple monte carlo integration* [42, Chapter 7.7].

This algorithm is based on N uniformly distributed points $x_1, x_2, \ldots, x_N$ in a multidimensional volume V. It can be shown that,

$$\int f \, dV = V \langle f \rangle \pm \sqrt{\frac{\langle f^2 \rangle - \langle f \rangle^2}{N}} \quad .$$

In this case the angle brackets denote

$$\langle f \rangle = \frac{1}{N} \sum_{i=1}^{N} f(x_i) \quad \text{and} \quad \langle f^2 \rangle = \frac{1}{N} \sum_{i=1}^{N} f^2(x_i) \quad .$$

Applied to eq. (3.32), assuming that the random points are distributed in a square with side

length d_{RO}, yields

$$I = \rho_{\mathrm{mass}}\, l_{\mathrm{Fe}} \int r^2\, dA \approx \rho_{\mathrm{mass}}\, l_{\mathrm{Fe}}\, A_{\mathrm{rotor}}\, \langle r^2 \rangle = \rho_{\mathrm{mass}}\, l_{\mathrm{Fe}}\, d_{\mathrm{RO}}^2\, \frac{n}{N}\, \frac{1}{n} \sum_{i=1}^{n} r_{\mathrm{i}}^2 \quad . \tag{3.33}$$

In eq. (3.33), n is the number of points on the rotor cross section and r_{i} their radius. Points inside the flux barriers do not contribute to the moment of inertia.

3.3 Controller Design

The controller of the synchronous reluctance machine is similarly structured as the one of the IM (c.f. Section 2.3.1 and Fig. 2.10). Again, a cascaded controller design consisting of a current controller, a superposed speed and a position controller is implemented and again, except for the position controller, proportional-integral (PI) controllers including Anti-Windup [47] strategies are used. Moreover, again, the control paths for the d and q-axis are treated separately.
The main properties of the SynRM's controller are listed below.

- No flux controller is required.
- The position controller is implemented in exactly the same way as for the induction machine.
- The control paths of the current controller in d and q-axis differ from each other, because of the different inductances (see Section 3.3.1).
- The speed controller uses the MTPA (maximum torque per ampere) control strategy (see Section 3.3.1) including field weakening.

3.3.1 Current Controller

The control paths of the current controller, resulting from eqs. (3.5) and (3.6), are given by

$$u_\mathrm{d}(t) = R_\mathrm{S}\, i_\mathrm{d}(t) + L_\mathrm{d}\frac{d}{dt} i_\mathrm{d}(t) \underbrace{-\omega_\mathrm{R}\, L_\mathrm{q}\, i_\mathrm{q}(t)}_{u_\mathrm{d,\,comp}} \quad \text{and} \tag{3.34}$$

$$u_\mathrm{q}(t) = R_\mathrm{S}\, i_\mathrm{q}(t) + L_\mathrm{q}\frac{d}{dt} i_\mathrm{q}(t) \underbrace{+\omega_\mathrm{R}\, L_\mathrm{d}\, i_\mathrm{d}(t)}_{u_\mathrm{q,\,comp}} \quad . \tag{3.35}$$

Subtracting the compensation voltages $u_\mathrm{d,\,comp}$ and $u_\mathrm{q,\,comp}$ from eqs. (3.34) and (3.35) gives a linear control paths,

$$u_\mathrm{d}(s) = R_\mathrm{S}\, i_\mathrm{d}(s) + L_\mathrm{d}\, s\, i_\mathrm{d}(s) \quad \text{and} \quad u_\mathrm{q}(s) = R_\mathrm{S}\, i_\mathrm{q}(s) + L_\mathrm{q}\, s\, i_\mathrm{q}(s) \quad , \tag{3.36}$$

similar to those of the induction machine, c.f. eq. (2.20). The tuning parameters of the controller were determined in exactly the same way as for the induction machine.

3.3.2 Speed Controller - MTPA

In the basic setting range of the SynRM the maximum torque per ampere strategy (MTPA) i.e., $i_\mathrm{d} = i_\mathrm{q}$, minimises copper losses for an unsaturated machine [59] and is implemented in the controller. For a saturated machine, the angle between i_d and i_q becomes larger than 45 °, however requiring additional knowledge concerning torque as a function of current, which is not available, due to the absence of a torque-sensing flange. For this reason, this characteristic of the SynRM is not considered within the controller design. Other possibilities to implement a controller for the SynRM are e.g., discussed in [60].

Since the maximum current $I_\mathrm{S,\,max}$ and voltage $U_\mathrm{S,\,max}$ are determined by the power converter of the application the conditions,

$$I_\mathrm{S,\,max} \geq \sqrt{{i_\mathrm{d}^*}^2 + {i_\mathrm{q}^*}^2} \quad \text{and} \quad U_\mathrm{S,\,max} \geq \sqrt{{u_\mathrm{d}^*}^2 + {u_\mathrm{q}^*}^2} \quad ,$$

have to be considered in the controller design as well[4].

[4] Command variables are marked with a $*$ superscript.

To also ensure a maximum torque control in the field weakening region, needed in the periods of abrupt position change within the cycle, a strategy proposed in [61] is implemented. Within those short phases of the cycle, the machine reaches a high speed, which requires field weakening control, due to the limited voltage.

This method expresses the q-axis current in terms of i_d,

$$i_\mathrm{q} \;=\; a\, i_\mathrm{d} \qquad a \in \mathbb{R} \quad , \tag{3.37}$$

and establishes a relation between the torque, the d-q-model equations and $U_{\mathrm{S,\,max}}$. This results in an optimisation problem and its solution, derived below, gives a maximum torque per voltage (MTPV) control strategy for the SynRM, which is also implemented in the controller design.

The d-q-model equations simplify for steady state, $\dot{\Psi}_\mathrm{d} \;=\; \dot{\Psi}_\mathrm{q} \;=\; 0$, to

$$u_\mathrm{d} \;=\; R_\mathrm{S}\, i_\mathrm{d} - \omega_\mathrm{R}\, L_\mathrm{q}\, i_\mathrm{q} \quad \text{and} \quad u_\mathrm{q} \;=\; R_\mathrm{S}\, i_\mathrm{q} + \omega_\mathrm{R}\, L_\mathrm{d}\, i_\mathrm{d} \quad . \tag{3.38}$$

Combining eqs. (3.37) and (3.38) and the condition for the maximum voltage $U_{\mathrm{S,\,max}}$ results in:

$$\begin{aligned} U_{\mathrm{S,\,max}}^2 \;\geq\; u_\mathrm{d}^2 + u_\mathrm{q}^2 \;&=\; (R_\mathrm{S}\, i_\mathrm{d} - \omega_\mathrm{R}\, L_\mathrm{q}\, i_\mathrm{q})^2 + (R_\mathrm{S}\, i_\mathrm{q} + \omega_\mathrm{R}\, L_\mathrm{d}\, i_\mathrm{d})^2 \\ &=\; (R_\mathrm{S}\, i_\mathrm{d} - \omega_\mathrm{R}\, L_\mathrm{q}\, a\, i_\mathrm{d})^2 + (R_\mathrm{S}\, a\, i_\mathrm{d} + \omega_\mathrm{R}\, L_\mathrm{d}\, i_\mathrm{d})^2 \\ i_\mathrm{d}^2 \;&=\; \frac{U_{\mathrm{S,\,max}}^2}{(R_\mathrm{S} - \omega_\mathrm{R}\, L_\mathrm{q}\, a)^2 + (R_\mathrm{S}\, a + \omega_\mathrm{R}\, L_\mathrm{d})^2} \end{aligned} \tag{3.39}$$

Inserting eqs. (3.37) and (3.39) into the expression for the torque, eq. (3.12), gives

$$\begin{aligned} T_\mathrm{motor} \;&=\; \frac{3}{2}\, p\, (L_\mathrm{d} - L_\mathrm{q})\, i_\mathrm{d}\, i_\mathrm{q} \;=\; \frac{3}{2}\, p\, (L_\mathrm{d} - L_\mathrm{q})\, a\, i_\mathrm{d}^2 \\ &=\; \frac{3}{2}\, p\, (L_\mathrm{d} - L_\mathrm{q})\, a\, \frac{U_{\mathrm{S,\,max}}^2}{(R_\mathrm{S} - \omega_\mathrm{R}\, L_\mathrm{q}\, a)^2 + (R_\mathrm{S}\, a + \omega_\mathrm{R}\, L_\mathrm{d})^2} \quad , \end{aligned} \tag{3.40}$$

and establishes a relation between the torque of the machine and the maximum voltage of the power converter.

Assuming L_d and L_q constant for any given point of operation, the solution of the optimisation problem

$$\frac{d}{da}\, T_\mathrm{motor} \;=\; \frac{d}{da} \left(\frac{3}{2}\, p\, (L_\mathrm{d} - L_\mathrm{q})\, a\, \frac{U_{\mathrm{S,\,max}}^2}{(R_\mathrm{S} - \omega_\mathrm{R}\, L_\mathrm{q}\, a)^2 + (R_\mathrm{S}\, a + \omega_\mathrm{R}\, L_\mathrm{d})^2} \right) \;\stackrel{!}{=}\; 0$$

yield the equations for maximum torque control in the field weakening region, eqs. (3.41) to (3.43), as also shown in [61].

$$a \;=\; \sqrt{\frac{R_\mathrm{S}^2 + \omega_\mathrm{R}^2\, L_\mathrm{d}^2}{R_\mathrm{S}^2 + \omega_\mathrm{R}^2\, L_\mathrm{q}^2}} \tag{3.41}$$

$$i_\mathrm{d}^* \;= U_{\mathrm{S,\,max}} \sqrt{\frac{1}{(R_\mathrm{S} - \omega_\mathrm{R}\, L_\mathrm{q}\, a)^2 + (R_\mathrm{S}\, a + \omega_\mathrm{R}\, L_\mathrm{d})^2}} \tag{3.42}$$

$$i_\mathrm{q}^* \;= U_{\mathrm{S,\,max}} \sqrt{\frac{1}{(R_\mathrm{S}/a - \omega_\mathrm{R}\, L_\mathrm{q})^2 + (R_\mathrm{S} + \omega_\mathrm{R}\, L_\mathrm{d}/a)^2}} \tag{3.43}$$

Since the magnetising inductances of the SynRM are affected by saturation [62], it is recommendable to consider these non-linearities in the controller design as well. A possible approach is to perform beforehand simple standstill (locked rotor) DC tests [63] to identify L_d and L_q as a function of i_d and i_q and to use the results in lookup tables within the controller (see Fig. 5.13a and [61]). A schematic illustration of the implemented speed controller is shown in Fig. 3.7, the details of the underlying FOC are not shown, due to reasons of confidentiality.

The tuning parameters of the proportional-integral speed controller are determined with the method of Ziegler and Nichols [49] (see Section 2.3.1).

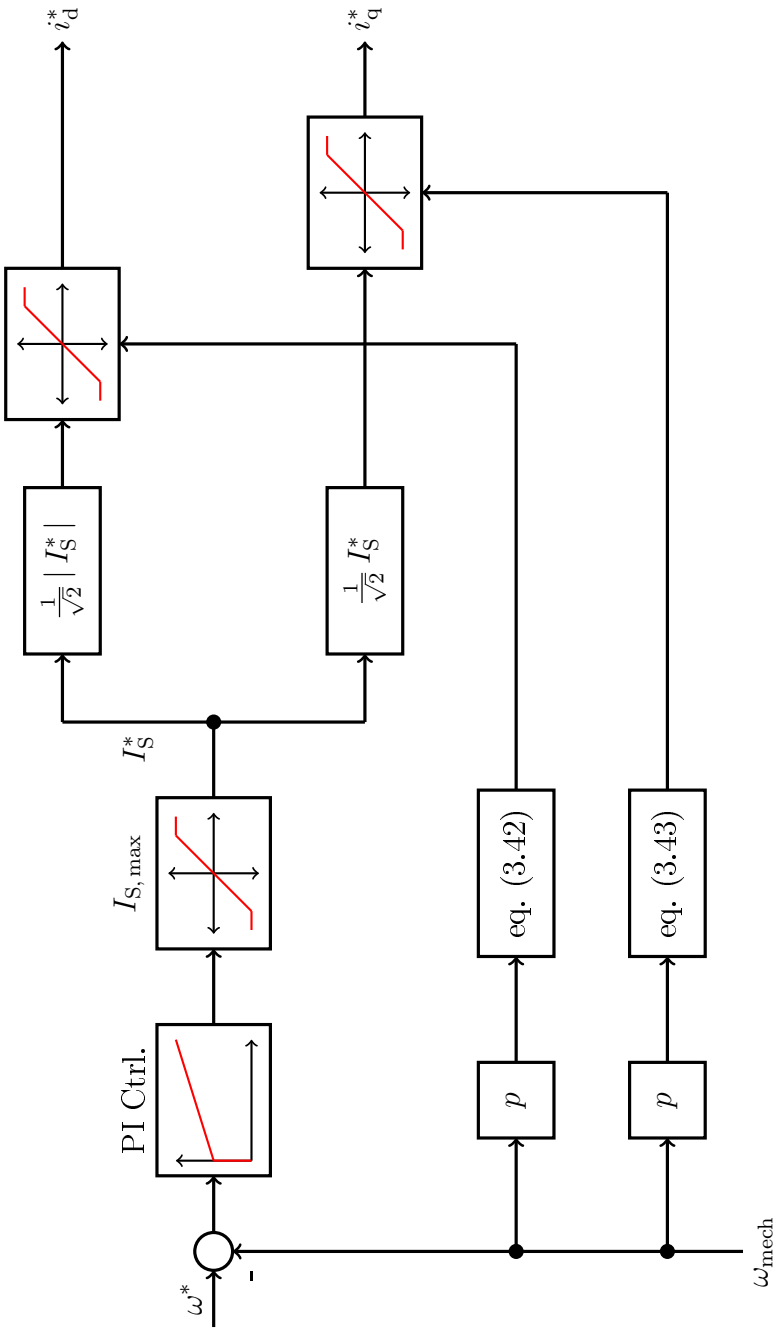

Figure 3.7: Schematic illustration of the speed controller for the SynRM, further details are presented in [61]. The cascaded control structure is similar to Fig. 2.10 and, again, the details of the underlying FOC are not shown, due to reasons of confidentiality. The command variables are marked with a $*$ superscript, $I_{\mathrm{S,\,max}}$ denotes the maximum value of current of the power converter and ω_mech is obtained from a rotary encoder.

3.4 Cross Saturation

The saturation of the iron-sheets in synchronous reluctance motors causes a magnetic coupling between d- and q-axis [62, 63]. This means the magnetic flux in d-axis does not only depend on i_d but also on i_q and vice versa and should be taken into account.

Simple analytic models based on a sinusoidally distributed magnetomotive force and a reluctance network for the rotor, such as the one presented in Section 3.2, allow to compute the magnetising inductances of the machine in one point of operation. But, d- and q-axis are treated separately and independently from each other and the influence of slotting and saturation is neglected.

More sophisticated (semi) analytic methods based on winding functions e.g. [64], considering the effect of slotting, are able to give an accurate estimation of the flux density in the air gap if the core is not saturated.

Computations based on finite element analysis (FEA) are, in general, able to consider the nonlinearity of the iron sheet and therefore different saturation states of the machine. But FEA are more computationally intensive than (semi) analytic methods. Especially the simulation of a transient operation and when the finite element solver is coupled to another simulation, which needs small time steps, causes long computing times.

Another approach, which is able to consider cross saturation and to perform transient simulations within reasonable computational time is presented in the following. This model is used for the comparison with the measurement results (see Section 5.3.3).

This method is based on the d-q-model equations,

$$\dot{\Psi}_\mathrm{d} \;=\; u_\mathrm{d} - i_\mathrm{d}\left(\Psi_\mathrm{d},\,\Psi_\mathrm{q}\right) R_\mathrm{S} + \omega_\mathrm{R}\,\Psi_\mathrm{q} \quad \text{and} \quad \dot{\Psi}_\mathrm{q} \;=\; u_\mathrm{q} - i_\mathrm{q}\left(\Psi_\mathrm{d},\,\Psi_\mathrm{q}\right) R_\mathrm{S} - \omega_\mathrm{R}\,\Psi_\mathrm{d} \quad , \tag{3.44}$$

and uses results of steady-state finite element computations to consider the mutual dependences of the d- and q-axis, provided in two-dimensional lookup tables within the simulation.

The procedure to obtain the data for the lookup table is described below and schematically shown in Fig. 3.8.

1. The geometry of the machine and specific values for the stator current space phasor $\hat{I}_\mathrm{S}$ and its angle β (to determine i_d and i_q) are needed as an input to compute the flux density distribution of the machine via FEA.

2. The radial component of the flux density in the mid of the air gap as a function of the azimuthal angle $B_\delta\left(\varphi\right)$ is extracted. The component of the fundamental wave $\hat{B}_{\delta 1}$ and its maximum's azimuthal position γ is computed using the fourier transformation.

3. Eq. (3.15),
$$\Psi_\mathrm{h} \;=\; \frac{2}{\pi}\,\tau_\mathrm{p}\,l_\mathrm{Fe}\,w_\mathrm{str}\,\xi\hat{B}_{\delta 1} \quad ,$$
gives the main flux linkage Ψ_h and further Ψ_d and Ψ_q, c.f. Fig. 3.2.

4. A two-dimensional linear interpolation provides i_d and i_q as a function of Ψ_d and Ψ_q for use in the lookup table (red terms in eq. (3.44)).

The complete procedure is repeated for various rotor positions to average out the influence of the slotting. The two-dimensional lookup tables itself are shown in Fig. B.2.

Since harmonics of the flux density in the air gap and their influence on the torque of the machine are not considered in this approach, a correction value,

$$f_{\text{torque}}\left(\hat{I}_{\text{S}}\right) = \frac{T_{\text{motor, dq}}\left(\hat{I}_{\text{S}},\ \beta = 45\,^{\circ}\right)}{T_{\text{motor, FEA}}\left(\hat{I}_{\text{S}},\ \beta = 45\,^{\circ}\right)} \quad , \tag{3.45}$$

is introduced to compensate this difference, at least on the average, within the simulation.

Fig. 3.9 shows a comparison of steady-state torque characteristic between a finite element analysis and the described d-q-model. The factor defined in eq. (3.45) ensures that these curves match each other, at least for $i_{\text{d}} = i_{\text{q}}$.

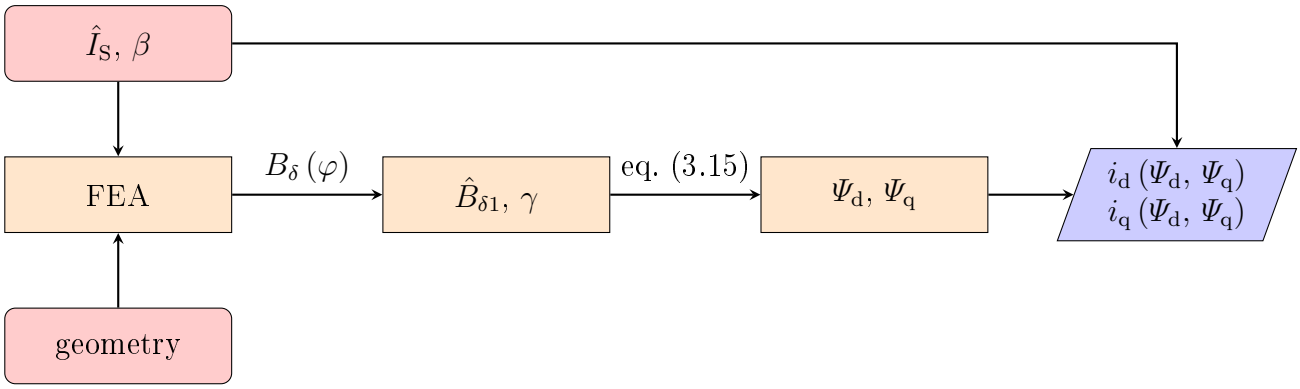

Figure 3.8: Schematic illustration to obtain the two-dimensional lookup tables to simulate d-q-model eqs. (3.44). The results are shown in Fig. B.2.

The advantage of this approach is evident, the time-consuming finite element computation has to be performed only once beforehand. Afterwards, arbitrary scenarios can be simulated requiring a fraction of computational time and providing nearly the same degree of accuracy: as illustrated for example in Fig. 3.10.

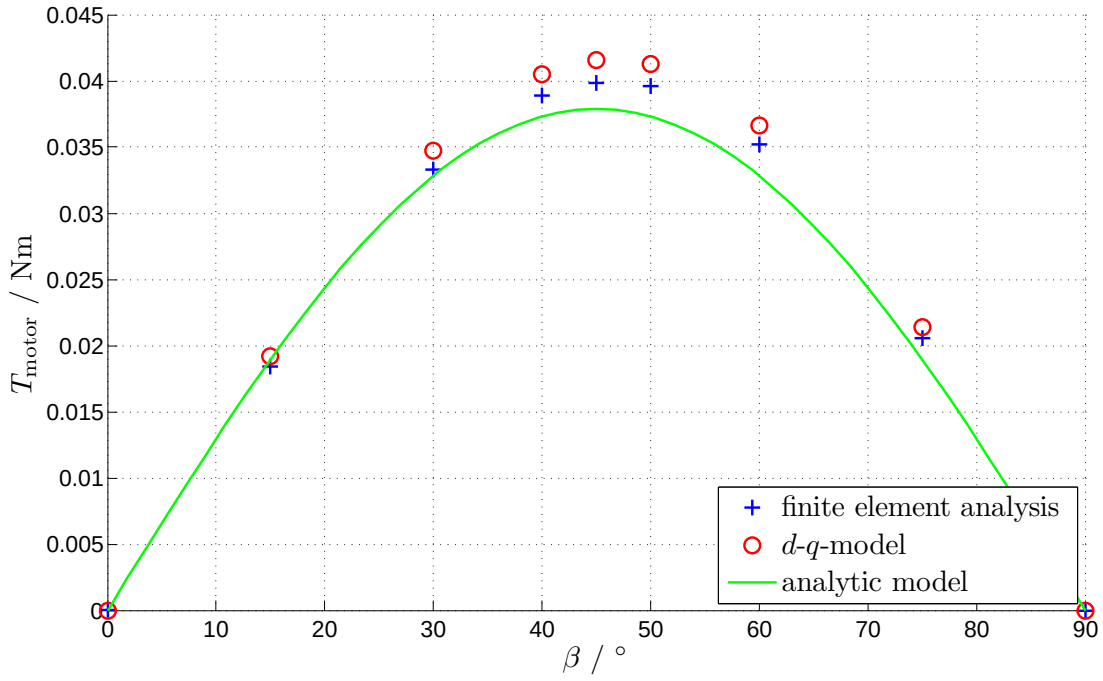

Figure 3.9: Steady state torque characteristic for a stator current of $\hat{I}_{\mathrm{S}} = 5.1\,\mathrm{A}$ (which results in a slightly saturated machine, c.f. Fig. B.1) and a geometry according to Fig. 4.5. The factor in eq. (3.45) was introduced to compensate the difference between the results of the finite element analysis (blue +) and the d-q-model (red ∘). The green line shows the result of the analytic model, presented in Section 3.2.

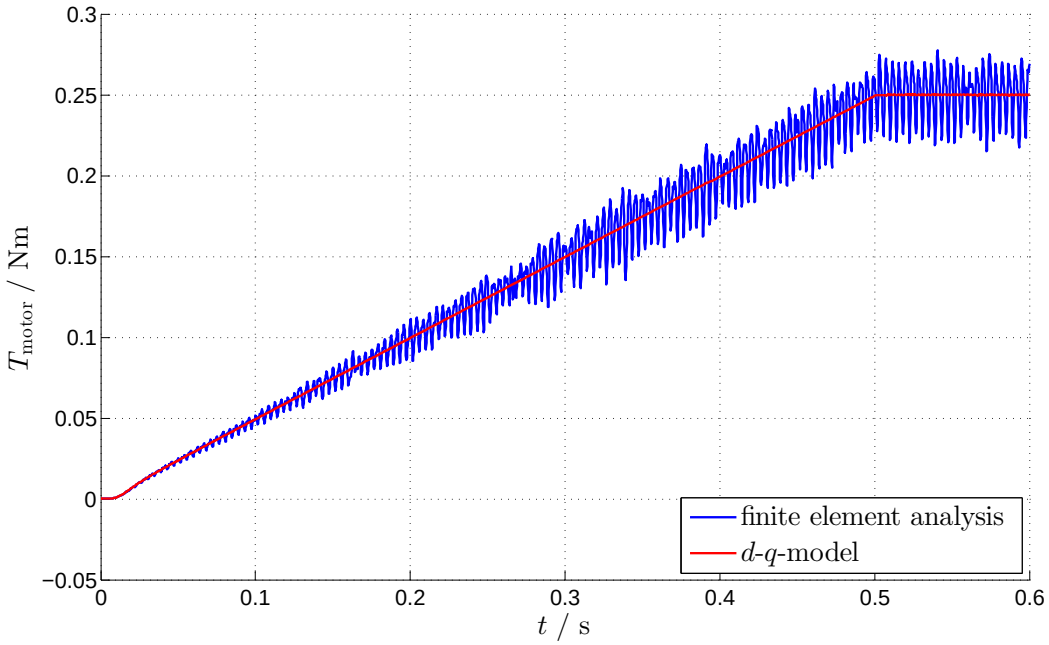

(a) Torque T_{motor} as a function of time t.

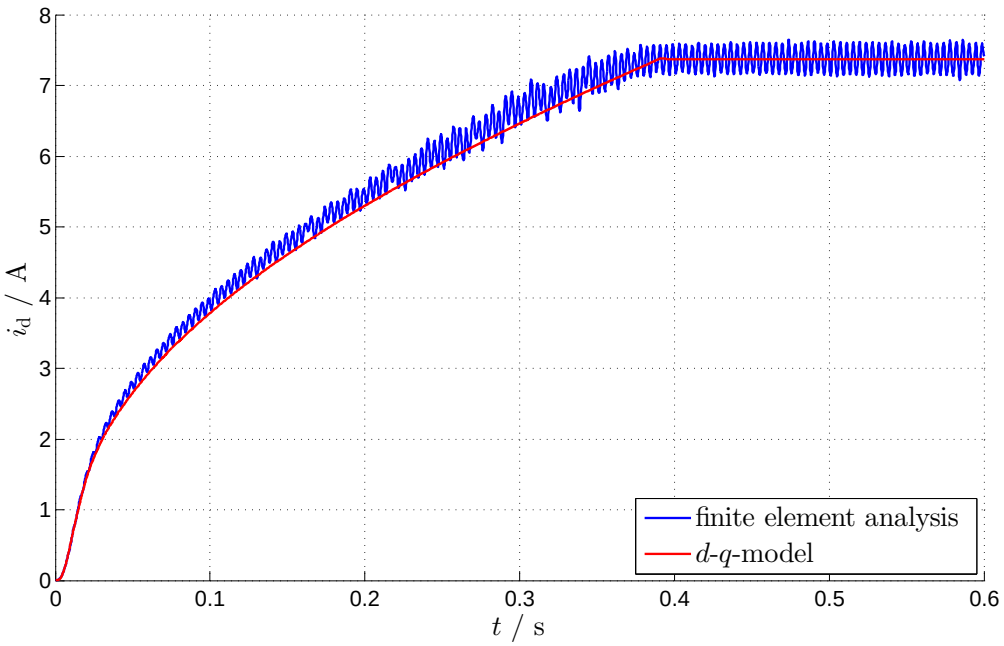

(b) d-axis current i_{d} as a function of time t.

Figure 3.10: Comparison of the presented d-q-model including the torque factor of eq. (3.45) and a finite element analysis, computed using JMAG® [36]. The graphs show a simulated torque ramp in the field weakening region for constant speed.

Chapter 4

Optimal Designs

This chapter describes an optimal machine design for the IM respectively the SynRM regarding an arbitrarily criterion, such as maximum torque in a specific operating point, or in particular for this application to run through the defined cycle producing a minimum of copper loss.

Therefore, on the one hand, similar to Chapter 2.1.2, some input parameters for the optimisation have to be defined, which completely describe the mechanical and electrical properties of the machine. The number of input parameters should be chosen according to the rule "as much as necessary but as little as possible" to keep the space of the optimisation small and further the computing time as short as possible. On the other hand, also the constraints given by the application, listed in Tables 1.1 and 1.2 have to be considered.

The outer dimension of the machine were fixed to

$$l_{\mathrm{Fe}} = 60\,\mathrm{mm} \quad \text{and} \quad d_{\mathrm{SO}} = 40\,\mathrm{mm} \quad ,$$

as a suitable compromise between the volume and the permitted losses (see Section 2.1.2) to fulfil a steady-state and a transient condition, defined in eqs. (2.1) and (2.2), which are derived from the original cycle, shown in Fig. 1.2.

This high-dimensional and non-linear problem is solved using a Genetic Algorithm (GA) included in the *Global Optimization Toolbox* of the commercial software *MATLAB*® [65]. This kind of solver enables to find the global optimum, or at least a very good local one, for this type of problem [66].

The main part within a GA is provided by the fitness function, schematically shown in Fig. 4.1. It uses geometry parameters as input, computes the properties of the resulting machine and evaluates this machine with a fitness value concerning a defined criterion. The formulation of this optimisation criterion is a very important detail of the computation.

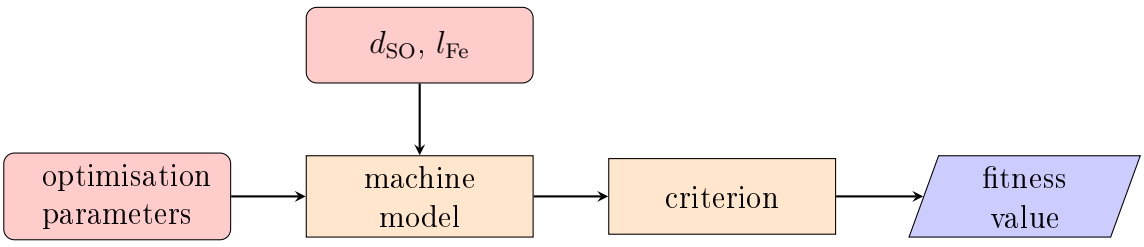

Figure 4.1: Schematic diagram of the fitness function integrated into the genetic algorithm to obtain a minimum loss machine design.

4.1 Optimisation of the IM

For the optimisation of the induction machine **9 parameters**, listed below, are used to define its mechanical (e.g. torque of inertia of the rotor) and electrical (e.g. equivalent circuit parameters) properties. The slot geometry for the computation of stator and rotor is defined in Figs. 2.3 and 4.2. Further constraints and assumptions are listed in Table 4.1.

1. Number of pole pairs p.
2. Number of slots per pole q
   p and q define the number of stator slots
   $$N_{\mathrm{S}} = 6\,p\,q \quad .$$
3. Ratio of air-gap diameter d_δ and outer diameter d_{SO}
   Thereby d_δ, the height of the stator (h_{SJ}+h_{ST}) and the height of the rotor (h_{RJ}+d_{bar}+h_{bar}) are determined.
4. Ratio of slot-tooth layer h_{ST} of the stator and height of the stator ($h_{\mathrm{ST}} + h_{\mathrm{SJ}}$).
5. Ratio of stators tooth-width a_{S} and slot pitch τ_{SSP} .
6. Ratio of the slot opening width a_{SSO} and the slot width ($\tau_{\mathrm{SSP}} - a_{\mathrm{S}}$) of the stator
   In combination with Fig. 4.2 point 4, 5 and 6 determine the complete geometry of the slot-tooth layer of the stator.
7. Number of rotor bars N_{bar},
   N_{bar} defines the slot-pitch
   $$\tau_{\mathrm{RSP}} = \frac{(d_\delta - \delta)\,\pi}{N_{\mathrm{bar}}} \quad .$$
8. Ratio of rotor tooth width a_{R} and slot pitch τ_{RSP}.
   The diameter of the rotor bars results in
   $$d_{\mathrm{bar}} = \tau_{\mathrm{RSP}} - a_{\mathrm{R}} \quad .$$
   Thereby, also the complete geometry of the slot-tooth layer of the rotor is fixed.
9. Magnetic flux density in the air gap $\hat{B}_\delta$ for nominal voltage and frequency.
   Thus, also the nominal magnetic flux Φ_{p} of the machine is determined and further the number of turns in series w_{str} per phase of the machine.

The machine is designed under consideration of all these constraints regarding a certain criterion, which is defined in Section 4.1.1.

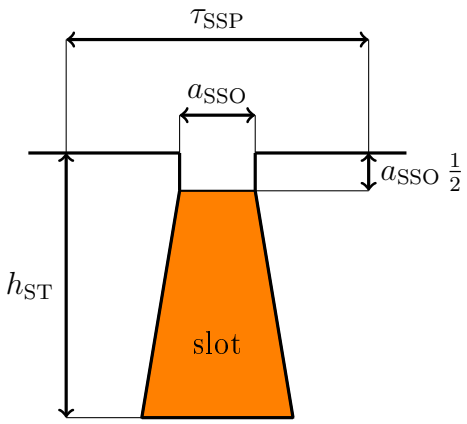

Figure 4.2: Sketch of the defined stator slot. Parallel teeth are assumed. The orange area illustrates the space for the winding.

Table 4.1: Additional assumptions and constraints.

Description	Symbol	Value	Unit
Nominal voltage (effective value)	U_{S}	2	V
Nominal frequency	f_{S}	$50\,p$	Hz
Slot fill factor	k_{sff}	0.5	-
Air gap length	δ	0.2	mm
Virtual slot opening width of rotor	a_{RSO}	$3\,\delta$	mm
Distance between the outer diameter of rotor and the rotor bar	h_{bar}	0.1	mm
Relative permeability in the flux bridge of rotor	μ_{r}	10	-
Width of the short-circuit ring[1]	a_{SCR}	5.0	mm
Length of winding overhang	-	10	mm

[1] The height of the short-circuit ring is equal to the rotor height.

4.1.1 Optimisation Criterion

A custom-designed optimisation criterion is needed, which represents the quality of a machine design in a single value. Amongst others, for this application two different criteria, entailing advantages and disadvantages, were used.

1. A machine specific characteristic
   The equivalent circuit parameters are used to compute a steady-state characteristic of the machine at nominal voltage and frequency. An empirically found criterion, according to

$$\int_0^1 \frac{T_{\text{motor}}(s)}{P_{\text{Cu, Stator}}(s)}\, ds \quad ,$$

   has been proven to be useful for this application. That means the machine, which generates most torque per losses, integrated over the entire torque slip curve, obtains the best fitness value.

   The advantage of this criterion is that it needs relatively little computation time. On the other hand, it is not possible to predict the losses to run through the complete cycle within the optimisation algorithm. This has to be performed after the GA has converged.

2. The complete cycle
   A more straightforward approach is to simulate the complete cycle and to use the computed losses as fitness value. Since simulating the complete cycle including the flux optimisation approach (Section 2.3.2) is time-consuming, machine designs, which do not fulfil eq. (2.2) are rejected beforehand.

In the context of this work, the optimisation was performed using both types for calculating the fitness value with comparable results.

4.1.2 Final Machine Design

Within an outer diameter of 40 mm and an active length of 60 mm, the minimum loss design of the GA yields the set of parameters listed in Table 4.2. These parameters determine the electrical and mechanical properties of the machine, listed in Table 4.3. The cross section of the machine is shown in Fig. 4.3 and the computed steady-state characteristics of the machine are presented in the Figs. 2.7 to 2.9.

The mean copper losses to run through the cycle of the optimal machine design, considering the specifications of Section 1.2 and the parameters of Table 2.2, yields

$$\overline{P}_{\text{Cu}} \approx \frac{1}{12}\int_0^{12} \frac{3}{2}\left[R_{\text{S}}\left(i_{\text{Sd}}^2(t)+i_{\text{Sq}}^2(t)\right)+R_{\text{R}}\, i_{\text{Sq}}^2(t)\right] dt \approx 19.5\,\text{W} \quad . \tag{4.1}$$

Table 4.2: Result of the GA to obtain a minimum loss design for a machine with an outer diameter d_{SO} of 40 mm and an active length l_{Fe} of 60 mm.

Parameters	p	q	$\frac{d_\delta}{d_{\text{SO}}}$	$\frac{h_{\text{ST}}}{h_{\text{SJ}}+h_{\text{ST}}}$	$\frac{a_{\text{S}}}{\tau_{\text{SSP}}}$	$\frac{a_{\text{SSO}}}{\tau_{\text{SSP}}-a_{\text{S}}}$	N_{bar}	$\frac{a_{\text{R}}}{\tau_{\text{RSP}}}$	$\hat{B}_\delta$
Value	1	3	0.54	0.66	0.36	0.35	32	0.71	0.21 T

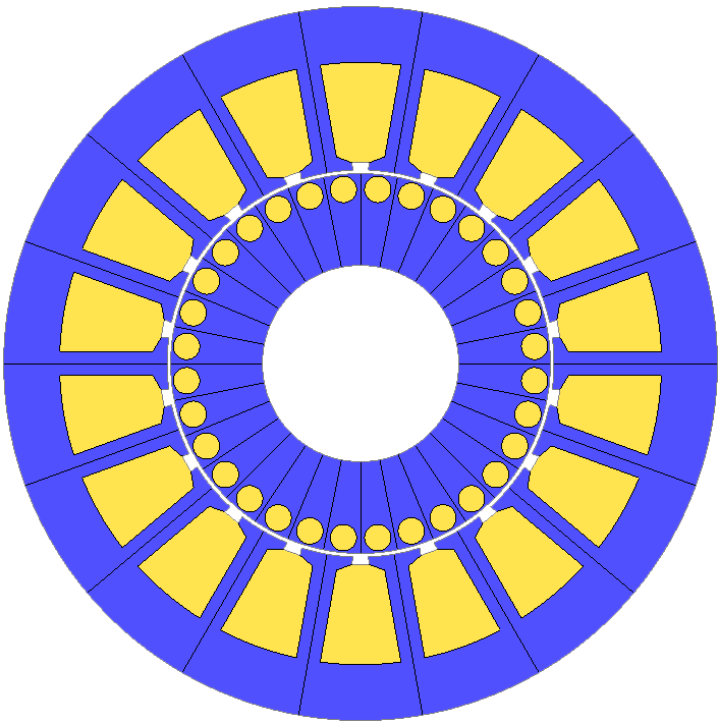

Figure 4.3: Cross section of the induction machine's final design, visualised using JMAG® [36].

Table 4.3: Further information on the minimal loss machine design shown in Table 4.2. The electrical parameters are computed for a temperature of 100 °C and are fitted to a finite element computation, c.f. Section 2.2.1.3.

Description	Symbol	Value	Unit
Stator outer diameter	d_{SO}	40.00	mm
Stator bore diameter	d_{SI}	21.68	mm
Height of stators slot-tooth layer	h_{ST}	6.03	mm
Height of stator yoke	h_{SJ}	3.13	mm
Tooth width stator	a_{S}	1.35	mm
Slot opening width of the stator	a_{SSO}	0.86	mm
Cross-sectional area of one stator slot	-	19.35	mm^2
Number of turns in series per phase	w_{str}	27	-
Rotor outer diameter	d_{RO}	21.28	mm
Rotor bar diameter	d_{bar}	1.48	mm
Rotor's mass moment of inertia	I	$1.08 \cdot 10^{-5}$	kgm^2
Stator ohmic resistance	R_{S}	0.14	Ω
Rotor ohmic resistance	R_{R}	0.24	Ω
Stator leakage inductance	$L_{\mathrm{S}\sigma}$	0.13	mH
Rotor leakage inductance	$L_{\mathrm{R}\sigma}$	0.20	mH
Main inductance at nominal voltage and frequency	L_{h}	1.45	mH
Optimal nominal value of rotor flux	$\Psi_{\mathrm{R\,opt}}$	$9.5 \cdot 10^{-3}$	Vs

4.2 Optimisation of the SynRM

Similar to the IM (see Section 4.1), also for the SynRM, the previously presented analytic model (Section 3.2) is used within a GA to obtain an optimal machine design for this application.

Again, some input parameters for the optimisation have to be defined, which completely describe the machine, but they differ slightly to those of the induction motor. Also, the optimisation criterion determining the fitness value, presented in Section 4.2.1, which evaluates the quality of a machine design in a single value has to be adjusted to the current issue.

For an adequate comparison between the IM and the SynRM, both machine types have to be optimised relating to the same constraints. In particular, the outer dimensions of the machine are fixed to

$$l_{\mathrm{Fe}} = 60\,\mathrm{mm} \quad \text{and} \quad d_{\mathrm{SO}} = 40\,\mathrm{mm} \quad .$$

For the computation of the optimal machine design of the SynRM **7 parameters**, listed below, are used as an input to determine mechanical and electrical properties.

1. Number of pole pairs p.
2. Number of slots per pole q.
3. Ratio of air-gap diameter d_δ and outer diameter d_{SO}.
4. Ratio of slot-tooth layer h_{ST} of the stator and height of the stator $(h_{\mathrm{ST}} + h_{\mathrm{SJ}})$.
5. Ratio of stators tooth-width a_{S} and slot pitch τ_{SSP} .
6. Number of flux barriers in the rotor cross section $N_{barrier}$.
7. Ratio of flux barrier width w_{barrier} to flux path width w_{path}.[2]

In contrast to the optimisation of the IM, two parameters, $\hat{B}_\delta$[3] and a_{SSO}[4], are determined with an educated guess: Both are of secondary importance in the analytic model.

Table 4.4: Additional assumptions and constraints for the minimum loss design of the SynRM. Geometry parameters are defined in Fig. 4.4.

Description	Symbol	Value	Unit
Nominal voltage (effective value)	U_{S}	2	V
Nominal frequency	f_{S}	$20\,p$	Hz
Slot fill factor	k_{sff}	0.5	-
Air gap length	δ	0.2	mm
Length of winding overhang	-	10	mm
Relative permeability of the iron sheets[5]	μ_{r}	310	-
Relative permeability in the flux bridge of the rotor[6]	$\mu_{\mathrm{r,\,bridge}}$	5	-
Width of the flux bridge of the rotor	w_{bridge}	0.25	mm

[2] w_{barrier} and w_{path} are defined in Fig. 4.4.
[3] The magnetic flux density in the air gap, determined with $\hat{B}_\delta = 0.3\,\mathrm{T}$, for $\hat{I}_{\mathrm{S}} = \hat{I}_{\mathrm{d}}$.
[4] The slot opening width of the stator a_{SSO} affects only the carter factor and is set to half of the slot width.
[5] Needed for the computation of L_{d}.
[6] Needed for the computation of L_{q}.

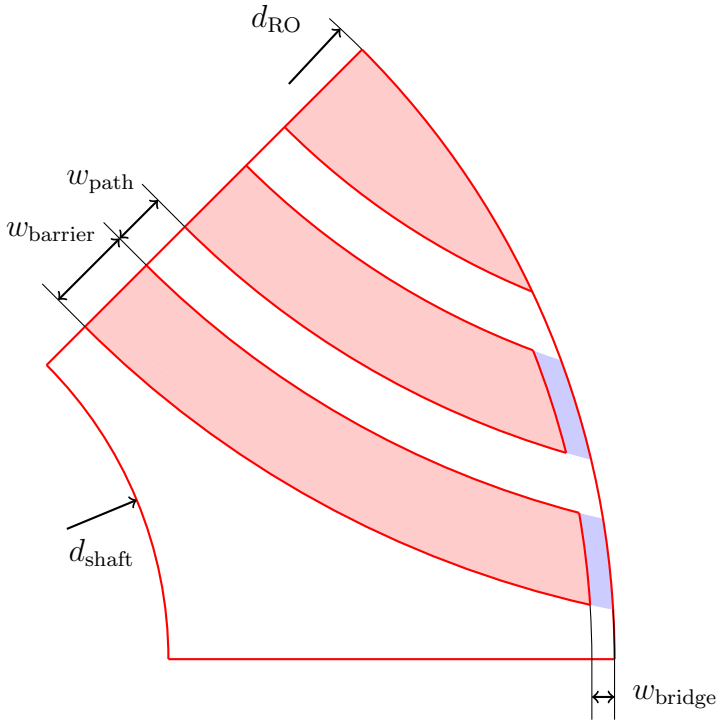

Figure 4.4: Sketch of half a pole of the rotor cross section. The areas marked in red indicate the flux barriers (material with $\mu_{\mathrm{r}} = 1$), the flux bridges are highlighted in blue.

4.2.1 Optimisation Criterion

For this application two different fitness values have been shown to provide the desired results.

1. Maximum torque per copper loss
   A fitness value according to

$$\frac{T_{\mathrm{motor}}}{P_{\mathrm{Cu}}} \propto \frac{p\,(L_{\mathrm{d}} - L_{\mathrm{q}})\,I_{\mathrm{d}}\,I_{\mathrm{q}}}{R_{\mathrm{S}}\,\left(I_{\mathrm{d}}^2 + I_{\mathrm{q}}^2\right)} \overset{I_{\mathrm{d}}=I_{\mathrm{q}}}{\propto} \frac{p\,(L_{\mathrm{d}} - L_{\mathrm{q}})}{R_{\mathrm{S}}} \quad ,$$

   does only depend on the geometrical parameters of the machine. Certainly machine designs, which do not fulfill conditions determined by the cycle, such as the required acceleration assuming a temporarily overload, are rejected.

2. The complete cycle
   Again, the straightforward approach is to simulate the complete cycle and to use the computed losses as fitness value. But also for the SynRM simulating the complete cycle needs a lot of computational time.

   For this reason, it is also suitable to reject machine designs which do not fulfil eq. (2.2) beforehand.

4.2.2 Final Machine Design

The optimisation results in the set of parameters listed in Table 4.5. These parameters determine the cross section, shown in Figure 4.5, the electrical and mechanical properties of the machine, listed in Table 4.6.

The mean copper looses to run through the cycle of the optimal machine design, using the two-dimensional lookup tables for the d-q-model (eqs. (3.44)) of Fig. B.2, the dependencies of the magnetising inductances L_d and L_q of Fig. B.1 for the speed controller and considering the specifications of Section 1.2, yields

$$\overline{P}_\mathrm{Cu} \;=\; \frac{1}{12}\int_0^{12} \frac{3}{2}\, R_\mathrm{S}\, i_\mathrm{S}^2\,(t)\, dt \;\approx\; 13.5\,\mathrm{W} \quad . \tag{4.2}$$

Table 4.5: Result of the GA to obtain a minimum loss design, for a machine with an outer diameter d_SO of 40 mm and an active length l_Fe of 60 mm.

Parameters	p	q	$\frac{d_\delta}{d_\mathrm{SO}}$	$\frac{h_\mathrm{ST}}{h_\mathrm{SJ}+h_\mathrm{ST}}$	$\frac{a_\mathrm{S}}{\tau_\mathrm{SSP}}$	N_barrier	$\frac{w_\mathrm{barrier}}{w_\mathrm{path}}$
Value	2	2	0.57	0.75	0.45	2	1.43

Table 4.6: Further information concerning the minimal loss machine design according to Table 4.5. The electrical parameters are computed for a temperature of 100 °C.

Description	Symbol	Value	Unit
Stator outer diameter	d_SO	40.00	mm
Stator bore diameter	d_SI	23.16	mm
Height of stators slot-tooth layer	h_ST	6.28	mm
Height of stator yoke	h_SJ	2.14	mm
Tooth width stator	a_S	1.36	mm
Cross-sectional area of one stator slot	-	14.64	mm^2
Number of turns in series per phase	w_str	44	-
Outer diameter of rotor	d_RO	22.76	mm
Rotor's mass moment of inertia	I	$6.23 \cdot 10^{-6}$	kgm^2
Stator winding ohmic resistance	R_S	0.30	Ω
Stator current at nominal operating point	I_S	3.60	A
Flux density in the air gap, d-axis *	$\hat{B}_{\delta 1,\mathrm{d}}$	0.29	T
Flux density in the air gap, q-axis *	$\hat{B}_{\delta 1,\mathrm{q}}$	0.12	T
Magnetising inductance for d-axis *	L_d	1.70	mH
Magnetising inductance for q-axis *	L_q	0.68	mH

* for nominal point of operation

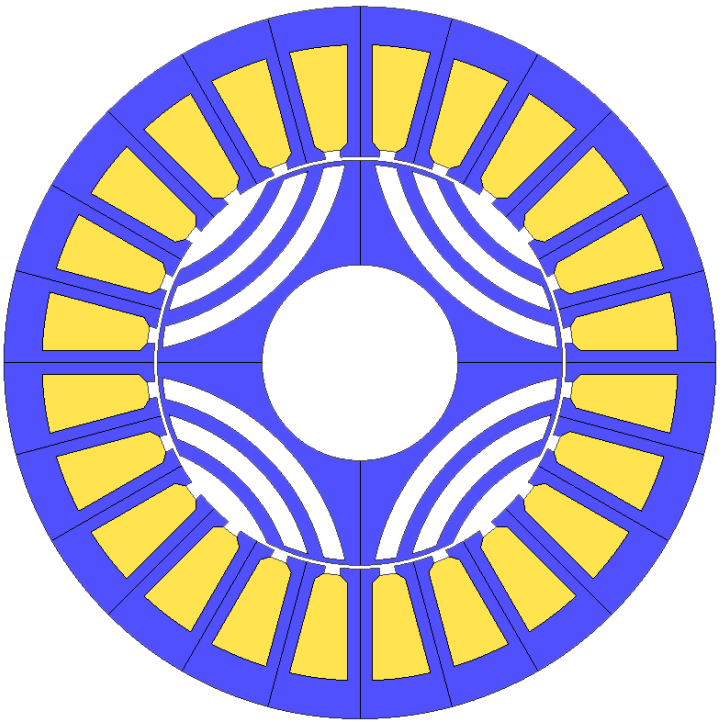

Figure 4.5: Cross section of the synchronous reluctance machine's final design, visualised using JMAG® [36].

Chapter 5

Measurement Results

5.1 Friction in a Thread

Section 1.2.2 gives an overview of the mechanical system, which is used as a basis for the machine design. Measurement results, which are in poor agreement with the original approximation for the mechanic, demand a more detailed consideration.

The modeling of the spindle, which transforms the circular motion of the motor into a linear motion, can be reduced to an inclined plane [67, Chapter 5].

For the movement against the force of the spring, considering Fig. 5.1 and eqs. (5.5) to (5.8), the balance of forces is given by,

$$F_{\text{motor}} \cos\alpha \;=\; F_{\text{t, load}} + \mu\, F_{\text{n}} \;=\; F_{\text{load}} \sin\alpha + \mu\, (F_{\text{load}} \cos\alpha + F_{\text{motor}} \sin\alpha) \quad . \tag{5.1}$$

Using the well know relation,

$$\tan(x \pm y) \;=\; \frac{\tan x \pm \tan y}{1 \mp \tan x\, \tan y} \quad \text{, gives}$$

$$F_{\text{motor}} \;=\; \frac{2\, T_{\text{motor}}}{d_{\text{spindle}}} \;=\; \tan(\alpha + \xi)\; F_{\text{load}} \quad . \tag{5.2}$$

A similar consideration gives the relation for the movement with the force of the spring,

$$F_{\text{motor}} \;=\; \frac{2\, T_{\text{motor}}}{d_{\text{spindle}}} \;=\; \tan(\alpha - \xi)\; F_{\text{load}} \quad . \tag{5.3}$$

Eq. (5.3) determines an important condition for the still standing times of the cycle. If

$$\arctan \frac{k_{\text{spindle}}}{d_{\text{spindle}}\, \pi} \;=\; \alpha \;\leq\; \xi \;=\; \arctan \mu \;=\; \arctan \frac{F_{\text{fric}}}{F_{\text{n}}} \quad , \tag{5.4}$$

the system is self-locking and means, there is no holding torque required to keep the actuator at a specific position.

The dimensions of the built-in spring are listed in Table 5.1 and result in a spring constant of

$$D_{\text{spring}} \;=\; \frac{G\, d_{\text{wire}}^4}{8\, d_{\text{spring}}^3\, n} \approx 17.0\, \frac{\text{N}}{\text{mm}} \quad ,$$

which is in poor agreement with the specifications listed Table 1.2.

Table 5.1: Parameters of the of the built-in spring.

Description	Symbol	Value	Unit
Shear modulus for stainless steel	G	73000	N/mm^2
Spring wire diameter	d_{wire}	2	mm
Spring mean diameter	d_{spring}	10	mm
Number of the springy coils	n	8.5	-
Spindle diameter	d_{spindle}	4.7	mm

$$\tan\alpha = \frac{k_{\text{spindle}}}{d_{\text{spindle}}\,\pi} \tag{5.5}$$

$$F_{\text{fric}} = \mu\, F_{\text{n}} \tag{5.6}$$

$$\mu = \tan\xi \tag{5.7}$$

$$F_{\text{n}} = F_{\text{n, motor}} + F_{\text{n, load}} \tag{5.8}$$

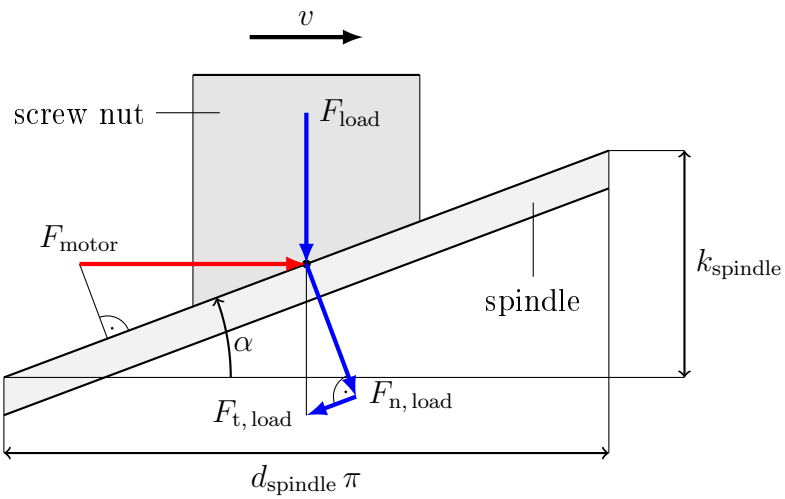

Figure 5.1: Forces on a flat thread assuming a relative movement of screw nut and spindle.

The torque, which has to be generated by the machine to run through the cycle, is given by

$$T_{\text{motor}} = I\,\frac{d^2}{dt^2}\varphi + T_{\text{load}}\,(x) + T_{\text{fric}} \quad . \tag{5.9}$$

The position depending load T_{load} is given by

$$T_{\text{load}} = \frac{d_{\text{spindle}}}{2}\left[\tan(\alpha + \xi)\,(F_{\text{min}} + D_{\text{spring}}\,x)\right] \quad , \tag{5.10}$$

for a movement against the force of the spring and by

$$T_{\text{load}} = \frac{d_{\text{spindle}}}{2}\left[\tan(\alpha - \xi)\,(F_{\text{min}} + D_{\text{spring}}\,x)\right] \quad , \tag{5.11}$$

for a movement with the force. For simplicity, it is assumed, that the friction torque is constant and does not depend on the rotational speed of the machine.

To provide a suitable comparison between measurements and simulations, it is essential to determine the mechanical constants of the system (T_{fric}, ξ, F_{min}) beforehand.

In the mechanical system no torque-sensing flange is installed, due to financial reasons. Therefore, for the IM the relation of eq. (A.46),

$$T_{\text{motor}} = \frac{3}{2}\,p\,\frac{L_{\text{h}}}{L_{\text{h}} + L_{\text{R}\sigma}}\,\Psi_{\text{Rd}}\,i_{\text{Sq}} \quad , \tag{5.12}$$

is used to obtain information concerning the torque. Though, this estimation depends on equivalent circuit parameters, which have some kind of uncertainty and on Ψ_{R} and i_{Sq}, which are again estimated using eq. (A.44),

$$\dot{\Psi}_{\mathrm{Rd}} = \frac{R_{\mathrm{R}}}{L_{\mathrm{h}} + L_{\mathrm{R}\sigma}} \left(L_{\mathrm{h}}\, i_{\mathrm{Sd}} - \Psi_{\mathrm{Rd}} \right) \quad , \tag{5.13}$$

and eq. (A.45)

$$\dot{\rho} = \dot{\varphi} + \frac{R_{\mathrm{R}}\, L_{\mathrm{h}}}{L_{\mathrm{h}} + L_{\mathrm{R}\sigma}} \frac{i_{\mathrm{Sq}}}{\Psi_{\mathrm{Rd}}} \quad . \tag{5.14}$$

For the SynRM, the relation of eq. (3.12),

$$T_{\mathrm{motor}} = \frac{3}{2} p \left(L_{\mathrm{d}} - L_{\mathrm{q}} \right) i_{\mathrm{d}}\, i_{\mathrm{q}} \quad , \tag{5.15}$$

is used, providing L_{d} and L_{q} in a lookup table, also afflicted with some kind of uncertainty.

5.2 Measurement Results IM

First, this Chapter discusses some differences between the original design and the manufactured machine (Section 5.2.1). If the equivalent circuit parameters used in the controller, do not fit to the machine, unphysical measurement results might be observed, illustrated in Section 5.2.2. The parameters of this actuator, determined with a method presented in Section 5.2.3, are used in Section 5.2.4 to compare simulation and measurement results. An improvement of the controller design to reduce losses during the still standing times of the cycle is presented in Section 5.2.5.

The stator and rotor of the manufactured IM are depicted in Fig. 5.2.

(a) Stator of the manufactured IM. (b) Rotor of the manufactured IM.

Figure 5.2: Stator (left) and rotor (right) of the manufactured IM.

5.2.1 Deviation from Original Design

The machine was supposed to be manufactured according to Table 4.3 and Fig. 4.3. Due to limitations of production accuracy, some differences between the delivered motor and the computed design occur, listed subsequently.

- Air gap length δ

  Its nominal length is defined with 0.2 mm, but the production accuracy of the manufacturer for the outer diameter of the rotor is specified with ± 0.05 mm. This directly influences the length of the air gap, accordingly its magnetic voltage drop (c.f. eq. (A.8)) and further the main inductance [37, Eq. 3.110] of the machine.

  Simulation has shown that at the nominal working point of the machine's original design, the ratio of the magnetic voltage drop of the air gap $\hat{U}_\delta$ and the iron path $\hat{U}_{\mathrm{Fe}}$ is

  $$\frac{\hat{U}_\delta}{\hat{U}_{\mathrm{Fe}}} \approx \frac{4}{9} \quad .$$

  This factor is used to estimate the maximum deviation of the main inductance caused by the change of the air gap. This assumption is only valid for small differences of the real air gap compared to the original design. The main inductance L_{h} is also influenced by

the outer diameter of the rotor (c.f. eq. (5.19)), but this is of small impact and neglected in this consideration.

The real air gap δ^* (denoted with a superscript $*$) results from the computed one. The factor f is introduced to consider the manufacturing inaccuracy.

$$\delta^* \;=\; \delta\, f \qquad f \in \left[\frac{15}{20},\, \frac{25}{20}\right] \tag{5.16}$$

Eq. (A.13) describes the effective air gap,

$$\delta_{\text{eff}} \;=\; \frac{\hat{U}_\delta + \hat{U}_{\text{Fe}}}{\hat{U}_\delta}\, k_{\text{C}}\, \delta \;=\; \frac{k_{\text{C}}\, \delta}{\hat{U}_\delta}\, \hat{U}_{\text{Fe}} \left(1 + \frac{\hat{U}_\delta}{\hat{U}_{\text{Fe}}}\right) \quad . \tag{5.17}$$

The air gap δ cancels in the first term of eq. (5.17), since

$$\hat{U}_\delta \;=\; \frac{\delta\, k_{\text{C}}}{\mu_0}\, \hat{B}_\delta \quad ,$$

and therefore the true effective air gap δ^*_{eff} results in eq. (5.18).

$$\begin{aligned} \frac{\delta^*_{\text{eff}}}{\delta_{\text{eff}}} \;&=\; \frac{1 + \frac{\hat{U}_\delta}{\hat{U}_{\text{Fe}}}\, f}{1 + \frac{\hat{U}_\delta}{\hat{U}_{\text{Fe}}}} \;=\; \frac{1 + \frac{4}{9}\, f}{1 + \frac{4}{9}} \;=\; \frac{9 + 4\, f}{13} \;\overset{!}{=}\; f' \\ \delta^*_{\text{eff}} \;&=\; f'\, \delta_{\text{eff}} \qquad f' \in [0.92,\, 1.08] \end{aligned} \tag{5.18}$$

Since the main inductance of the induction machine is inversely proportional to δ_{eff},

$$L_{\text{h}} \;=\; 2\, \mu_0\, m \left(\frac{w_{\text{str}}\, \xi}{\pi}\right)^2 \frac{l_{\text{Fe}}\, \tau_{\text{p}}}{p\, \delta_{\text{eff}}} \quad , \tag{5.19}$$

the deviation caused by the production uncertainty is about 9 %.

- The distance between the outer diameter of the rotor and the rotor bar h_{bar}

  This parameter of the rotor geometry is similar to the length of the air gap, directly influenced by a change of the nominal diameter of the rotor and causes a change of the rotor leakage inductance (c.f. Section 2.2.1.1 and Fig. 2.3).

  This effect is not that easy to quantify, because $L_{\text{R}\sigma}$ highly depends on the saturation of the flux bridge, which changes with the actual point of operation.

- The diameter of the rotor bar d_{bar}

  Certainly, the diameter of the rotor bars has to be smaller than its borehole. The manufacturer uses a wire with a diameter of 1.4 mm, whereby the ohmic resistance of the rotor[1] R_{R} increases by approximately 8 % when compared to the originally expected one.

- The slot fill factor and the length of the end winding

  A measurement of the ohmic resistance of the stator yields

  $$R_{\text{S}} \;=\; 0.19\,\Omega \quad \text{at} \quad T \;=\; 100\,^\circ\text{C} \quad . \tag{5.20}$$

  This is approximately 32 % higher than originally expected and results from

[1] Transfered to the stator.

1. a slot fill factor of about 40.5 % instead of 50.0 % and
2. lengthy winding overhangs of approximately 14 mm respectively 16 mm in contrast to the design of 10 mm.

Another element of uncertainty in the computations is given by the magnetisation characteristic of the electrical steel sheets. For the original machine design, the magnetisation characteristic originates from a benchmark study. The edges of electrical steel sheets are particularly influenced by the degradation caused by the cutting - here laser cutting - process [68, 69]. This will notably affect small machines with small teeth. Hence, the magnetisation characteristics of the machine will differ from the original estimation. However, this effect is very difficult to predict, given the current state of knowledge, but can have a great impact on the inductances of the machine L_h and $L_{\mathrm{R}\sigma}$.

The influence of different magnetisation characteristics on L_h is illustrated in Fig. C.2. For the computations the modelling approach of Section 2.2.1 and a geometry according to Fig. 4.3 are used. The two curves in Fig. C.2 may be seen as upper and lower bound for L_h. Therefore, it can be assumed that L_h of the manufactured machine is located somewhere between these two extremes.

The influence on $L_{\mathrm{R}\sigma}$ is, again, difficult to quantify.

5.2.2 Influence of Badly Estimated Parameters

To illustrate the influence of badly estimated equivalent circuit parameters, the actuator is forced to change its position from minimum to maximum range and back with constant speed

$$n \;=\; \frac{14\,\mathrm{mm}\,2\,\pi}{k_\mathrm{spindle}\,5\,\mathrm{s}}\,\frac{30}{\pi} \;=\; \text{const.} \;=\; 105\,\mathrm{min}^{-1} \quad .$$

Thus, the acceleration term in eq. (5.9) cancels and for simplification the spring is not pre-stressed, hence

$$F_\mathrm{min} \;=\; 0 \quad .$$

For this situation, the mechanical model predicts a linear relation between motor torque and the actuator position x,

$$T_\mathrm{motor} \;\propto\; D_\mathrm{spring}\,x \quad ,$$

what is in poor agreement with the estimated torque, resulting from measurements, for the movement against the force of the spring, presented in Fig. 5.3.

The reason for the observed non-linear relation indicates that either the main inductance L_h, the rotor resistance R_R or the rotor leakage inductance $L_{\mathrm{R}\sigma}$, used for the online estimation of T_motor, Ψ_Rd and ρ (see eqs. (5.12) to (5.14)), do not fit to the machine.

The rotor resistance is determined by the geometry and the winding, which is well known, but during operation it is influenced by temperature. The following assessment gives an upper bound for the change of R_R caused by temperature during the movement against the spring: Let us estimate the torque generating current with $i_\mathrm{Sq} = \max(i_\mathrm{S}\,(t)) = 12\,\mathrm{A}$ (maximum current within this experiment, c.f. Fig. 5.6) and the rotor resistance with $R_\mathrm{R} = 0.25\,\Omega$, which is also quite high. This gives a heat energy transferred to the rotor of

$$Q \;=\; P_\mathrm{Cu}\,\Delta t \;\approx\; \frac{3}{2}\,R_\mathrm{R}\,i_\mathrm{Sq}^2\,\Delta t \;=\; \frac{3}{2}\,12^2 \cdot 0.25 \cdot 5\,\mathrm{J} \;=\; 270\,\mathrm{J} \quad .$$

The bars and the laminated sheet package of the rotor are mechanically strongly connected with each other. Hence, good thermal coupling between them and almost an instantaneous distribution of the heat energy Q is assumed.
The mass of the rotor (neglecting the end rings) is approximately $m_{\mathrm{rotor}} \approx 0.12\,\mathrm{kg}$ and the specific heat capacity of iron is $c_{\mathrm{Fe}} = 452\,\mathrm{J/(kg\,K)}$, which gives a maximum temperature rise of

$$\Delta T \;=\; \frac{Q}{m_{\mathrm{rotor}}\, c_{\mathrm{Fe}}} \;\approx\; \frac{270}{0.12 \cdot 452}\,\mathrm{K} \;\approx\; 5\,\mathrm{K} \quad .$$

This causes a maximum change of resistance of

$$R_{\mathrm{R}}\,(T + \Delta T) \;<\; R_{\mathrm{R}}\,(T)\;(1 + \alpha_{\mathrm{Cu},\,20}\,\Delta T) \;=\; R_{\mathrm{R}}\,(T)\,1.02 \quad ,$$

which is insignificant within this experiment.

The impact of inaccuracies on machine-parameters is for example discussed in [70].

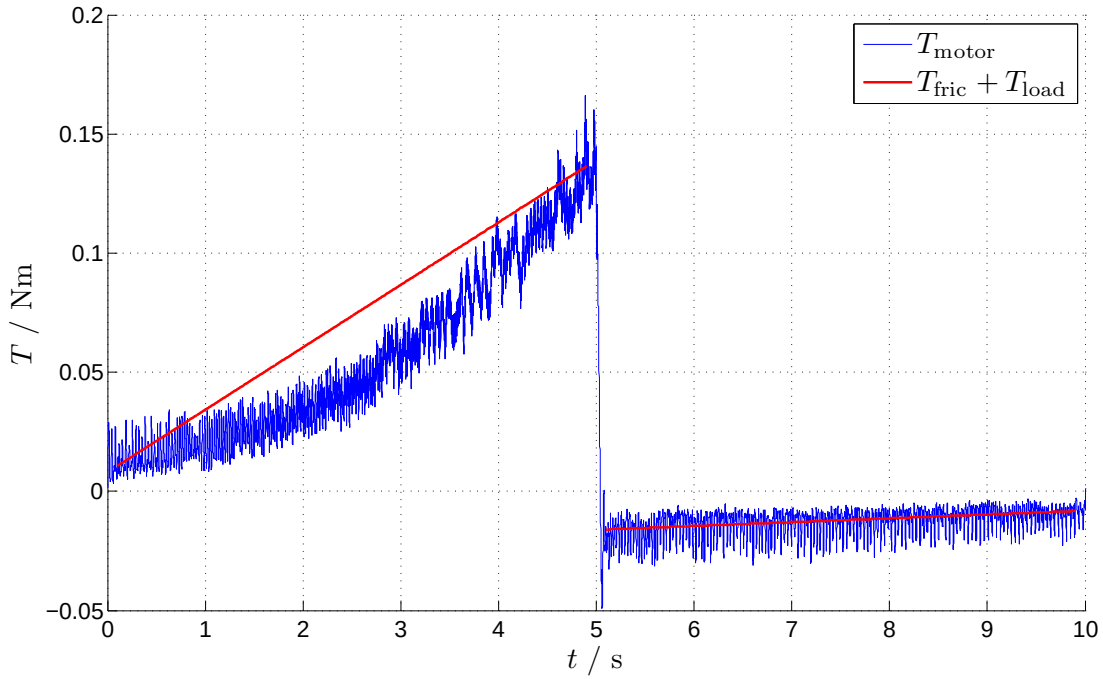

Figure 5.3: Estimated torque T_{motor} (eq. (5.9)) vs. time t (blue) for a position change of the actuator with constant speed between minimum and maximum range to estimate the material constant ξ. The red line shows the result predicted by theory, presented in Section 5.1.

In the context of this work, simulations are used to illustrate the influence of badly estimated equivalent circuit parameters on its produced torque and the rotor flux, since these values are easily available.

Figs. 5.4 and 5.5 show simulation results for the scenario that L_{h} or $L_{\mathrm{R}\sigma}$ are badly estimated as a function of the real produced torque of the machine. In these cases parameters marked with a superscript "est" are used for the online calculation of eqs. (5.12) to (5.14). The other parameters are used to model the machine or denote the real produced torque and rotor flux.

From these calculations follows:

- A wrongly estimated rotor flux $\Psi_{\mathrm{R,\,est}}$ causes a wrong estimation of the torque $T_{\mathrm{motor,\,est}}$. This mismatch is compensated by a change of i_{Sq} to generate the torque given by the load. The magnitude of the change depends on the nominal value of Ψ_{R} and therefore from the distance between the actual operating point and the maximum torque per ampere point.
- Even if all parameters used for the flux estimation match the parameters used for the machine modelling there is a mismatch between the real flux (torque) and the estimated one. This is why the approximation $\Psi_{\mathrm{h}} \approx \Psi_{\mathrm{R}}$ is used in the flux observer.
- A wrongly estimated rotor leakage inductance $L_{\mathrm{R}\sigma}$ has a small impact on the estimated torque for a minor load.

Fig. 5.6 presents a comparison of the measured stator current according to Fig. 5.3 and simulation results.

The flux observer on the test bench uses the same set of parameters as the simulation. The simulation in Fig. 5.6a uses the same equivalent circuit parameters for modeling the machine as for the flux observer. The values for L_{h} and $L_{\mathrm{R}\sigma}$ to model the machine within the simulation in Fig. 5.6b are adjusted to the observed data using the least-squares method.

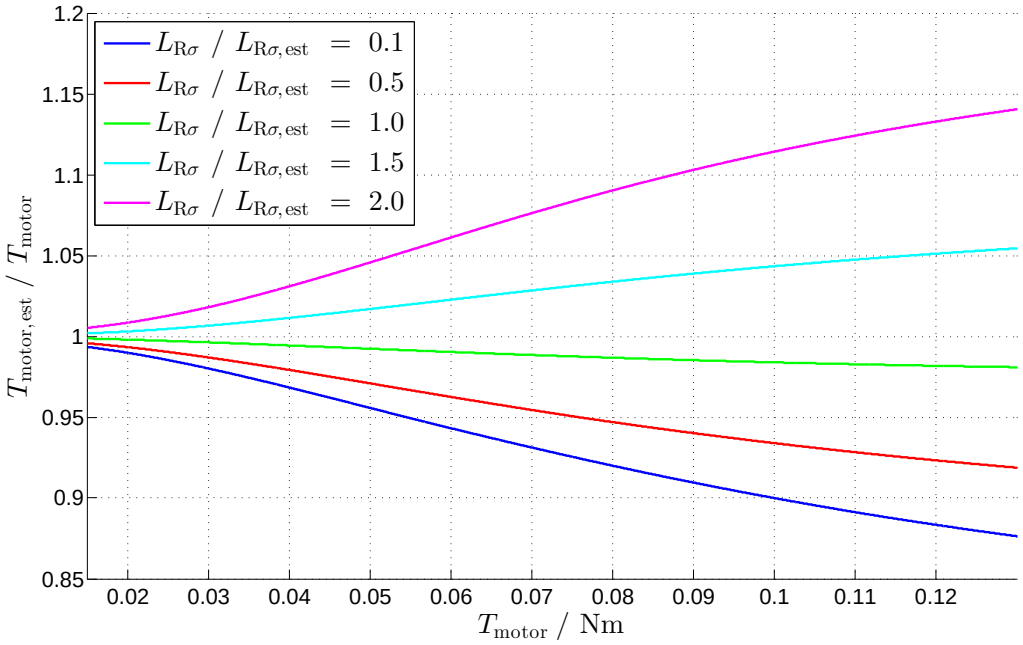

(a) Estimated torque $T_{\text{motor,est}}$ versus real torque T_{motor} as a function of T_{motor} for a nominal value of $\Psi_{\text{R}} = 0.0095\,\text{Vs}$. $L_{\text{R}\sigma}$ is used to model the machine and $L_{\text{R}\sigma,\text{est}}$ for the flux observer.

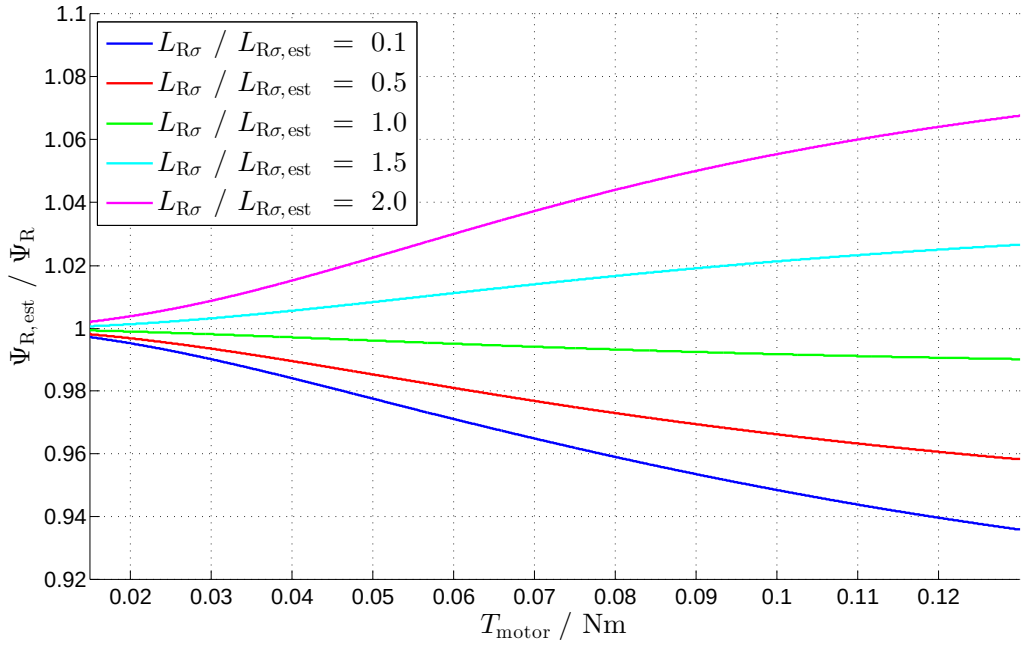

(b) Observed rotor flux $\Psi_{\text{R,est}}$ versus real value of Ψ_{R} as a function of T_{motor} for a nominal value of $\Psi_{\text{R}} = 0.0095\,\text{Vs}$. $L_{\text{R}\sigma}$ is used to model the machine and $L_{\text{R}\sigma,\text{est}}$ for the flux observer.

Figure 5.4: Simulation results to illustrate the influence on the observed rotor flux and the estimated torque for a badly estimated rotor leakage inductance.

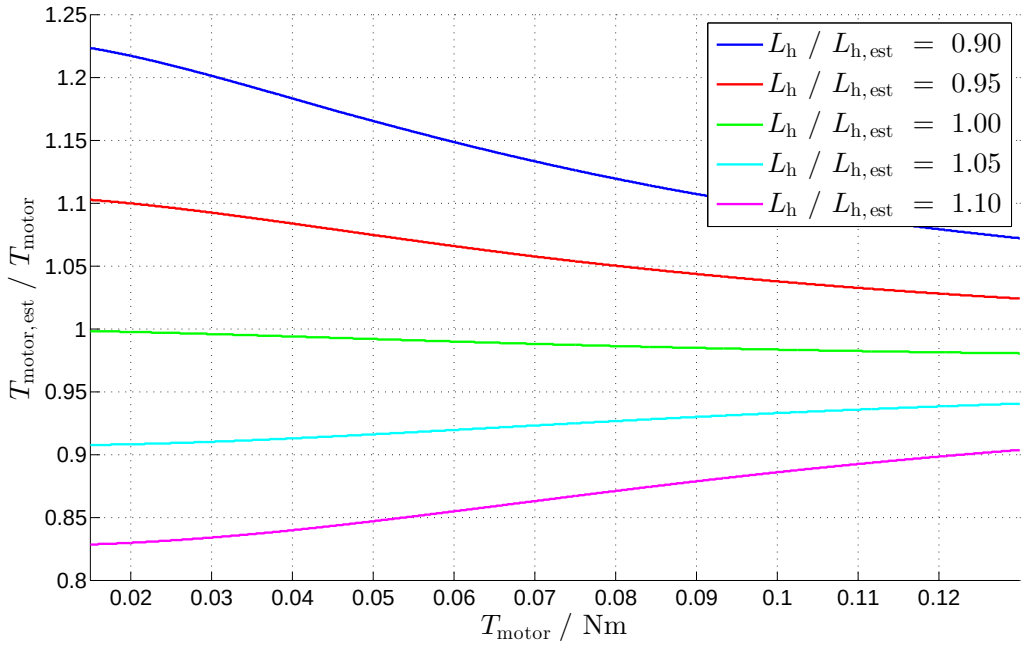

(a) Estimated torque $T_{\mathrm{motor,\,est}}$ versus real torque T_{motor} as a function of T_{motor} for a nominal value of $\Psi_{\mathrm{R}} = 0.0095\,\mathrm{Vs}$. L_{h} is used to model the machine and $L_{\mathrm{h,\,est}}$ for the flux observer.

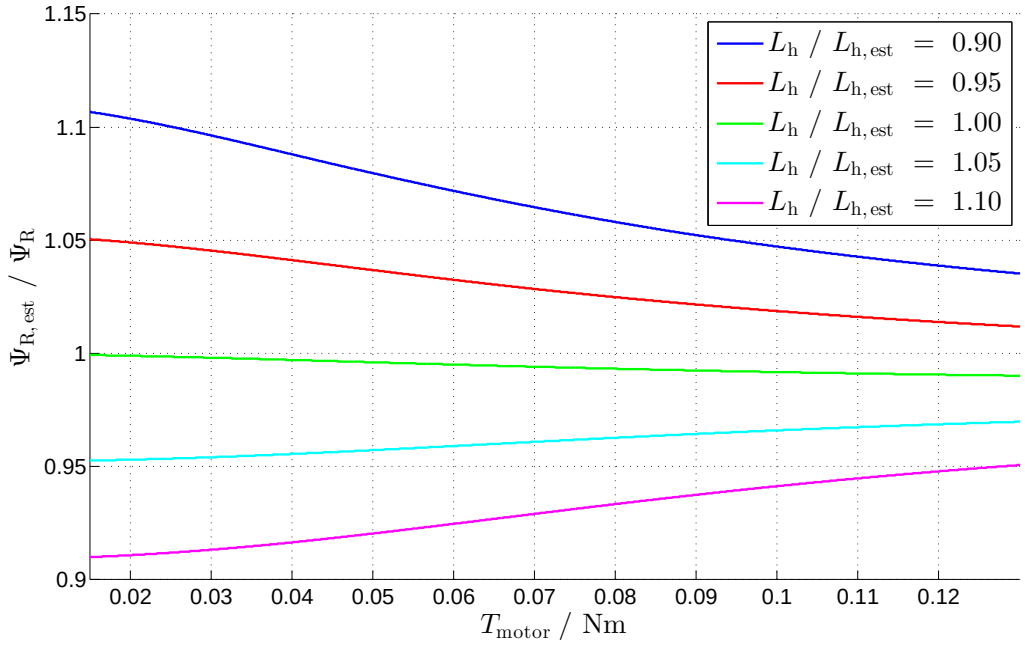

(b) Observed rotor flux $\Psi_{\mathrm{R,\,est}}$ versus real value of Ψ_{R} as a function of T_{motor} for a nominal value of $\Psi_{\mathrm{R}} = 0.0095\,\mathrm{Vs}$. L_{h} is used to model the machine and $L_{\mathrm{h,\,est}}$ for the flux observer.

Figure 5.5: Simulation results to illustrate the influence on the observed rotor flux and the estimated torque for a badly estimated main inductance.

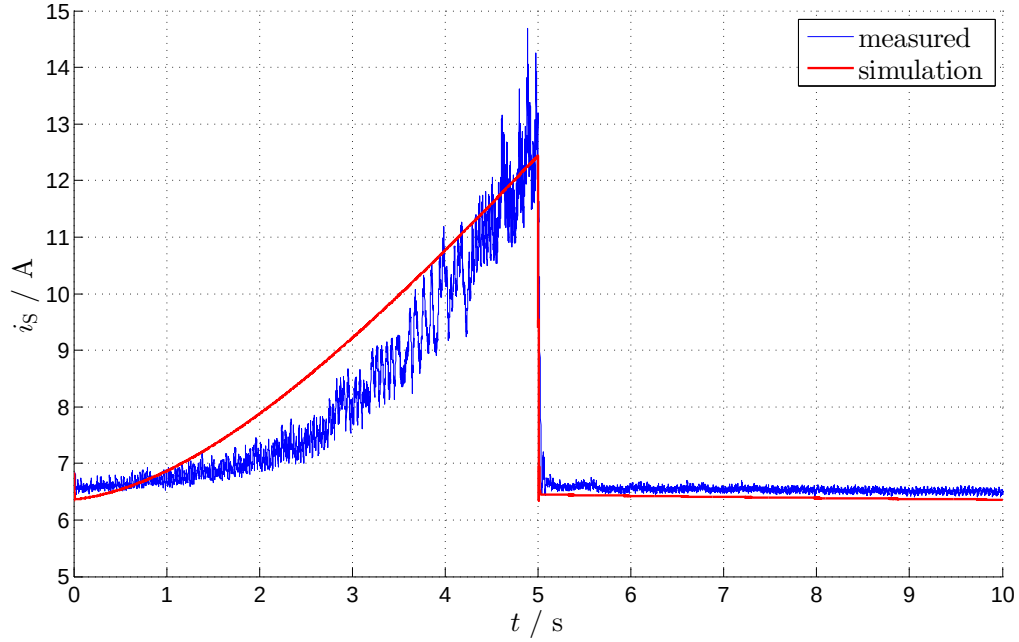

(a) Stator current i_S vs. time t. The flux observer on the test bench operates with the same set of parameters as the simulation. The simulation uses the same equivalent circuit parameters for modeling the machine.

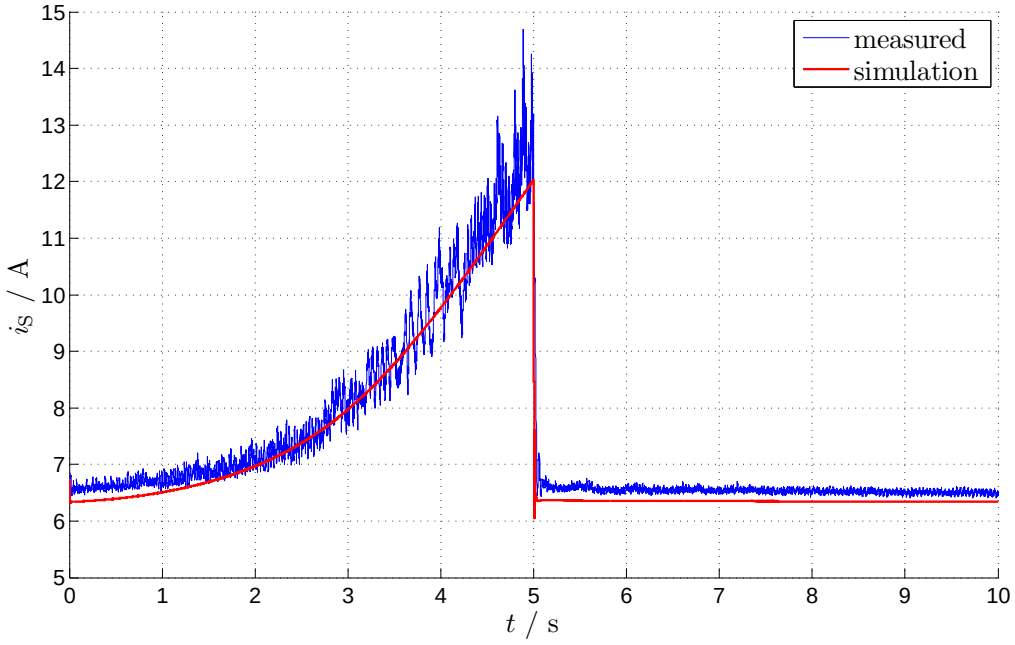

(b) Stator current i_S vs. time t. The flux observer on the test bench operates with the same set of parameters as the simulation. The equivalent circuit parameters used to model the machine within the simulation are adjusted to the measured data.

Figure 5.6: Comparison of the measured stator current according to Fig. 5.3 and simulation results for a movement of the actuator against the spring and back with constant speed.

5.2.3 Parameter Identification

This Section presents an ansatz to identify L_h, $L_{\mathrm{R}\sigma}$ and the mechanical constants T_fric and ξ of the actuator. Certainly, for a suitable comparison between simulations and measurements a knowledge of these parameters with sufficient accuracy is indispensable

In literature, numerous techniques relating to online and offline parameter estimation of a rotor flux oriented controlled induction machine are discussed and are summarised in e.g. [71]. Due to lack of alternatives, a simple offline parameter adaptation based on a torque reference, provided by the mechanical model of the actuator, (eqs. (5.10) and (5.11)), is used. But the constants T_fric and ξ have to be determined as well. This is why this method, presented in the following and illustrated in Fig. 5.8, contains iterative loops to achieve self-consistent results.

1. The iteration starts with an initial guess for L_h and $L_{\mathrm{R}\sigma}$.
2. The actuator is forced to move within its maximal range with constant speed, once with an installed spring and once without. This is a task on the test bench!
3. The estimation of the torque, eq. (5.12), is used to compute a new value for T_fric and ξ.
4. The method of least squares is used to adjust the simulation, based on the new values of T_fric and ξ, to the results from the test bench and gives a new guess for L_h and $L_{\mathrm{R}\sigma}$.
5. This procedure is repeated until the estimation of the torque and the mechanical model are in agreement up to a certain level.

Fig. 5.7 shows a repetition of the experiment presented in Fig. 5.3, which shows a linear relation of the estimated torque and the position $x \propto t$ of the actuator, as predicted by theory.

The rotor leakage inductance is constant within the simulation, but its value will change during operation. Thus, in the strict sense the obtained result is only valid for one point of operation.

5.2.4 Comparison: Measurement & Simulation

This Section presents a comparison of simulation and measurement results of the actuator, while the actuator runs through the complete cycle (Figs. 5.9 and 5.10). The corresponding parameters of the mechanic are listed in Table 5.2.

- The graphs for the q-axis current i_Sq and the estimated torque T_motor, using eq. (5.12), are in good agreement during the periods of the cycle, which demand a movement of the actuator.

  An exception is given in the period of the cycle between $t = 8\,\mathrm{s}$ and $t = 12\,\mathrm{s}$ for a movement against the force of the spring. It seems that in these phases the flux bridges of the slot tooth layer of the rotor are more saturated and therefore the slot leakage inductance is smaller than initially estimated. This causes an estimation of the rotor flux, which is considerably smaller than in reality, c.f. Fig. 5.4b, and has to be compensated by a rise of i_Sq. Certainly, this also causes a wrong estimation of T_motor, c.f. Fig. 5.4a.

- In contrast to the prediction of the mechanical model, the machine produces torque during the still standing times of the cycle.

  At this time, the actuator has reached its nominal position within fractions of millimeters and the machine has accordingly reduced its speed close to zero. In this speed range the

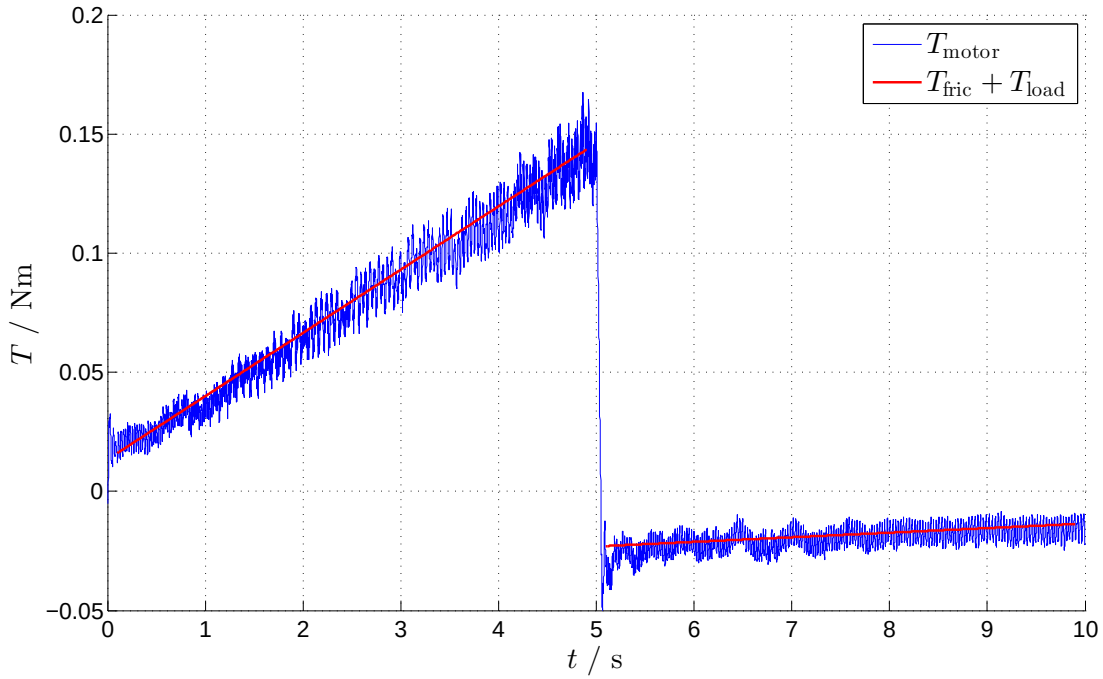

Figure 5.7: Comparison of the estimated torque of the machine T_{motor} and the predicted torque based on the mechanical model ($T_{\text{fric}} = 13.5 \cdot 10^{-3}$, $\xi = 0.125$, $F_{\text{min}} = 0$) for a movement of the actuator against the spring and back with constant speed.

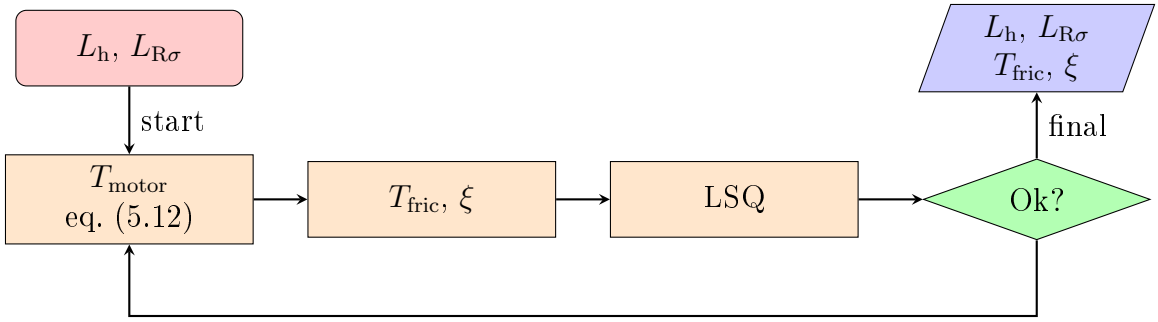

Figure 5.8: Schematic diagram of the iteration to adapt the equivalent circuit parametes L_{h} and $L_{\text{R}\sigma}$ and to determine the constants T_{fric} and ξ, LSQ . . . Least Square Method.

static friction term dominates, which causes a comparatively high torque to compensate this position control deviation. This effect cannot be seen in the simulation, because stiction is not considered within the mechanical model.

If the position of the actuator is within the tolerances given by the specification, c.f. Table 1.1, the effort of the controller to reach the exact position is not absolutely essential for this application and causes avoidable losses. A small change in the design of the controller, presented in Section 5.2.5, provides a remedy for this problem.

- The graphs for speed n and position x as a function of time t are almost equal, except for the abrupt changes of position of the cycle. In these phases, simulation and measurement results differ slightly from each other, probably caused by inaccuracies in the estimation of the torque of inertia of the system.

- The mean copper losses to run through the cycle are estimated according to

$$\overline{P}_{\mathrm{Cu}} \approx \frac{1}{12}\int_0^{12} \frac{3}{2}\left[R_{\mathrm{S}}\left(i_{\mathrm{Sd}}^2(t)+i_{\mathrm{Sq}}^2(t)\right)+R_{\mathrm{R}}\,i_{\mathrm{Sq}}^2(t)\right]dt \quad .$$

The results between simulation and measurement differ by approximately 20 %, mainly caused by the holding torque during the still standing times of the cycle. In the present case the results of the simulation has to be interpreted as lower limit for the copper losses.

Converting the temperature of the winding to 100 °C would increase the copper losses by

$$1+\alpha_{\mathrm{Cu},20}\,(100-35) = 1+3.93\cdot 10^{-3}\,(100-35) \approx 1.26 \quad ,$$

for the simulation as well as for the measurement. This is still lower than originally expected (see eq. (4.1)), despite higher values for the stator and rotor resistances (c.f. Section 5.2.1) caused by manufacturing.

This is, on the one hand, explained by the properties of mechanical system of the test bench. They differ from the specifications, which result in a different value for the effective torque of the cycle. With the implemented controller design, the effective torque is proportional to the square of the copper losses, determined by

$$P_{\mathrm{Cu}} \propto R_{\mathrm{S}}\,i_{\mathrm{Sd}}^2+(R_{\mathrm{S}}+R_{\mathrm{R}})\,i_{\mathrm{Sq}}^2 = P_{\mathrm{Cu,\,flux}}+\underbrace{P_{\mathrm{Cu,\,torque}}}_{\propto T_{\mathrm{RMS}}^2} \quad .$$

On the other hand, the main inductance of the manufactured machine has increased compared to the original design. For this reason, less magnetising current is needed for the same rotor flux.

Table 5.2: Estimated parameters and results for the actuator to run through the cycle.

Description	Symbol	Value	Unit
Spring constant	D_{spring}	17	N/mm
Spindle diameter	d_{spindle}	4.7	mm
Spindle material constant	ξ	0.13	-
Additional friction torque	T_{fric}	$13.5 \cdot 10^{-3}$	Nm
Counterforce at minimum position of the actuator	F_{min}	0	Nm
Estimated mass moment of inertia of the system	I_{system}	$1.44 \cdot 10^{-5}$	kgm^2
Estimated effective torque of the cycle (simulation)	T_{RMS}	$48 \cdot 10^{-3}$	Nm
Nominal rotor flux	Ψ_{R}	$9.5 \cdot 10^{-3}$	Vs
Temperature of the winding during the experiment	-	35	°C
Estimated mean copper losses of the simulation	$\overline{P}_{\text{Cu, sim}}$	10.2	W
Estimated mean copper losses of the measurement	$\overline{P}_{\text{Cu, meas}}$	12.3	W

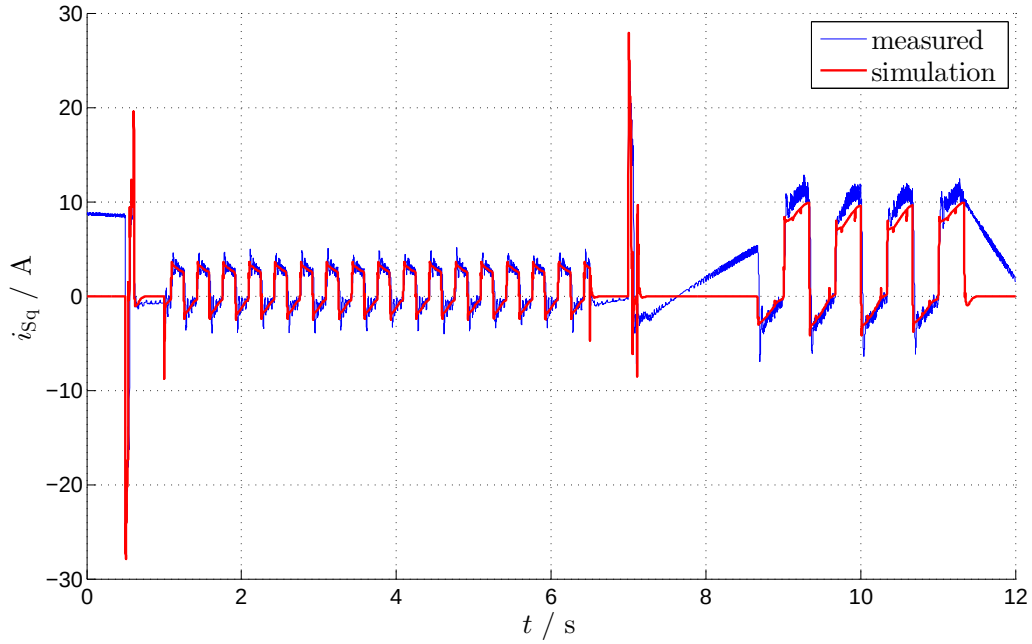

(a) Comparison between measurement (blue) and simulation (red) of the torque generating current i_{Sq} as a function of time t.

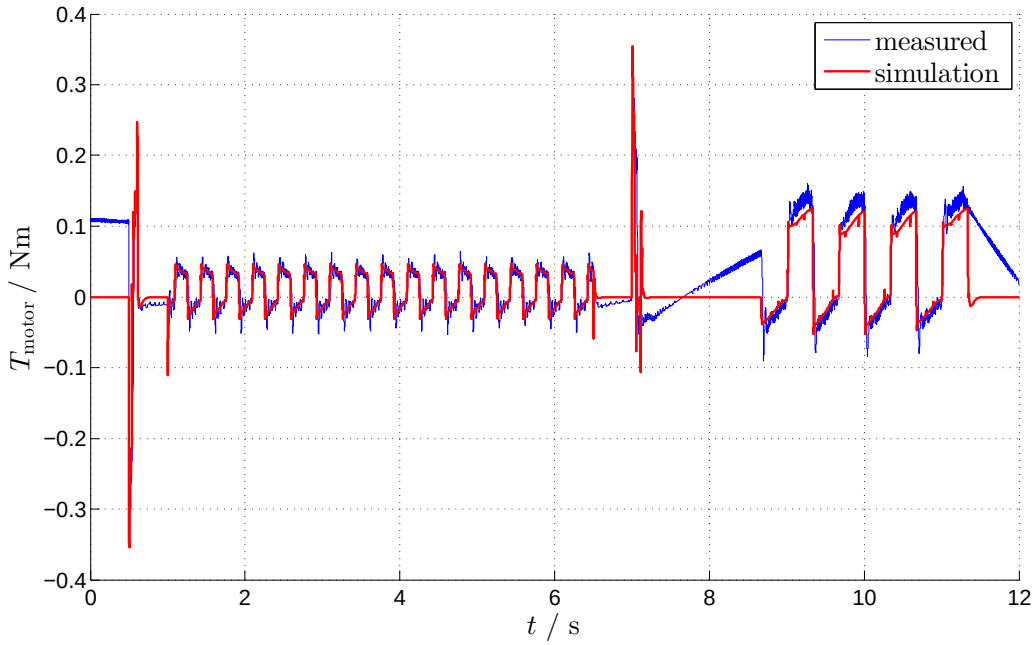

(b) Comparison between measurement (blue) and simulation (red) of the estimated torque T_{motor} as a function of time t.

Figure 5.9: Comparison of measurement and simulation results of the actuator equipped with the IM to run through the cycle.

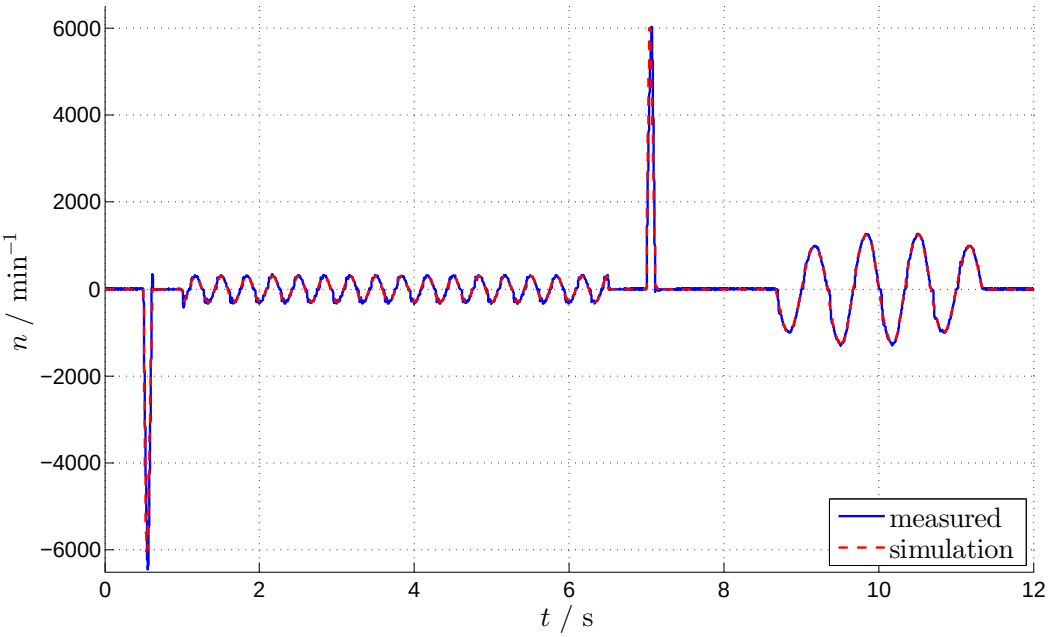

(a) Comparison between measurement (blue) and simulation (red) of the actuator's speed n as a function of time t.

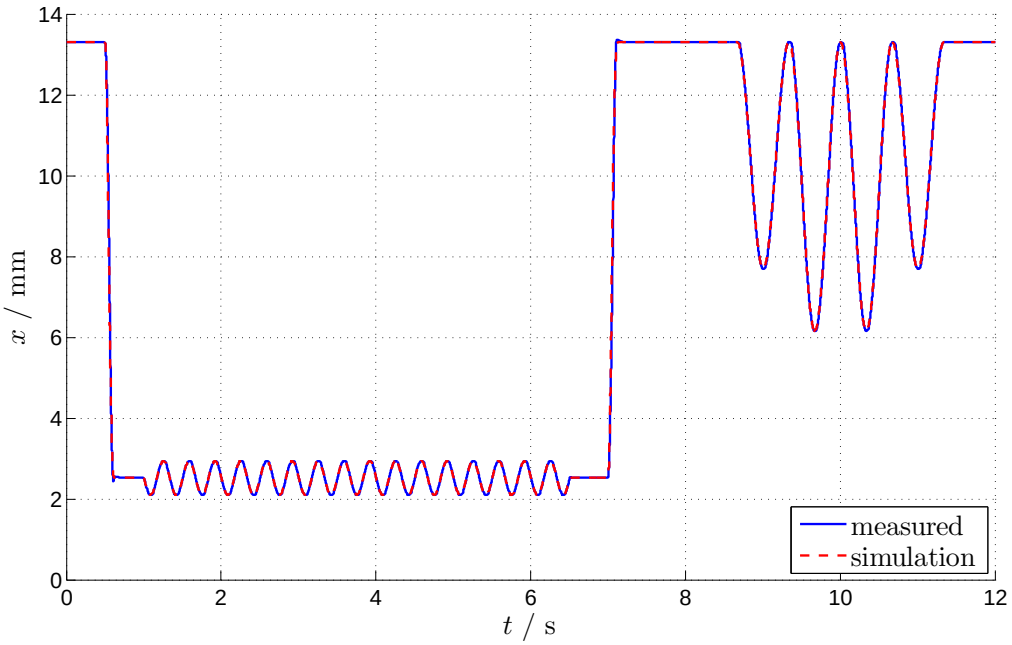

(b) Comparison between measurement (blue) and simulation (red) of the actuator's position x as a function of time t.

Figure 5.10: Comparison of measurement and simulation results of the actuator equipped with the IM to run through the cycle.

5.2.5 Zero Torque Control

Due to minor position control deviations, the machine also produces a torque during the still standing times of the cycle, c.f. Fig. 5.9. In addition, this torque is comparatively high because in a speed range of $n \ll 1$ the static friction term dominates. Assuming that the actuator has already reached its nominal position within the tolerances given by the application, this property of the controller is not absolutely essential and causes avoidable losses.

Minor modifications of the original controller design, presented in Section 2.3.1, eliminate this problem. Therefore, two additional conditions have to be included in the controller.

1. Detect a change of the nominal position value x^*,

$$|x^*(t_\mathrm{k}) - x^*(t_{\mathrm{k}-1}))| \; < \; \epsilon \quad \text{and} \tag{5.21}$$

2. check the actual position control deviation,

$$|x(t_\mathrm{k}) - x^*(t_\mathrm{k}))| \; < \; \Delta x \quad . \tag{5.22}$$

In this context, t_k denotes the time at the k^{th} sampling instance. If eqs. (5.21) and (5.22) are fulfilled, the nominal value for the torque generating current is now set to zero.

The consequence of this controller modification is shown in Fig. 5.11, in comparison with the original controller design.

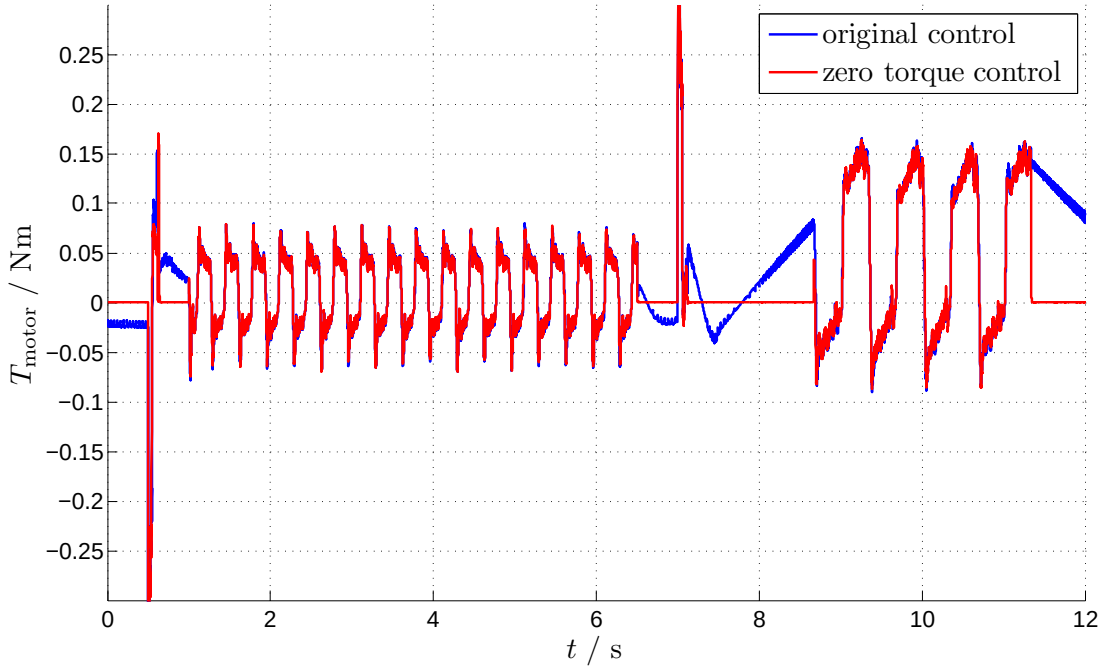

Figure 5.11: Measurement results of the estimated torque T_{motor} as a function of time t to run through the cycle. This Fig. shows a comparison of the controller design as presented in Section 2.3.1 (blue line) and the modification (red line), which sets torque generating current to zero, if eqs. (5.21) and (5.22) are fulfilled.

5.3 Measurement Results SynRM

Again, at first, this Chapter discusses the differences between the manufactured motor and the computed design (Section 5.3.1). Results of the parameter identification of the SynRM are presented in Section 5.3.2 and a comparison between simulation and measurement results, while the actuator runs through the complete cycle, in Section 5.3.3.

The stator and rotor of the manufactured SynRM are depicted in Fig. 5.12.

(a) Stator of the manufactured SynRM. (b) Rotor of the manufactured SynRM.

Figure 5.12: Stator (left) and rotor (right) of the manufactured SynRM.

5.3.1 Deviation from Original Design

The machine was supposed to be manufactured according to Table 4.6 and Fig. 4.5. Due to limitations of production accuracy, also for the SynRM, in particular the slot fill factor and the length of the end winding differ from the computed design.

A measurement of the ohmic resistance of the stator yields

$$R_\mathrm{S} = 0.46\,\Omega \quad \text{at} \quad T = 100\,^\circ\mathrm{C} \quad . \tag{5.23}$$

This is approximately 50 % higher than originally expected and results mainly from a slot fill factor of about 35.9 % instead of 50.0 %.

Again, the other element of uncertainty in the computations is given by the magnetisation characteristic of the electrical steel sheets. For the original machine design, the magnetisation characteristic originates from a benchmark study. The edges of electrical steel sheets are particularly influenced by the degradation caused by the cutting - here laser cutting - process. This will notably affect small machines with small teeth. Hence, the magnetisation characteristics of the machines will differ from the original estimation. However, this effect is very difficult to predict, given the current state of knowledge, but can have a great impact on the inductances of the machines.

5.3.2 Parameter Identification

The SynRMs controller needs information about the d- and q-axis inductance as a function of the stator current i_S. Therefore, simple DC voltage step response experiments (at standstill and locked rotor) were performed to obtain data used to compute L_d and L_q with the method of least squares. The transfer function is assumed to be a RL circuit.
The results are provided for the controller within lookup tables and are shown in Fig. 5.13a.

Also for the SynRM, a knowledge of the mechanical constants of the actuator, T_fric and ξ, and the magnetic properties of the machine is indispensable to provide a suitable comparison between simulation and measurement results.

Therefore, a procedure, similar to the IM (c.f. Section 5.2.3), is realised. Again, the actuator is forced to move within its maximal range with constant speed, once with an installed spring and once without. The measurement results are iteratively used to determine the mechanical parameters of the actuator and to adjust the underlying two-dimensional lookup table of the SynRMs simulation model.

A comparison of measurement and simulation results, using the parameters of the final iteration, for a movement of the actuator against the spring and back with constant speed is shown in Fig. 5.13b, exemplary for the stator current i_S.

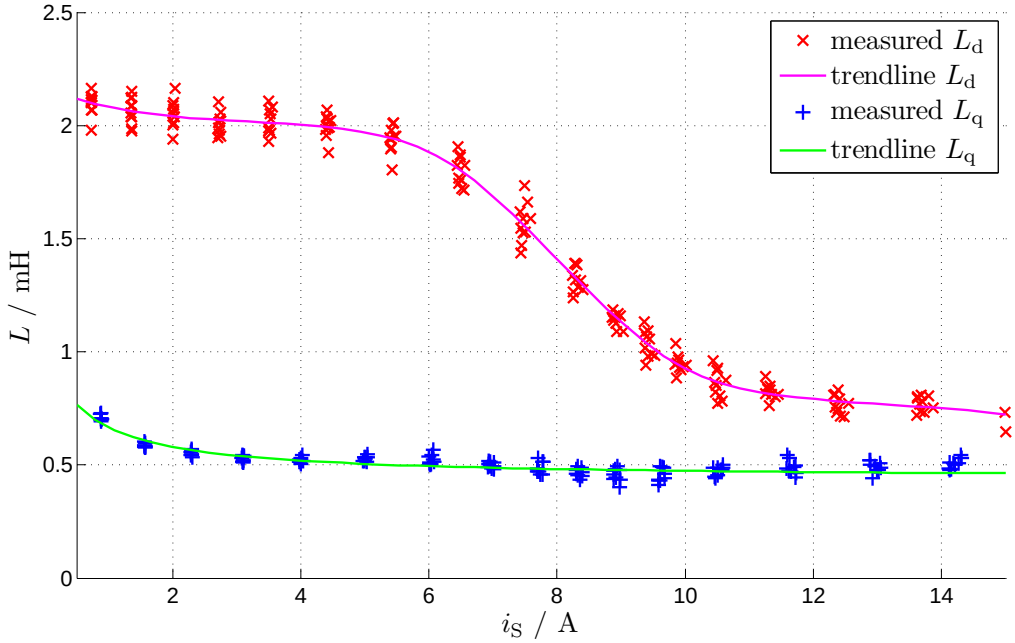

(a) Results of standstill DC experiments to obtain information of the d and q-axis inductance as a function of the stator current i_S.

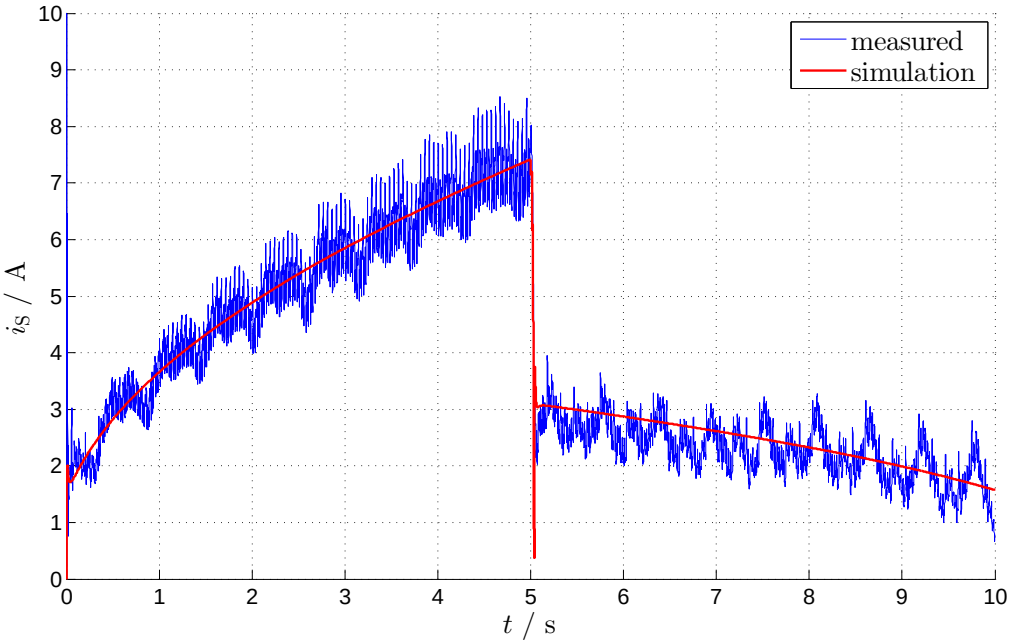

(b) Comparison between measurement and simulation results of the stator current i_S for a movement of the actuator against the spring and back with constant speed.

Figure 5.13: Results of the parameter identification of the SynRM.

5.3.3 Comparison: Measurement & Simulation

This Section presents a comparison of simulation and measurement results of the actuator equipped with the SynRM, while the actuator runs through the complete cycle (Figs. 5.14 and 5.15). The corresponding parameters of the mechanic are listed in Table 5.3.

- The performance of the SynRM as it runs through the required cycle, exemplified by the stator current i_S, is shown in Fig. 5.14.

  The differences between simulation and measurement results observed for the high dynamic phases (see also Fig. 5.15) are explained by uncertainties about the mechanical constants and properties of the test bench, such as dead times and static friction, which are not or insufficiently considered in the model.

- The mean copper losses to run through the cycle are estimated according to

$$\overline{P}_{\mathrm{Cu}} \;=\; \frac{1}{12}\int_0^{12} \frac{3}{2}\, R_S\, i_S^2\,(t)\, dt \quad .$$

  For the SynRM, the results between simulation and measurement are equal. This is why the modification of the controller, which sets the stator current to zero, if the actuator's position is within the required tolerances, described in Section 5.2.5, is already implemented during the measurements for these graphs.

  Converting the temperature of the winding to 100 °C would increase the copper losses by

$$1 + \alpha_{\mathrm{Cu},\,20}\,(100 - 35) \;=\; 1 + 3.93 \cdot 10^{-3}\,(100 - 35) \;\approx\; 1.26 \quad ,$$

  for the simulation as well as for the measurement. This is still lower than originally expected (see eq. (4.2)), despite a higher value for the stator resistance (c.f. Section 5.3.1) caused by manufacturing.

  This is, on the one hand, again explained by the properties of mechanical system of the test bench. They differ from the specifications, which results in a different value for the effective torque of the cycle.

  On the other hand, the inductances of the manufactured machine has changed for the better, compared with the original computations, see Appendix B, based on the magnetisation characteristic derived from a benchmark study (c.f. Appendix C).

Table 5.3: Estimated parameters and results for the actuator to run through the cycle.

Description	Symbol	Value	Unit
Spring constant	D_{spring}	17	N/mm
Spindle diameter	d_{spindle}	4.7	mm
Spindle material constant	ξ	0.14	-
Additional friction torque	T_{fric}	$6.5 \cdot 10^{-3}$	Nm
Counterforce at minimum position of the actuator	F_{min}	0	Nm
Estimated mass moment of inertia of the system	I_{system}	$0.97 \cdot 10^{-5}$	kgm^2
Estimated effective torque of the cycle (simulation)	T_{RMS}	$46 \cdot 10^{-3}$	Nm
Temperature of the winding during the experiment	-	35	°C
Estimated mean copper losses of the simulation	$\overline{P}_{\text{Cu, sim}}$	5.6	W
Estimated mean copper losses of the measurement	$\overline{P}_{\text{Cu, meas}}$	5.6	W

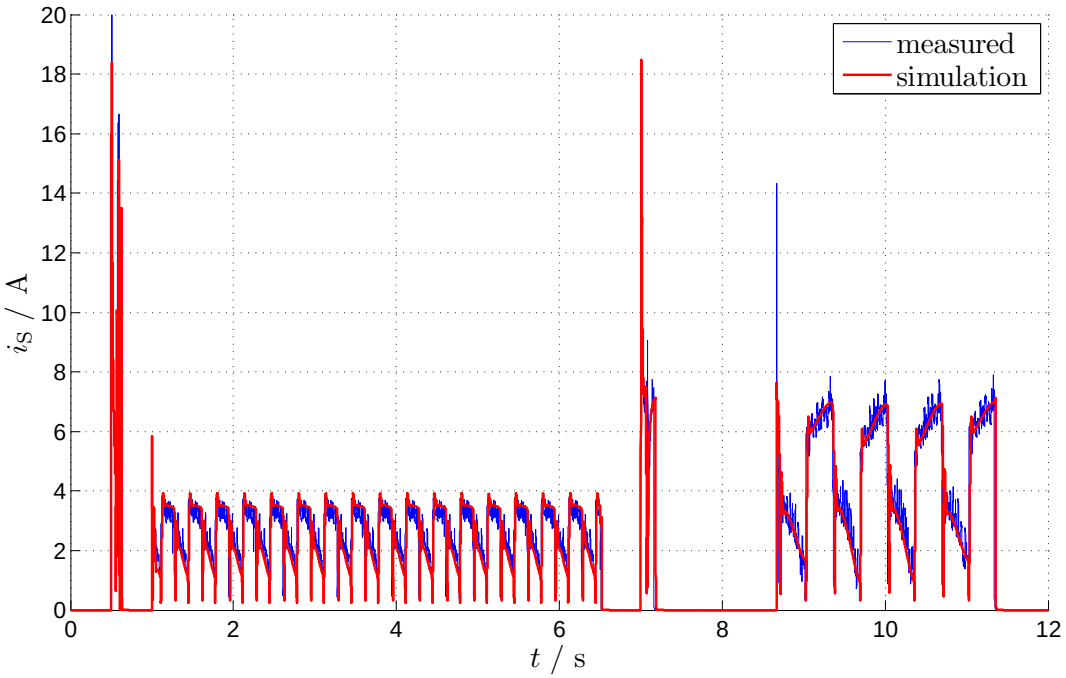

Figure 5.14: Comparison between measurement (blue) and simulation (red) of the stator current i_S as a function of time t of the actuator equipped with the SynRM to run through the cycle.

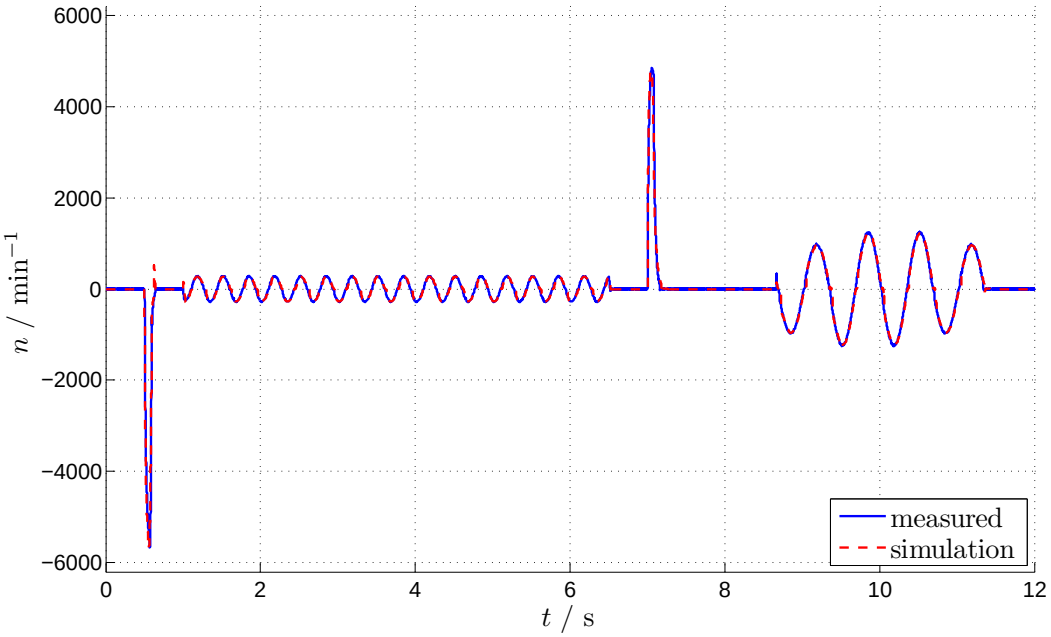

(a) Comparison between measurement (blue) and simulation (red) of the actuator's speed n as a function of time t.

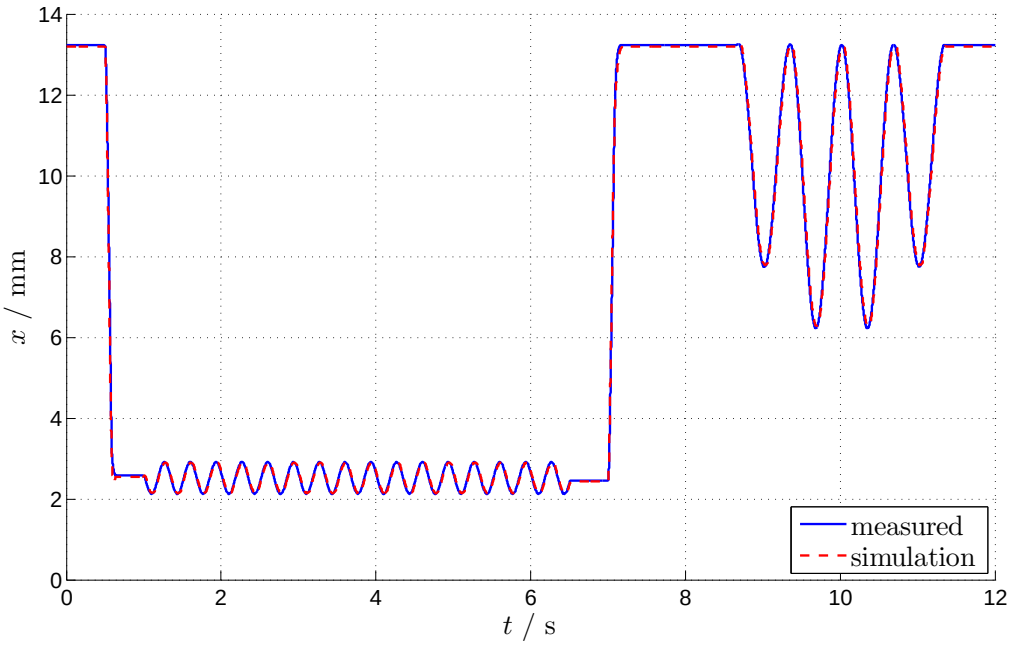

(b) Comparison between measurement (blue) and simulation (red) of the actuator's position x as a function of time t.

Figure 5.15: Comparison of measurement and simulation results of the actuator equipped with the SynRM to run through the cycle.

Chapter 6

Comparison of IM and SynRM

For the comparison of the IM and the SynRM, again, the specified cycle is used. However, the final application of the actuator demands to change its position within the defined adjusting range. Therefore, control strategies, such as reducing the IM's flux to zero during the resting times or limiting the torque of the machines to a certain level, might be applicable for the specific cycle, but not for the final application of the actuator.

6.1 Simulation

This Section compares the optimal machine designs of the IM and SynRM. Firstly, general aspects of the two machines designs are discussed. Subsequently, their dynamic behaviour is compared for two different load profiles.

- Slot-tooth layer of the stator
  Both machines have deep and wide slots (c.f. Figs. 4.3 and 4.5) to accommodate a lot of copper to keep the ohmic resistance of the stator winding and further copper losses as small as possible.

- Moment of inertia of the rotor
  The air gap diameters d_δ of the two machines are almost equal,

  $$\frac{d_{\delta,\,\mathrm{IM}}}{d_{\delta,\,\mathrm{SynRM}}} = \frac{0.54}{0.57} \approx 0.95 \quad ,$$

  but the moments of inertia differ considerably, because of the material removed for the flux barriers in the case of the SynRM,

  $$\frac{I_{\mathrm{IM}}}{I_{\mathrm{SynRM}}} = \frac{1.08 \cdot 10^{-5}}{0.62 \cdot 10^{-5}} \approx 1.74 \quad . \tag{6.1}$$

  As a result, the SynRM needs considerably less energy to accelerate and brake its rotor. This has a direct effect on the required torque and accordingly the copper losses.

- Controller design
  The controller forces the IM to operate with a constant rotor flux Ψ_R, which causes a flux producing current. In the extreme case that the machine does not have to produce any torque at all, the IM's controller would reduce the torque producing current i_Sq to zero. But i_Sd remains at its value and causes further losses of

  $$P_\mathrm{Cu} = \frac{3}{2} R_\mathrm{S}\, i_\mathrm{Sd}^2 \quad .$$

  In this situation, the SynRM's controller would reduce the stator current to zero, resulting in zero copper loss.

- Torque ripple
  For both machines, the numerically computed torque, T_{motor}, as a function of the azimuthal angle φ_{mech}, for constant speed and for an average torque of $\overline{T}_{\text{motor}} = 0.04\,\text{Nm}$, are shown in Fig. 6.1. Due to the rotor geometry of the SynRM, its torque ripple is significantly higher than that of the IM, what may lead to acoustic noise and vibrations. However, for the application motivating the work presented here, noise was considered to be of minor interest only.

During operation of the IM, the rotor flux is estimated using eq. (A.44), which depends on knowledge of the equivalent circuit parameters. This procedure is not necessary for the SynRM. Thus, the performance of the SynRM's controller depends to a smaller extent on the quality of the estimated equivalent circuit parameters than the IM's controller.

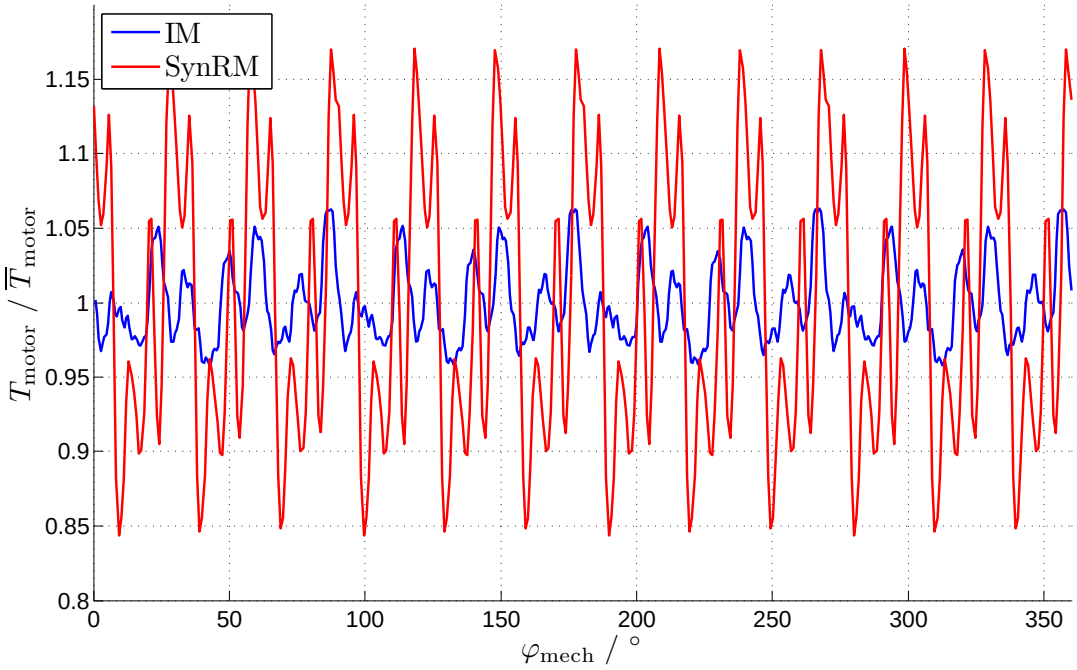

Figure 6.1: For both machines, the numerically computed torque, T_{motor}, as a function of the azimuthal angle φ_{mech}, for constant speed and for an average torque of $\overline{T}_{\text{motor}} = 0.04\,\text{Nm}$ using JMAG® [36]

.

6.1.1 Load profile: Specification

The first scenario is given by the specification of the application. Thus, the actuator has to run through the cycle shown in Fig. 1.2 with a load profile given by Table 1.2 and Fig. 1.5.

The load on the machine depends on the position of the actuator, but not on the direction of movement against or with the force of the spring. In particular, the machine has to produce a holding torque during the still standing phases of the cycle. The key parameters of the simulation are summarised in Table 6.1.

Fig. 6.2a shows the computed copper losses P_{Cu} as a function of time t for both machine types to run through the cycle within the tolerances given by Table 1.1.
During the complete cycle, the SynRM produces lower losses than the IM: The crucial difference occurs during the high dynamic phases, shown magnified in the right top hand corner of Fig. 6.2a. The SynRM needs less energy to accelerate its rotor up to the maximum rotational speed due to

1. its smaller torque of inertia and
2. that it can generate more torque than the IM.

This performance of the SynRM is exemplified in Fig. 6.2b for the step function response of position at $t = 7\,\mathrm{s}$ on the basis of the torque T_{motor} respectively the speed n (enlarged view). Thus, the SynRM accelerates faster, which in sum reduces the current requirement.

Table 6.1: Key parameters for the simulation according to the specifications, presented in Section 1.2.

Description	Symbol	Value	Unit
Maximum rotational speed	n_{max}	6000	min^{-1}
Maximum current of the power converter	I_{max}	50	A
Temperature of the winding	-	100	°C
Nominal rotor flux (IM)	Ψ_{R}	$9.5 \cdot 10^{-3}$	Vs
Estimated mean copper losses of the IM	$\overline{P}_{\mathrm{Cu,\,IM}}$	19.5	W
Estimated mean copper losses of the SynRM	$\overline{P}_{\mathrm{Cu,\,SynRM}}$	13.5	W

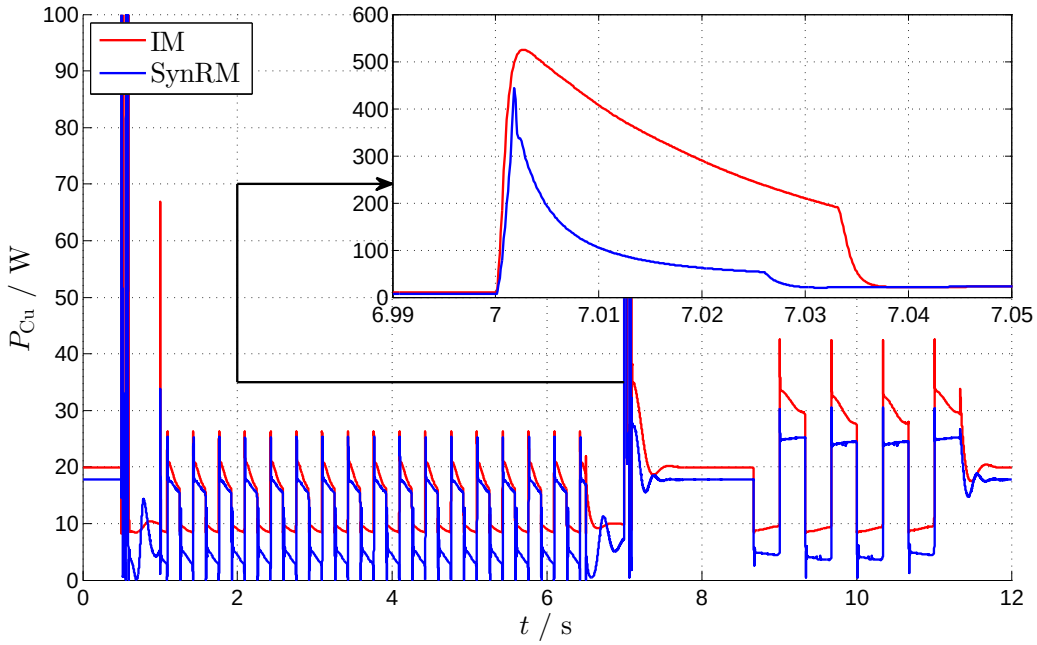

(a) Computed copper losses P_{Cu} vs. time t for the IM (red) and the SynRM (blue). The enlarged view in the right top hand corner shows the abrupt change of position at $t = 7\,\mathrm{s}$.

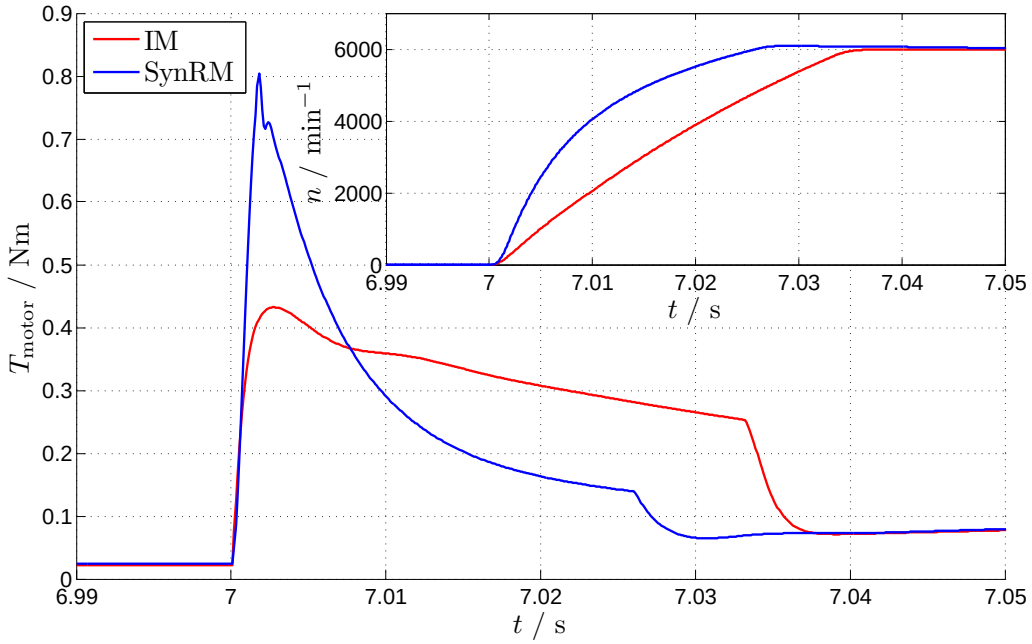

(b) Computed torque T_{motor} and speed n (enlarged view in the right top hand corner) for the step function response of position at $t = 7\,\mathrm{s}$ for the IM (red) and SynRM (blue).

Figure 6.2: Comparison of IM and SynRM for the load profile described in Section 6.1.1.

6.1.2 Load profile: Test bench

The realisation of the mechanical construction on the test bench differs in some points from the specification.

1. The load depends on the direction of rotation of the machine and is described by eqs. (5.2) and (5.3).
2. The mechanical components used for the actuator cause a self-locking system, which means, no holding torque is required to keep the actuator at a specific position.
3. The spring constant of the built-in spring differs considerably from the specifications. In order to compensate for this, the spring is not prestressed.

Again, the key parameters of the simulation are summarised in Table 6.2.

In contrast to the results presented in Section 6.1.1, the losses of both machine designs are remarkably reduced, due to the different load profile, c.f. Fig. 6.3. This mainly affects the SynRM, because its controller reduces the current to zero during the still standing times of the cycle.

Based on the simulation results, while considering the underlying specifications, preferences for this application could be given to the SynRM, due to a comparable dynamic performance and lower losses. This not only increases the efficiency of the actuator, but also leads to a smaller temperature increase. This, in turn, might eventually allow for a smaller design exploiting the thermal reserves.

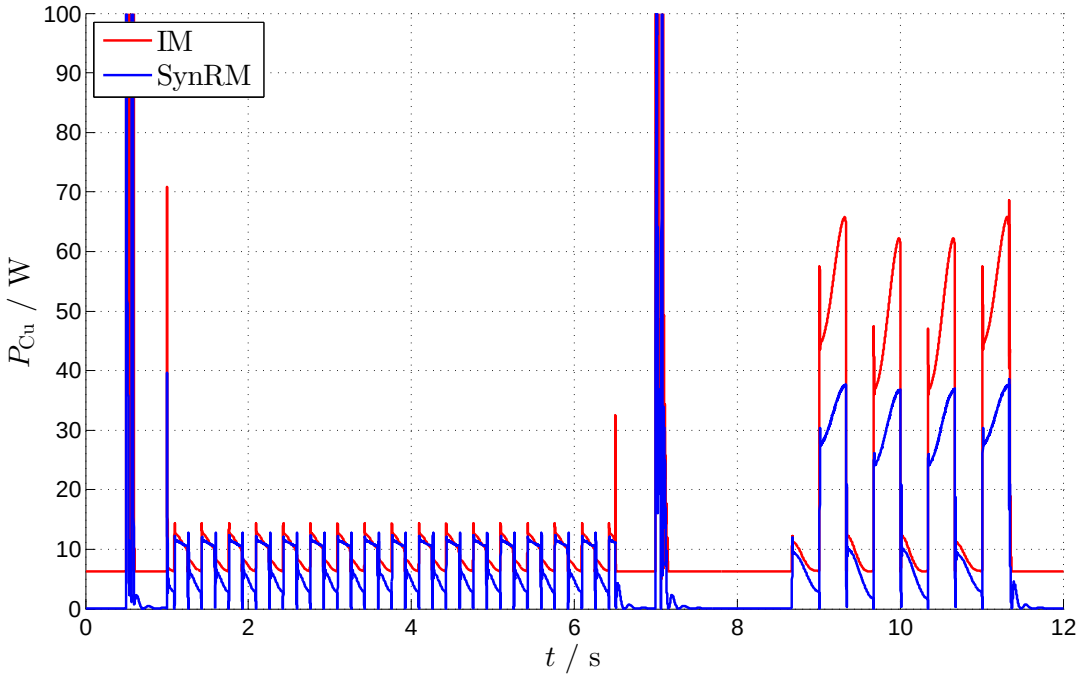

Figure 6.3: Copper losses P_{Cu} vs. time t for the IM (red) and the SynRM (blue) for the load profile described in Section 6.1.2.

Table 6.2: Key parameters for the simulation of the performance on the test bench.

Description	Symbol	Value	Unit
Maximum rotational speed	$n_{\max}$	6000	$\min^{-1}$
Maximum current of the power converter	$I_{\max}$	50	A
Temperature of the winding	-	100	°C
Spring constant	D_{spring}	17	N/mm
Diameter of the spindle	d_{spindle}	4.7	mm
Material constant of the spindle	ξ	0.125	-
Additional friction torque	T_{fric}	$13.5 \cdot 10^{-3}$	Nm
Counterforce at minimum position of the actuator	$F_{\min}$	0	Nm
Nominal rotor flux (IM)	Ψ_{R}	$8.5 \cdot 10^{-3}$	Vs
Estimated mean copper losses of the IM	$\overline{P}_{\text{Cu, IM}}$	16.5	W
Estimated mean copper losses of the SynRM	$\overline{P}_{\text{Cu, SynRM}}$	9.0	W

6.2 Results from the Test Bench

This Section discusses the dynamic and loss performance, based on measuring results of the two actuators as manufactured, equipped with an IM, respectively a SynRM, for an ambient temperature of $T_{\mathrm{amb}} = 20\,^{\circ}\mathrm{C}$.

1. Current space phasor i_{S}

   Fig. 6.5a shows i_{S} versus time t, required for the two machines to complete a cycle.

   The SynRM's controller reduces the stator current to zero during the resting phases of the cycle, as discussed in Section 6.1.2.

   For the step function response of the position, the IM builds up the current faster than the SynRM. But, the SynRM accelerates faster and therefore the periods requiring high currents are shorter than for the IM, as shown in the enlarged views of Figs. 6.5a and 6.5b.

2. Trajectory x

   Results of the actuators' positions as a function of time are shown in Fig. 6.5b. Both machines meet the specification within the given tolerances. Minor preferences concerning the position control deviation are attributed to the IM during the cycle's slow movement phases.

3. Temperature increase of the machines

   The temperature increase of the machines, shown in Fig. 6.4, was measured while repeatedly running through the cycle shown in Fig. D.1 in the Appendix. This cycle differs from the one given by the specifications and had to be used for the publications [72, 73] due to confidentiality. Its load profile is similar to the original cycle specified by a customer, shown in Fig. 1.2.

   Both measurements agree with the results of the rough thermal model, presented in Fig. 1.6. The steady state temperatures of the two machines, which are directly related to the losses, differ by approximately

   $$T_{\mathrm{winding,\,IM}} - T_{\mathrm{winding,\,SynRM}} \;\approx\; 15\,\mathrm{K} \quad . \tag{6.2}$$

   The thermal time constants τ_{therm} of the machines can be computed by applying the method of least squares to the measurement results of Fig. 6.4 and eq. (6.7). The calculation neglects the heat transfer through radiation[1] and considers that the copper losses increase with the temperature of the winding (eqs. (6.3) to (6.6)).

$$\frac{dT_{\mathrm{winding}}}{dt} = \frac{1}{C_{\mathrm{motor}}} \left[P_{\mathrm{Cu}}(T_{\mathrm{winding}}) - P_{\mathrm{therm}}(T_{\mathrm{winding}})\right] \tag{6.3}$$

$$P_{\mathrm{Cu}}(T_{\mathrm{winding}}) = P_{\mathrm{Cu},0} \left[1 + \alpha_{\mathrm{Cu},20} \left(T_{\mathrm{winding}}(t) - \underbrace{T_{\mathrm{winding}}(t=0)}_{T_0}\right)\right] \tag{6.4}$$

$$P_{\mathrm{therm}}(T_{\mathrm{winding}}) = k\,(T_{\mathrm{winding}} - T_{\mathrm{amb}}) \tag{6.5}$$

$$\frac{dT_{\mathrm{winding}}}{dt} = \frac{1}{C_{\mathrm{motor}}} \left[T_{\mathrm{winding}} \underbrace{(P_{\mathrm{Cu},0}\,\alpha_{\mathrm{Cu},20} - k)}_{a} + \underbrace{(P_{\mathrm{Cu},0} - P_{\mathrm{Cu},0}\,\alpha_{\mathrm{Cu},20}\,T_0 + k\,T_{\mathrm{amb}})}_{b}\right] \tag{6.6}$$

[1] Might be insignificant for an ambient temperature of $T_{\mathrm{amb}} = 20\,^{\circ}\mathrm{C}$.

In this context, $P_{\mathrm{Cu},0}$ denotes the copper losses of the machines for a winding temperature at the beginning of the measurement, k is a thermal constant, C_{motor} the heat capacity of the motor / actuator and P_{therm} the dissipated power. The solution of eq. (6.6) results in

$$T_{\mathrm{winding}}(t) = \left(T_0 + \frac{b}{a}\right) \exp\left(\frac{a}{C_{\mathrm{motor}}}\, t\right) - \frac{b}{a} = \left(T_0 + \frac{b}{a}\right) \exp\left(\frac{t}{\tau_{\mathrm{therm}}}\right) - \frac{b}{a} \quad . \tag{6.7}$$

The computation gives for the IM $\tau_{\mathrm{therm\,IM}} \approx 17\,\mathrm{min}$ and for the SynRM $\tau_{\mathrm{therm\,SynRM}} \approx 14\,\mathrm{min}$. To analyse the differences, a more detailed thermal modelling approach would be required what is beyond the scope of this work.

Based on the results, the actuator equipped with the SynRM might be the better choice for this application. However, it must be taken into account that two key parameters (k_{sff} and T_{fric}, see Table 6.3), which are directly related to the losses, are different from each other.

A comparison of the two manufactured rotors is shown in Fig. 6.6a, the actuator itself is depicted in Fig. 6.6b.

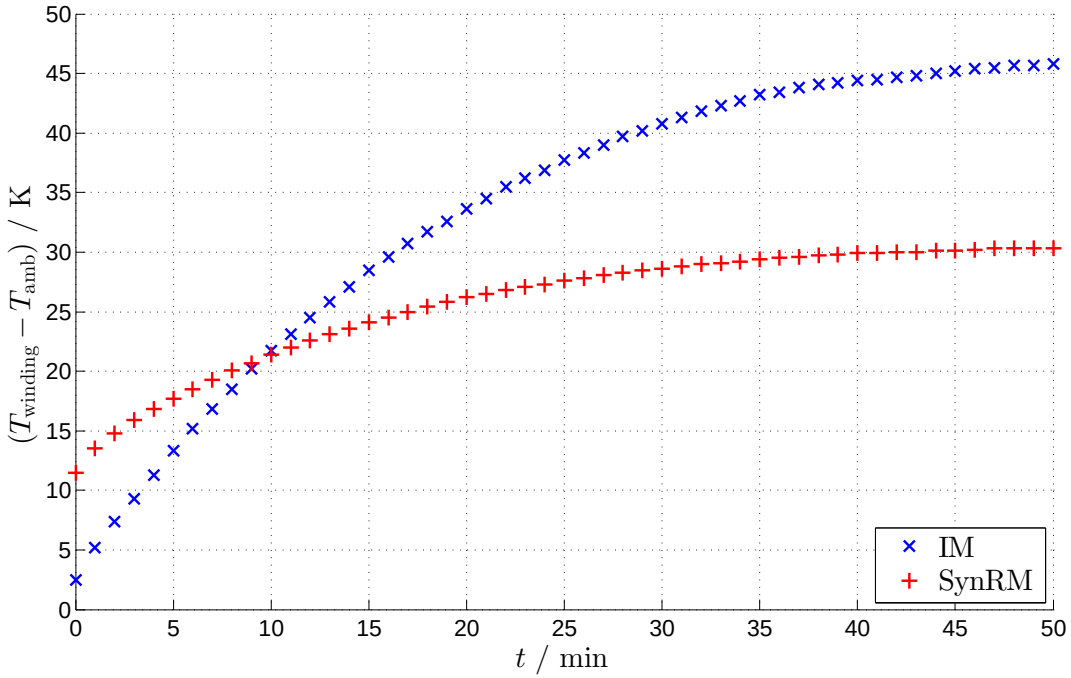

Figure 6.4: Measured temperature increase of the IM (blue ×) and SynRM (red +) as a function of time t for an ambient temperature of $T_{\mathrm{amb}} = 20\,^{\circ}\mathrm{C}$.
At $t = 0$ the actuator started repeatedly to run through the cycle. (The initial winding temperatures T_{winding} differ, due to previous measurements.)

Table 6.3: Exemplary parameters of the manufactured actuators.

Parameter	IM	SynRM
k_{sff}	0.41	0.36
δ / mm	0.16	0.20
T_{fric} / Nm $\cdot 10^{-3}$	13.5	6.5
ξ	0.13	0.14

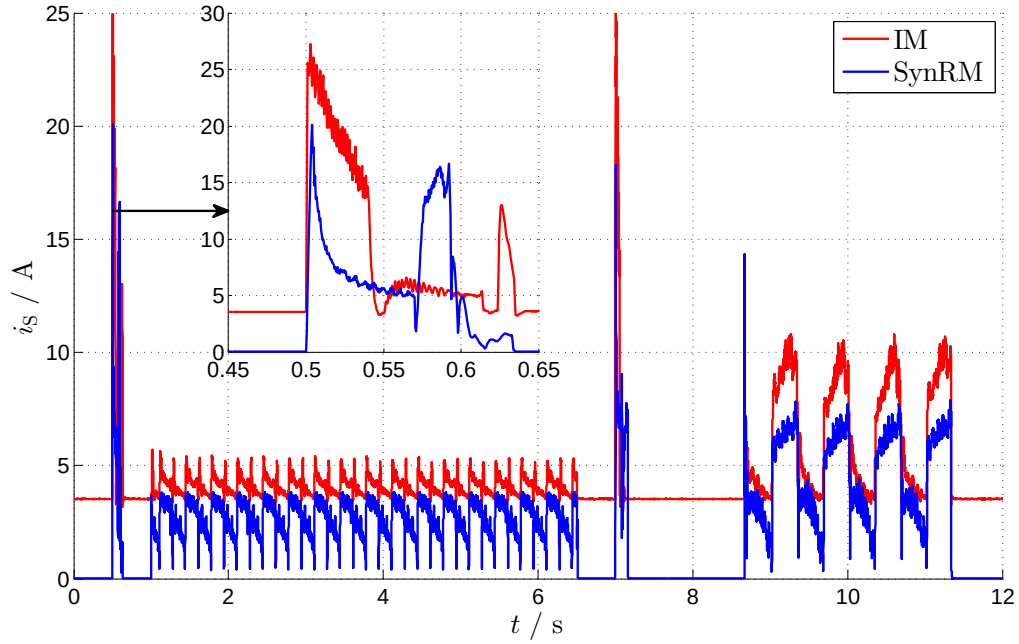

(a) Measured stator currents i_S for the IM (blue) and SynRM (red) to run through the cycle as a function of time t. The enlarged view at the top shows the abrupt change of position at $t = 0.5\,\mathrm{s}$.

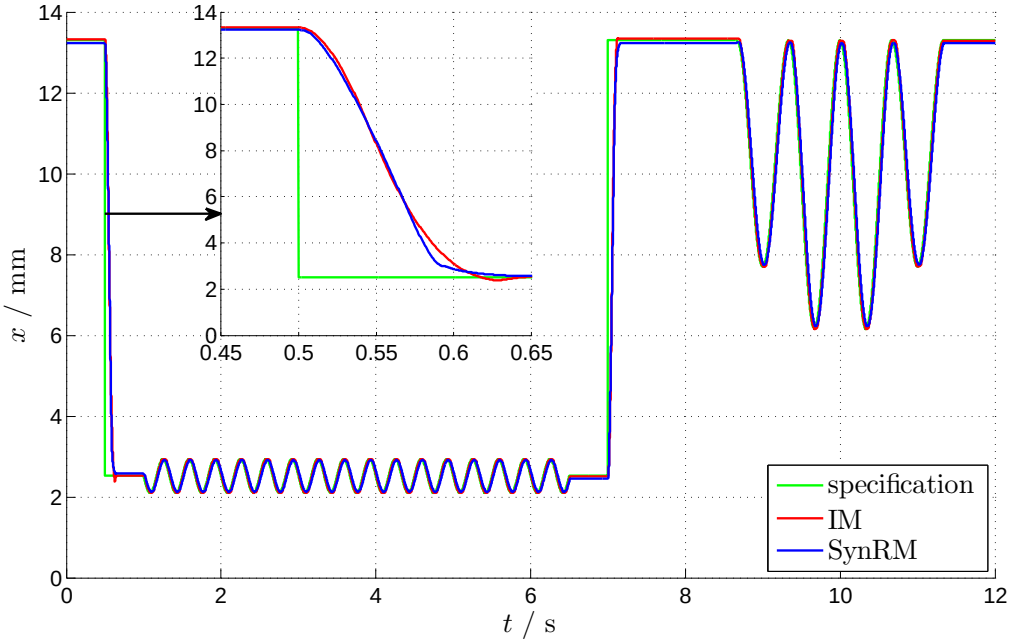

(b) Measured trajectories x of the IM (blue) and SynRM (red) to run through the cycle as a function of time t. The enlarged view at the top shows the abrupt change of position at $t = 0.5\,\mathrm{s}$. For comparison, the cycle as determined by the specification is plotted (green).

Figure 6.5: Comparison of measurement results for the actuator equipped with an IM respectively SynRM.

(a) Comparison of the two manufactured rotors (SynRM left and IM right).

(b) The actuator equipped with an IM, respectively a SynRM.

Figure 6.6: Pictures of the manufactured rotors (above) and the actuator (below).

6.3 Simulation using Results from the Test Bench

A comparison between measurement and simulation results of the two machines is presented in Section 5.2.4, respectively Section 5.3.3. Measurement results of the two actuators with respect to their dynamic performance and temperature increase are presented in Section 6.2, but the mechanical constants differ from each other.

This Section presents simulation results of the IM assuming the mechanical constants of the SynRMs actuator ($\xi = 0.14$ and $T_{\text{fric}} = 6.5 \cdot 10^{-3}\,\text{Nm}$), depicted in Fig. 6.7. The quintessence of this computation is that the losses and, certainly, the temperature increase of the machine decreases compared to the measurement results (Fig. 6.4), due to the smaller friction torque. But, based on the thermal model of Section 1.3, the temperature increase of the actuator equipped with the SynRM will still be lower.

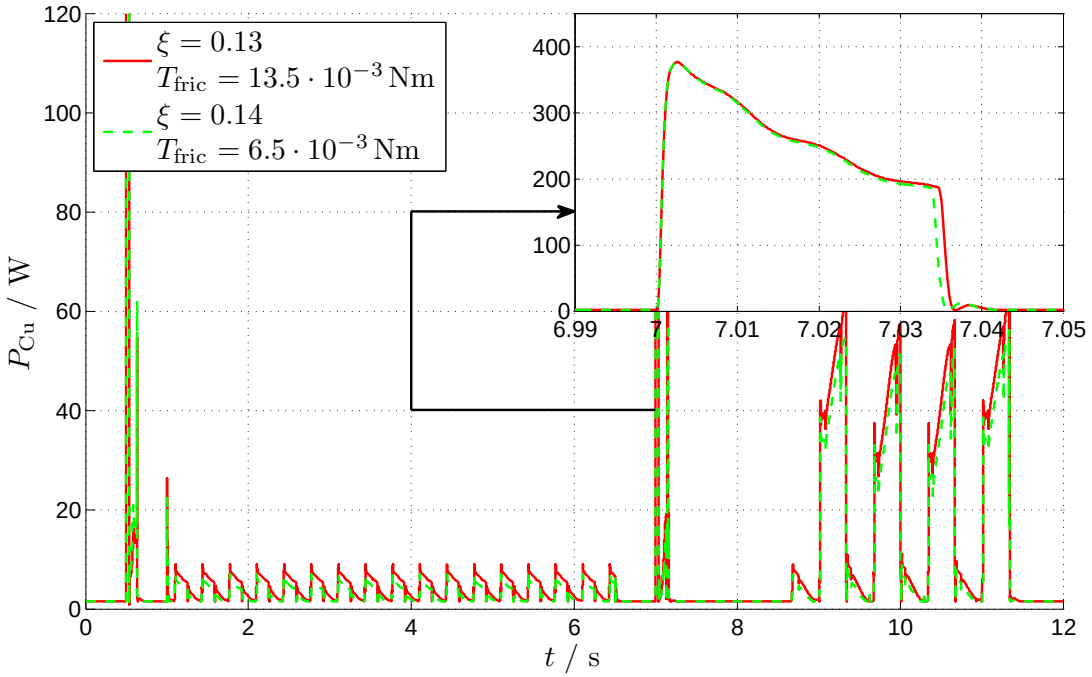

Figure 6.7: Computed copper losses P_{Cu} vs. time t for the IM using the mechanical parameters of the IMs actuator (red), respectively the SynRMs actuator (green dashed), c.f. Table 6.3. The enlarged view in the right top hand corner shows the abrupt change of position at $t = 7\,\text{s}$.

In contrast, the effect of the different slot fill factors on the machines' performances can be quantified relatively easily, because

$$P_{\text{Cu, SynRM}} \;=\; \frac{3}{2}\, R_{\text{S}}\, i_{\text{S}}^2 \;\propto\; k_{\text{sff}} \quad .$$

That means, a slot fill factor of 41 % instead of 36 % (c.f. Table 6.3) would reduce the SynRM's losses down to

$$\frac{36}{41} \;\approx\; 0.88 \quad ,$$

and thus, similarly the temperature increase, assuming the current requirement of the machine remains unchanged.

Chapter 7

Conclusion

In this work the design and analysis of IMs and SynRMs for a specific elevated-temperature actuator application is presented. PM based machines do not provide a viable option for the cost-sensitive application of interest here, because of their inherent temperature sensitivity, the related costs for additional, external cooling and the market uncertainty of rare-earth magnets.

Chapters 2 and 3

- Machine specific semi-analytical modelling approaches including a suitable controller design have been implemented in an optimisation algorithm to obtain a machine design, suitable for this sample case application.
- During the design process, the main dimensions of the machines were determined using a rough electro-magnetic approach and a thermal model of the actuator (Sections 2.1 and 1.3). The optimisation of the machines was performed within these predetermined limits, focussing on minimum losses. But the structure of implemented models of the two machines also enables this design method to be used for other boundary conditions.

Chapter 4

- The machine optimisation process and the final design results have been presented in Chapter 4.
- Differences occurred between the motors as manufactured and their computed designs:

  On the one hand, mechanical parameters of the machines and the actuator itself are influenced by the production. On the other hand, the magnetisation characteristic of the electrical steel sheets is particularly influenced by the degradation caused by laser cutting. This will notably affect small machines with small teeth and can have a great impact on the inductances of the machines.
- In a potential renewed design process these experiences have to be considered, if possible.

Chapters 5 and 6

- A comparison between simulations and measurements for the IM, respectively the SynRM, has been presented in Chapters 5 and 6. Both, simulation and measurement results show that the IM and SynRM are able to fulfil the requirements determined by the specifications.

- It is of particular interest for this application to operate the IM at the optimal nominal value of the rotor flux, because copper losses during the driving cycle are highly affected by this value. Therefore, an accurate knowledge of the equivalent circuit parameters of the IM is required. For the SynRM no flux controller is needed. Thus, the performance of the SynRM's controller is less sensitive to the accuracy of the estimated equivalent circuit parameters than the IM's controller.

- In the extreme case that the machine is not required to produce any torque at all, the SynRM's controller reduces the stator current to zero, resulting in zero copper losses. In contrast, the IM operates with a constant rotor flux, which requires a flux-producing current causing copper losses for this situation.

Further Remarks

For the given application and using the control techniques as implemented (constant flux for the IM and variable flux for the SynRM), the IM is slightly preferable with respect to dynamic behaviour and the position control deviation. However, the measured temperature increase indicates lower losses for the SynRM which would allow operation at even higher ambient temperature. Since both characteristics - loss and dynamic behaviour - are influenced by the control strategy, further research on control optimisation might allow to expand the respective capabilities of the machines. However, this was beyond the scope of this work, where rather established control techniques had to be chosen for reasons of cost.

Appendix A

Induction Machine Theory - Derivations

A.1 Fundamental Torque Relationship

A relationship between the resistive losses and the produced torque of the induction motor is deduced, according to [37, Chapter 6 and 7].

The copper losses P_{Cu} in the stator of an induction motor are given by

$$P_{\mathrm{Cu}} \;=\; m\, I_{\mathrm{Ph}}^2\, R_{\mathrm{Ph}} \quad , \tag{A.1}$$

which can also be expressed as a function of the current density J_{RMS},

$$\begin{aligned} P_{\mathrm{Cu}} \;&= m\,(J_{\mathrm{RMS}}\, A_{\mathrm{C}})^2\, \frac{\rho_{\mathrm{Cu}}\, l_{\mathrm{Cu}}}{A_{\mathrm{C}}}\, w_{\mathrm{str}} \;=\; m\, J_{\mathrm{RMS}}^2\, \rho_{\mathrm{Cu}}\, l_{\mathrm{Cu}}\, A_{\mathrm{slot}}\, k_{\mathrm{sff}}\, \frac{w_{\mathrm{str}}}{w_{\mathrm{slot}}} \\ &= m\, J_{\mathrm{RMS}}^2\, \rho_{\mathrm{Cu}}\, l_{\mathrm{Cu}}\, A_{\mathrm{slot}}\, k_{\mathrm{sff}}\, \frac{N_{\mathrm{S}}}{2\,m} \;=\; J_{\mathrm{RMS}}^2\, \rho_{\mathrm{Cu}}\, \frac{l_{\mathrm{Cu}}}{2}\, A_{\mathrm{Cu}} \quad . \end{aligned}$$

Thus, the maximum current density (rms-value), given specific permitted losses, decreases with the volume of copper in the stator

$$J_{\mathrm{RMS}} \;=\; \sqrt{\frac{2\, P_{\mathrm{Cu}}}{\rho_{\mathrm{Cu}}\, A_{\mathrm{Cu}}\, l_{\mathrm{Cu}}}} \quad . \tag{A.2}$$

The same approach can also be applied to the rotor.

As already mentioned in Section 1.2.2 for this application of the induction motor, iron losses can be neglected in good approximation.

Suppose the current densities of the rotor and stator are known, the current sheet A is given by

$$A \;=\; \frac{A_{\mathrm{Cu}}\, J_{\mathrm{RMS}}}{d_\delta\, \pi} \quad . \tag{A.3}$$

In eq. (A.3), the linear current density is an effective value of a space phasor and a sinusoidal distribution at the circumference of the air gap diameter[1] is assumed.

$$A\,(\alpha) \;=\; \underbrace{\sqrt{2}\, A}_{\hat{A}}\, \sin(p\,\alpha)$$

[1] For simplicity, $d_\delta \;\approx\; d_{\mathrm{SI}} \;\approx\; d_{\mathrm{RO}}$ is used in the following.

Applying Ampère's law, as deduced in [37, Chapter 7.1.1], the current linkage results in

$$\Theta(\alpha) = \int A(\alpha)\frac{d_\delta}{2}\,d\alpha' = \underbrace{-\frac{\hat{A}\,d_\delta}{2\,p}}_{\hat{\Theta}}\cos(p\,\alpha) \quad .$$

Considering normal load conditions both, the stator and the rotor, are current-carrying, which causes a current linkage from each of the two and accordingly an air-gap flux density B_δ. But, only if a linear magnetic characteristic is assumed for the machine, the flux densities of stator and rotor can be superposed,

$$\hat{B}_\delta = \frac{\mu_0}{\delta_{\text{eff}}}\hat{\Theta} \quad . \tag{A.4}$$

The effective air gap length δ_{eff}, used in eq. (A.4), is defined as follows

$$\sum_{\text{i}\,\in\,\text{iron parts}} H_\text{i}\,l_\text{i} + H_\delta\,\delta = H_\delta\,\delta_{\text{eff}} \quad ,$$

describes the system if there was no magnetic voltage drop in the iron and combines all magnetic drops to the air gap. In other words, δ_{eff} describes the length that would be required to produce the same voltage drop of the magnetomotive force in a machine with infinite permeability in the iron parts.

Furthermore, δ_{eff} exclusively depends on geometric properties, if linear magnetic properties ($\mu_\text{r} = \text{const.}$) are assumed, as shown in Section A.2.

The current sheet

$$A(x) = \hat{A}\sin\left(\frac{x\,\pi}{\tau_\text{p}} + \psi\right)$$

and the air gap flux density

$$B_\delta(x) = \hat{B}_\delta\sin\left(\frac{x\,\pi}{\tau_\text{p}}\right)$$

cause the torque

$$T = p\,d_\delta\,l_{\text{Fe}}\int_0^{\tau_\text{p}} A(x)\,B_\delta(x)\,dx \quad , \tag{A.5}$$

according to [54, eq. (4.7-1)], where ψ defines the phase angle between the current sheet and the air gap flux density, which depends on the angle of the rotor current.

Using a trigonometric relation[2], eq. (A.5) results in

$$\begin{aligned} T &= p\,d_\delta\,l_{\text{Fe}}\,\hat{A}\,\hat{B}_\delta\int_0^{\tau_\text{p}}\sin^2\left(\frac{x\,\pi}{\tau_\text{p}}\right)\cos(\psi) + \underbrace{\sin\left(\frac{x\,\pi}{\tau_\text{p}}\right)\cos\left(\frac{x\,\pi}{\tau_\text{p}}\right)\sin(\psi)}_{=0}\,dx \\ &= p\,d_\delta\,l_{\text{Fe}}\,\hat{A}\,\hat{B}_\delta\cos(\psi)\,\frac{\tau_\text{p}}{2\,\pi}\underbrace{\left[\frac{x\,\pi}{\tau_\text{p}} - \sin\left(\frac{x\,\pi}{\tau_\text{p}}\right)\cos\left(\frac{x\,\pi}{\tau_\text{p}}\right)\right]\Bigg|_0^{\tau_\text{p}}}_{\pi} \\ &= p\,d_\delta\,l_{\text{Fe}}\,\hat{A}\,\hat{B}_\delta\cos(\psi)\,\frac{\pi}{2\,\pi}\,\frac{d_\delta\,\pi}{2p} = \hat{A}\,\hat{B}_\delta\,d_\delta^2\,l_{\text{Fe}}\,\frac{\pi}{4}\cos(\psi) \quad . \end{aligned}$$

[2] $\sin(a+b) = \sin(a)\cos(b) + \cos(a)\sin(b)$

That means, within this model, the torque of the induction machine is constant in time and increases linearly with its active length and with the square of the air gap diameter. Because of this, a short machine should be favoured if the volume of the machine is the limiting factor of the design process. But, for a short machine, the end windings would cause a disproportionately high portion of copper losses.

Since the current sheet

$$\hat{A} \propto \frac{A_{\mathrm{Cu}}\, J_{\mathrm{RMS}}}{d_\delta\, \pi} \propto \sqrt{\frac{2\, P_{\mathrm{Cu}}}{\rho_{\mathrm{Cu}}\, A_{\mathrm{Cu}}\, l_{\mathrm{Cu}}}} \propto \sqrt{P_{\mathrm{Cu}}}$$

and the air gap flux density

$$\hat{B}_\delta \propto \frac{\mu_0}{\delta_{\mathrm{eff}}}\,\hat{\Theta} \propto \frac{\hat{A}\, d_\delta}{2\, p} \propto \frac{A_{\mathrm{Cu}}\, J_{\mathrm{RMS}}}{d_\delta\, \pi} \propto \sqrt{\frac{2\, P_{\mathrm{Cu}}}{\rho_{\mathrm{Cu}}\, A_{\mathrm{Cu}}\, l_{\mathrm{Cu}}}} \propto \sqrt{P_{\mathrm{Cu}}} \quad ,$$

the torque and the copper loss are proportional.

$$T_{\mathrm{motor}} \propto \hat{A}\, \hat{B}_\delta \propto P_{\mathrm{Cu}} \tag{A.6}$$

A.2 Linear Magnet Circuit

The assumption of linear magnetic properties of the laminations is acceptable as long as the machine is not saturated. The derivation results in an expression for the effective air gap length δ_{eff}, defined in Section A.1.

The peak magnetic voltage $\hat{U}_{\mathrm{p}}$ for one pole pair of the machine is obtained from Ampère's law. This task can be simplified by dividing the machine into different regions (air gap, yoke and teeth for stator and rotor), which are analysed separately for the peak value of the magnetic flux density of the air gap $\hat{B}_\delta$. Due to symmetry, it is sufficient to only treat one pole.

$$\hat{U}_{\mathrm{p}} \approx \sum_i \int H_{\mathrm{i}}\, dl_{\mathrm{i}} = \sum_i \hat{U}_{\mathrm{i}} = 2\left(\hat{U}_\delta + \hat{U}_{\mathrm{ST}} + \hat{U}_{\mathrm{RT}} + \frac{1}{2}\,\hat{U}_{\mathrm{SJ}} + \frac{1}{2}\,\hat{U}_{\mathrm{RJ}}\right) \tag{A.7}$$

In the following, the calculation of the magnetic voltage for the different regions of the induction motor is described in more detail.

- Air gap region

  The magnetic voltage over the air gap is calculated from the length of the physical air gap δ and the flux reduction due to the slot openings. This is achieved by introducing the Carter factor [74].

  The Carter factor k_{C} considers that due to the slotting of the machine on average the air gap seems to be longer than it physically is. According to Carter's principle, the Carter factor has to be calculated separately for stator and rotor and their product yields the Carter factor of the air gap.

  Thus, $\hat{U}_\delta$ results in:

$$\hat{U}_\delta = \frac{\delta\, k_{\mathrm{C}}}{\mu_0}\,\hat{B}_\delta \tag{A.8}$$

- Slot tooth region

  Instead of the whole slot tooth region, for simplification, only one slot pitch is considered. Furthermore, it is assumed that the complete magnetic flux entering the slot pitch is forced into the tooth. According to this, the magnetic flux density in the tooth increases by the ratio of slot pitch and tooth width compared to the flux density in the air gap.

  Thus, the magnetic voltages for the stator and the rotor slot tooth regions result in

$$\hat{U}_{\mathrm{ST}} = \frac{h_{\mathrm{ST}}}{\mu_0\,\mu_{\mathrm{r}}}\,\frac{\tau_{\mathrm{SSP}}}{a_{\mathrm{S}}}\,\hat{B}_\delta \qquad \text{and} \qquad \hat{U}_{\mathrm{RT}} = \frac{h_{\mathrm{RT}}}{\mu_0\,\mu_{\mathrm{r}}}\,\frac{\tau_{\mathrm{RSP}}}{a_{\mathrm{R}}}\,\hat{B}_\delta \quad . \tag{A.9}$$

  As long as the teeth of the machine are not saturated the above mentioned assumption works fine, but a more detailed model has to consider that a certain part of the magnetic flux will also flow across the slot.

- Yoke region

  The magnetic flux of the machine per pole is defined by

$$\Phi_{\mathrm{p}} = \frac{2}{\pi}\,\hat{B}_\delta\,\tau_{\mathrm{p}}\,l_{\mathrm{Fe}} \quad . \tag{A.10}$$

  In eq. (A.10), the factor $2/\pi$ arises from a sinusoidally assumed flux density $\hat{B}_\delta$ averaged over one pole pitch τ_{p}.
  In the yoke region Φ_{p} splits into two equal parts,

$$\Phi_{\mathrm{J}} = 1/2\,\Phi_{\mathrm{p}} \quad . \tag{A.11}$$

  The flux density in the yoke region is assumed constant and depends on the cross sectional area of the yoke. Using eqs. (A.10) and (A.11) the magnetic voltages for the stator and the rotor yoke regions are given by

$$\hat{U}_{\mathrm{SJ}} = \frac{l_{\mathrm{SHJ}}}{\mu_0\,\mu_{\mathrm{r}}\,\pi}\,\frac{\tau_{\mathrm{p}}}{h_{\mathrm{SJ}}}\hat{B}_\delta \qquad \text{and} \qquad \hat{U}_{\mathrm{RJ}} = \frac{l_{\mathrm{RHJ}}}{\mu_0\,\mu_{\mathrm{r}}\,\pi}\,\frac{\tau_{\mathrm{p}}}{h_{\mathrm{RJ}}}\hat{B}_\delta \quad . \tag{A.12}$$

Combining eqs. (A.7) to (A.9) and (A.12) gives an expression for the effective air gap length according to [37, eq. (3.56)],

$$\delta_{\mathrm{eff}} = \frac{\hat{U}_\delta + \hat{U}_{\mathrm{ST}} + \hat{U}_{\mathrm{RT}} + \frac{1}{2}\,\hat{U}_{\mathrm{SJ}} + \frac{1}{2}\,\hat{U}_{\mathrm{RJ}}}{\hat{U}_\delta}\,k_{\mathrm{C}}\,\delta \quad . \tag{A.13}$$

A.3 Derivation of the Equivalent Circuit

The equivalent circuit of the induction motor is derived [75, Chapter 5], starting with the differential equations for the stator and rotor voltage circuit.

$$u_{\mathrm{S}}^{\mathrm{S}} = R_{\mathrm{S}}\,i_{\mathrm{S}}^{\mathrm{S}} + \frac{d}{dt}\,\Psi_{\mathrm{S}}^{\mathrm{S}} \qquad \text{(stator circuit)} \tag{A.14}$$

$$0 = u_{\mathrm{R}}^{\mathrm{R}} = R_{\mathrm{R}}\,i_{\mathrm{R}}^{\mathrm{R}} + \frac{d}{dt}\,\Psi_{\mathrm{R}}^{\mathrm{R}} \qquad \text{(rotor circuit)} \tag{A.15}$$

$$\Psi_{\mathrm{S}}^{\mathrm{S}} = L_{\mathrm{S}}\,i_{\mathrm{S}}^{\mathrm{S}} + M\,i_{\mathrm{R}}^{\mathrm{S}} \qquad \text{(stator circuit)} \tag{A.16}$$

$$\Psi_{\mathrm{R}}^{\mathrm{R}} = M\,i_{\mathrm{S}}^{\mathrm{R}} + L_{\mathrm{R}}\,i_{\mathrm{R}}^{\mathrm{R}} \qquad \text{(rotor circuit)} \tag{A.17}$$

The meanings of the superscripts and subscripts are as follows:

- Superscript: denotes in which coordinate system the variable is defined. (S ...stator, R ...rotor)
- Subscript: denotes either a variable of the stator (S) or of the rotor circuit (R).

In eq. (A.15), the rotor voltage u_R is set to zero, because only the special case of a squirrel-cage motor is treated in this derivation, which is performed in two steps.

1. Transformation of the rotor variables to the stator (Section A.3.1).
2. Transformation of eq. (A.15) to the stator fixed coordinate system (Section A.3.2).

A.3.1 Transformation of the Rotor Variables to the Stator

This transformation is based on three conditions [76, 75, 54], concerning the transformed rotor current i'_R[3]:

1. i'_R has to cause the same current linkage as i_R.

$$\begin{aligned} \Theta^\mathrm{S}_\mu &= \Theta^\mathrm{S}_\mathrm{S} + \Theta^\mathrm{S}_\mathrm{R} \\ \frac{3}{2}\, w_\mathrm{S}\, i^\mathrm{S}_\mu &= \frac{3}{2}\, w_\mathrm{S}\, i^\mathrm{S}_\mathrm{S} + \frac{3}{2}\, w_\mathrm{R}\, i^\mathrm{S}_\mathrm{R} \\ i^\mathrm{S}_\mu &= i^\mathrm{S}_\mathrm{S} + \frac{w_\mathrm{R}}{w_\mathrm{S}}\, i^\mathrm{S}_\mathrm{R} \end{aligned}$$

   In this case, w_S and w_R represent the number of turns in series of the winding of the stator and the rotor.

$$i'_\mathrm{R} = \frac{w_\mathrm{R}}{w_\mathrm{S}}\, i_\mathrm{R} \tag{A.18}$$

2. i'_R and i_S should flow across the same main inductance L_h, defined as

$$\Psi_\mathrm{h} = i_\mu\, L_\mathrm{h} \quad . \tag{A.19}$$

   Starting with eq. (A.17) and considering the relations, $M \propto w_\mathrm{S}\, w_\mathrm{R}$, $L_\mathrm{Sh} \propto w_\mathrm{S}^2$ and $L_\mathrm{Rh} \propto w_\mathrm{R}^2$, M and L_Rh can be expressed in terms of L_Sh.

$$\begin{aligned} \Psi^\mathrm{R}_\mathrm{R} &= L_\mathrm{Sh}\, \frac{w_\mathrm{R}}{w_\mathrm{S}}\, i^\mathrm{R}_\mathrm{S} + L_\mathrm{Sh} \left(\frac{w_\mathrm{R}}{w_\mathrm{S}}\right)^2 i^\mathrm{R}_\mathrm{R} + L_{\mathrm{R}\sigma}\, i^\mathrm{R}_\mathrm{R} \\ \frac{w_\mathrm{S}}{w_\mathrm{R}}\, \Psi^\mathrm{R}_\mathrm{R} &= L_\mathrm{Sh}\, i^\mathrm{R}_\mathrm{S} + L_\mathrm{Sh}\, \frac{w_\mathrm{R}}{w_\mathrm{S}}\, i^\mathrm{R}_\mathrm{R} + L_{\mathrm{R}\sigma}\, \frac{w_\mathrm{S}}{w_\mathrm{R}}\, i^\mathrm{R}_\mathrm{R} \\ \underbrace{\frac{w_\mathrm{S}}{w_\mathrm{R}}\, \Psi^\mathrm{R}_\mathrm{R}}_{\Psi^{\mathrm{R}\,\prime}_\mathrm{R}} &= L_\mathrm{Sh}\, i^\mathrm{R}_\mathrm{S} + L_\mathrm{Sh}\, \frac{w_\mathrm{R}}{w_\mathrm{S}}\, \frac{w_\mathrm{S}}{w_\mathrm{R}}\, i^{\mathrm{R}\,\prime}_\mathrm{R} + \underbrace{L_{\mathrm{R}\sigma} \left(\frac{w_\mathrm{S}}{w_\mathrm{R}}\right)^2}_{L'_{\mathrm{R}\sigma}} i^{\mathrm{R}\,\prime}_\mathrm{R} \end{aligned}$$

   Renaming L_Sh to L_h leads to

$$\Psi^{\mathrm{R}\,\prime}_\mathrm{R} = L_\mathrm{h}\, i^\mathrm{R}_\mathrm{S} + L_\mathrm{h}\, i^{\mathrm{R}\,\prime}_\mathrm{R} + L'_{\mathrm{R}\sigma} i^{\mathrm{R}\,\prime}_\mathrm{R} = L_\mathrm{h} i^\mathrm{R}_\mu + L'_{\mathrm{R}\sigma} i^{\mathrm{R}\,\prime}_\mathrm{R} = \Psi^\mathrm{R}_\mathrm{h} + L'_{\mathrm{R}\sigma} i^{\mathrm{R}\,\prime}_\mathrm{R} \quad . \tag{A.20}$$

[3] Transformed variables are marked with an apostrophe.

3. i'_R has to cause the same ohmic loss as i_R.

$$R_\mathrm{R}\, i_\mathrm{R}^2 \stackrel{!}{=} R'_\mathrm{R}\, {i'_\mathrm{R}}^2 = R'_\mathrm{R} \left(\frac{w_\mathrm{R}}{w_\mathrm{S}}\, i_\mathrm{R}\right)^2 \quad \Rightarrow \quad R'_\mathrm{R} = \left(\frac{w_\mathrm{S}}{w_\mathrm{R}}\right)^2 R_\mathrm{R} \tag{A.21}$$

In conclusion, eqs. (A.14) to (A.17) result in:

$$u_\mathrm{S}^\mathrm{S} = R_\mathrm{S}\, i_\mathrm{S}^\mathrm{S} + \frac{d}{dt}\Psi_\mathrm{S}^\mathrm{S} \tag{A.22}$$

$$0 = R'_\mathrm{R}\, i_\mathrm{R}^{\mathrm{R}\,\prime} + \frac{d}{dt}\Psi_\mathrm{R}^{\mathrm{R}\,\prime} \tag{A.23}$$

$$\Psi_\mathrm{S}^\mathrm{S} = (L_\mathrm{h} + L_{\mathrm{S}\sigma})\, i_\mathrm{S}^\mathrm{S} + L_\mathrm{h}\, i_\mathrm{R}^{\mathrm{S}\,\prime} \tag{A.24}$$

$$\Psi_\mathrm{R}^{\mathrm{R}\,\prime} = L_\mathrm{h}\, i_\mathrm{S}^\mathrm{R} + (L_\mathrm{h} + L'_{\mathrm{R}\sigma})\, i_\mathrm{R}^{\mathrm{R}\,\prime} \tag{A.25}$$

In the following, the apostrophe, marking variables, which are transformed from the rotor to the stator, is omitted for simplification.

A.3.2 Transforming the Rotor Differential Equation to the Stator Fixed Coordinate System

In general, the relation of a variable Z, once expressed in the coordinate system fixed to the stator and once in a rotating coordinate system fixed to the rotor, is given by

$$Z^\mathrm{R} = Z^\mathrm{S}\, \mathrm{e}^{-\mathrm{i}\,\varphi} \quad , \tag{A.26}$$

according to Fig. A.1. Transforming eq. (A.23), using eq. (A.26) results in

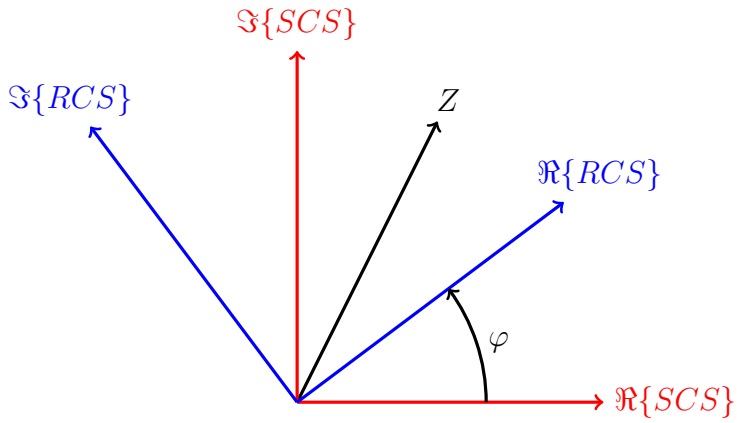

Figure A.1: Illustration of the transformation (eq. (A.26)) from the stator fixed (SCS) to the rotor fixed coordinate system (RCS).

$$0 = R_\mathrm{R}\, i_\mathrm{R}^\mathrm{S}\, \mathrm{e}^{-\mathrm{i}\,\varphi} + \frac{d}{dt}\left(\Psi_\mathrm{R}^\mathrm{S}\, \mathrm{e}^{-\mathrm{i}\,\varphi}\right) = R_\mathrm{R}\, i_\mathrm{R}^\mathrm{S} - \mathrm{i}\, \underbrace{\frac{d\varphi}{dt}}_{\omega_\mathrm{mech}} \Psi_\mathrm{R}^\mathrm{S} + \dot{\Psi}_\mathrm{R}^\mathrm{S} \quad .$$

Consequently, the differential equations, describing the induction machine in the stator fixed coordinate system, are given by

$$\dot{\Psi}_\mathrm{S}^\mathrm{S} = u_\mathrm{S}^\mathrm{S} - R_\mathrm{S}\, i_\mathrm{S}^\mathrm{S} \quad \text{and} \quad \dot{\Psi}_\mathrm{R}^\mathrm{S} = \mathrm{i}\,\omega_\mathrm{mech}\, \Psi_\mathrm{R}^\mathrm{S} - R_\mathrm{R}\, i_\mathrm{R}^\mathrm{S} \quad . \tag{A.27}$$

In a simulation program this coordinate system allows to consider the non-linearity of the main inductance in a very simple way. A transformation of eqs. (A.24) and (A.25) leads to

$$\frac{\Psi_{\mathrm{S}}^{\mathrm{S}}}{L_{\mathrm{S}\sigma}} = i_{\mathrm{S}}^{\mathrm{S}} + \frac{\Psi_{\mathrm{h}}^{\mathrm{S}}}{L_{\mathrm{S}\sigma}} \quad \text{and} \quad \frac{\Psi_{\mathrm{R}}^{\mathrm{S}}}{L_{\mathrm{R}\sigma}} = i_{\mathrm{R}}^{\mathrm{S}} + \frac{\Psi_{\mathrm{h}}^{\mathrm{S}}}{L_{\mathrm{R}\sigma}} \quad .$$

The sum of these two equations results in

$$\frac{\Psi_{\mathrm{S}}^{\mathrm{S}}}{L_{\mathrm{S}\sigma}} + \frac{\Psi_{\mathrm{R}}^{\mathrm{S}}}{L_{\mathrm{R}\sigma}} = \underbrace{\left(i_{\mathrm{S}}^{\mathrm{S}} + i_{\mathrm{R}}^{\mathrm{S}}\right)}_{i_{\mu}^{\mathrm{S}}} + \left(\frac{1}{L_{\mathrm{S}\sigma}} + \frac{1}{L_{\mathrm{R}\sigma}}\right) \Psi_{\mathrm{h}}^{\mathrm{S}} \overset{\Psi_{\mathrm{h}}^{\mathrm{S}} = L_{\mathrm{h}}\, i_{\mu}^{\mathrm{S}}}{=} \left(\frac{1}{L_{\mathrm{S}\sigma}} + \frac{1}{L_{\mathrm{h}}} + \frac{1}{L_{\mathrm{R}\sigma}}\right) \Psi_{\mathrm{h}}^{\mathrm{S}} \quad . \tag{A.28}$$

The left side of eq. (A.28) is the sum of the integrated eq. (A.27), the right hand could be provided in a look-up table, which allows to compute Ψ_{h} and further the torque

$$T_{\mathrm{motor}} = \frac{3}{2}\, p\, \Im\left\{\Psi_{\mathrm{h}}^{\mathrm{S}}\, i_{\mathrm{S}}^{\mathrm{S}\,*}\right\} \quad . \tag{A.29}$$

For steady state,

$$\frac{d\varphi}{dt} = \omega_{\mathrm{mech}} = \text{const.} \quad \text{and} \quad u_{\mathrm{S}} = \hat{U}_{\mathrm{S}}\, \mathrm{e}^{\mathrm{i}\,\omega_{\mathrm{S}}\, t} \quad , \tag{A.30}$$

the system equations of the induction machine in the stator fixed coordinate system (eqs. (A.31) to (A.33)) became algebraic.

$$u_{\mathrm{S}}^{\mathrm{S}} = R_{\mathrm{S}}\, i_{\mathrm{S}}^{\mathrm{S}} + \dot{\Psi}_{\mathrm{S}}^{\mathrm{S}} = R_{\mathrm{S}}\, i_{\mathrm{S}}^{\mathrm{S}} + \frac{d}{dt}\left(L_{\mathrm{S}\sigma}\, i_{\mathrm{S}}^{\mathrm{S}} + L_{\mathrm{h}}\, i_{\mu}^{\mathrm{S}}\right) \tag{A.31}$$

$$0 = R_{\mathrm{R}}\, i_{\mathrm{R}}^{\mathrm{S}} - \mathrm{i}\,\omega_{\mathrm{mech}} \Psi_{\mathrm{R}}^{\mathrm{S}} + \dot{\Psi}_{\mathrm{R}}^{\mathrm{S}} = R_{\mathrm{R}}\, i_{\mathrm{R}}^{\mathrm{S}} - \mathrm{i}\,\omega_{\mathrm{mech}} \left(L_{\mathrm{R}\sigma}\, i_{\mathrm{R}}^{\mathrm{S}} + L_{\mathrm{h}}\, i_{\mu}^{\mathrm{S}}\right) + \frac{d}{dt}\left(L_{\mathrm{R}\sigma}\, i_{\mathrm{R}}^{\mathrm{S}} + L_{\mathrm{h}}\, i_{\mu}^{\mathrm{S}}\right) \tag{A.32}$$

$$i_{\mu}^{\mathrm{S}} = i_{\mathrm{S}}^{\mathrm{S}} + i_{\mathrm{R}}^{\mathrm{S}} \tag{A.33}$$

In this state, certainly, also the currents simplify to

$$i_{\mathrm{S}} = \hat{I}_{\mathrm{S}}\, \mathrm{e}^{\mathrm{i}\,\omega_{\mathrm{S}}\, t} \quad , \quad i_{\mathrm{R}} = \hat{I}_{\mathrm{R}}\, \mathrm{e}^{\mathrm{i}\,\omega_{\mathrm{S}}\, t} \quad \text{and} \quad i_{\mu} = \hat{I}_{\mu}\, \mathrm{e}^{\mathrm{i}\,\omega_{\mathrm{S}}\, t} \quad . \tag{A.34}$$

Applying eqs. (A.30) and (A.34) to eqs. (A.31) to (A.33) the resulting equations describe the well known “T-equivalent circuit” of the induction motor, illustrated in Fig. A.2.

$$\hat{U}_{\mathrm{S}}^{\mathrm{S}} = R_{\mathrm{S}}\, \hat{I}_{\mathrm{S}}^{\mathrm{S}} + \mathrm{i}\,\omega_{\mathrm{S}} \left(L_{\mathrm{S}\sigma}\, \hat{I}_{\mathrm{S}}^{\mathrm{S}} + L_{\mathrm{h}}\, \hat{I}_{\mu}^{\mathrm{S}}\right) \tag{A.35}$$

$$0 = R_{\mathrm{R}}\, \hat{I}_{\mathrm{R}}^{\mathrm{S}} + \mathrm{i}\,\left(\omega_{\mathrm{mech}} - \omega_{\mathrm{S}}\right) \left(L_{\mathrm{R}\sigma}\, \hat{I}_{\mathrm{R}}^{\mathrm{S}} + L_{\mathrm{h}}\, \hat{I}_{\mu}^{\mathrm{S}}\right)$$

$$0 = \frac{R_{\mathrm{R}}}{s}\, \hat{I}_{\mathrm{R}}^{\mathrm{S}} + \mathrm{i}\,\omega_{\mathrm{S}} \left(L_{\mathrm{R}\sigma}\, \hat{I}_{\mathrm{R}}^{\mathrm{S}} + L_{\mathrm{h}}\, \hat{I}_{\mu}^{\mathrm{S}}\right) \tag{A.36}$$

$$\hat{I}_{\mu}^{\mathrm{S}} = \hat{I}_{\mathrm{S}}^{\mathrm{S}} + \hat{I}_{\mathrm{R}}^{\mathrm{S}} \tag{A.37}$$

In eq. (A.36), the definition of the slip s is used, which describes the relation between the mechanical angular frequency ω_{mech} and the angular frequency of the stator voltage ω_{S},

$$s = \frac{\omega_{\mathrm{S}} - \omega_{\mathrm{mech}}}{\omega_{\mathrm{S}}} \quad . \tag{A.38}$$

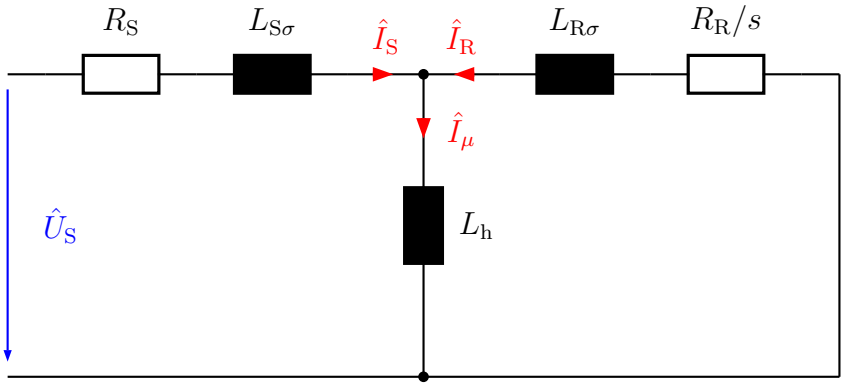

Figure A.2: Equivalent circuit of the induction motor for steady state, an illustration of eqs. (A.35) to (A.37).

A.4 Transformation to the Rotor Flux Oriented Coordinate System

For controlling an electrical machine, it is preferable to be able to adjust the magnetic flux and torque independently of each another, similar to a separately excited DC machine. This aim can be achieved by transforming eqs. (A.22) to (A.25) into the rotor flux oriented coordinate system (ΨCS). The relations for a general variable Z, defined in different coordinate systems, are

$$Z^\mathrm{S} = Z^\Psi \, \mathrm{e}^{\mathrm{i}\,\rho} \quad \text{and} \quad Z^\mathrm{R} = Z^\Psi \, \mathrm{e}^{\mathrm{i}(\rho-\varphi)} \quad , \tag{A.39}$$

according to Fig. A.3. Again, the superscript denotes in which coordinate system the variable is defined (S ...stator, R ...rotor, Ψ ...rotor flux).

Per definition, in the rotor flux oriented coordinate system ΨCS,

$$\Im\{\Psi_\mathrm{R}^\Psi\} \stackrel{!}{=} 0 \quad . \tag{A.40}$$

The following derivation of the differential equations for i_S and Ψ_R is based on Schröder [46, Chapter 13].

Transforming the differential equation for the rotor voltage circuit, using eq. (A.39) results in

$$\begin{aligned}
0 &= R_\mathrm{R}\, i_\mathrm{R}^\mathrm{R} + \dot{\Psi}_\mathrm{R}^\mathrm{R} \\
0 &= R_\mathrm{R}\, i_\mathrm{R}^\Psi \, \mathrm{e}^{\mathrm{i}(\rho-\varphi)} + \frac{d}{dt}\left(\Psi_\mathrm{R}^\Psi \, \mathrm{e}^{\mathrm{i}(\rho-\varphi)}\right) \\
0 &= R_\mathrm{R}\, i_\mathrm{R}^\Psi + \dot{\Psi}_\mathrm{R}^\Psi + \mathrm{i}\,(\dot{\rho}-\dot{\varphi})\,\Psi_\mathrm{R}^\Psi \\
\dot{\Psi}_\mathrm{R}^\Psi &= -R_\mathrm{R} \underbrace{\frac{\Psi_\mathrm{R}^\Psi - L_\mathrm{h}\, i_\mathrm{S}^\Psi}{L_\mathrm{h}+L_{\mathrm{R}\sigma}}}_{i_\mathrm{R}} - \mathrm{i}\,(\dot{\rho}-\dot{\varphi})\,\Psi_\mathrm{R}^\Psi \quad .
\end{aligned}$$

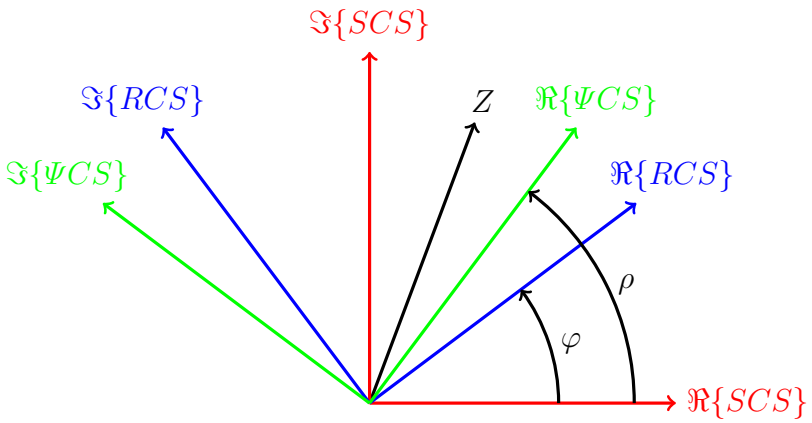

Figure A.3: Illustration of the transformation (eq. (A.39)) from the stator fixed (SCS) and the rotor fixed coordinate system (RCS) to the rotor flux oriented coordinate system $\Im\{\Psi CS\}$).

Splitting $\dot{\Psi}_{\mathrm{R}}^{\Psi}$ into its real and imaginary parts leads to

$$\begin{aligned}
\Re\{\dot{\Psi}_{\mathrm{R}}^{\Psi}\} &= \dot{\Psi}_{\mathrm{Rd}}^{\Psi} &&= \frac{R_{\mathrm{R}}}{L_{\mathrm{h}}+L_{\mathrm{R}\sigma}}\left(L_{\mathrm{h}}\, i_{\mathrm{Sd}}^{\Psi}-\Psi_{\mathrm{Rd}}^{\Psi}\right)\\
\Im\{\dot{\Psi}_{\mathrm{R}}^{\Psi}\} &= 0 &&= \frac{R_{\mathrm{R}}\, L_{\mathrm{h}}}{L_{\mathrm{h}}+L_{\mathrm{R}\sigma}}\, i_{\mathrm{Sq}}^{\Psi}-(\dot{\rho}-\dot{\varphi})\,\Psi_{\mathrm{Rd}}^{\Psi}\\
& & \dot{\rho} &= \dot{\varphi}+\frac{R_{\mathrm{R}}\, L_{\mathrm{h}}}{L_{\mathrm{h}}+L_{\mathrm{R}\sigma}}\,\frac{i_{\mathrm{Sq}}^{\Psi}}{\Psi_{\mathrm{Rd}}^{\Psi}} \quad .
\end{aligned}$$

The same transformation is performed for the differential equation for the stator voltage circuit.

$$\begin{aligned}
u_{\mathrm{S}}^{\mathrm{S}} &= R_{\mathrm{S}}\, i_{\mathrm{S}}^{\mathrm{S}}+\dot{\Psi}_{\mathrm{S}}^{\mathrm{S}}\\
u_{\mathrm{S}}^{\Psi}\,\mathrm{e}^{\mathrm{i}\,\rho} &= R_{\mathrm{S}}\, i_{\mathrm{S}}^{\Psi}\,\mathrm{e}^{\mathrm{i}\,\rho}+\frac{d}{dt}\left(\Psi_{\mathrm{S}}^{\Psi}\,\mathrm{e}^{\mathrm{i}\,\rho}\right)\\
u_{\mathrm{S}}^{\Psi} &= R_{\mathrm{S}}\, i_{\mathrm{S}}^{\Psi}+\dot{\Psi}_{\mathrm{S}}^{\Psi}+\mathrm{i}\,\dot{\rho}\,\Psi_{\mathrm{S}}^{\Psi}\\
u_{\mathrm{S}}^{\Psi} &= R_{\mathrm{S}}\, i_{\mathrm{S}}^{\Psi}+(L_{\mathrm{h}}+L_{\mathrm{S}\sigma})\, i_{\mathrm{S}}^{\dot{\Psi}}+L_{\mathrm{h}}\, i_{\mathrm{R}}^{\dot{\Psi}}+\mathrm{i}\,\dot{\rho}\left[(L_{\mathrm{h}}+L_{\mathrm{S}\sigma})\, i_{\mathrm{S}}^{\Psi}+L_{\mathrm{h}}\, i_{\mathrm{R}}^{\Psi}\right]\\
u_{\mathrm{S}}^{\Psi} &= R_{\mathrm{S}}\, i_{\mathrm{S}}^{\Psi}+(L_{\mathrm{h}}+L_{\mathrm{S}\sigma})\, i_{\mathrm{S}}^{\dot{\Psi}}+L_{\mathrm{h}}\underbrace{\frac{\dot{\Psi}_{\mathrm{R}}^{\Psi}-L_{\mathrm{h}}\, i_{\mathrm{S}}^{\dot{\Psi}}}{L_{\mathrm{h}}+L_{\mathrm{R}\sigma}}}_{\dot{i}_{\mathrm{R}}}+\mathrm{i}\,\dot{\rho}\left[(L_{\mathrm{h}}+L_{\mathrm{S}\sigma})\, i_{\mathrm{S}}^{\Psi}+L_{\mathrm{h}}\underbrace{\frac{\Psi_{\mathrm{R}}^{\Psi}-L_{\mathrm{h}}\, i_{\mathrm{S}}^{\Psi}}{L_{\mathrm{h}}+L_{\mathrm{R}\sigma}}}_{i_{\mathrm{R}}}\right]\\
u_{\mathrm{S}}^{\Psi} &= R_{\mathrm{S}}\, i_{\mathrm{S}}^{\Psi}+\mathrm{i}\,\dot{\rho}\underbrace{\left[(L_{\mathrm{h}}+L_{\mathrm{S}\sigma})-\frac{L_{\mathrm{h}}^2}{L_{\mathrm{h}}+L_{\mathrm{R}\sigma}}\right]}_{L_\sigma} i_{\mathrm{S}}^{\Psi}+\underbrace{\left[(L_{\mathrm{h}}+L_{\mathrm{S}\sigma})-\frac{L_{\mathrm{h}}^2}{L_{\mathrm{h}}+L_{\mathrm{R}\sigma}}\right]}_{L_\sigma} i_{\mathrm{S}}^{\dot{\Psi}}\\
&\quad+\underbrace{\left(\mathrm{i}\,\dot{\rho}\,\Psi_{\mathrm{R}}^{\Psi}+\dot{\Psi}_{\mathrm{R}}^{\Psi}\right)}_{\mathrm{i}\,\dot{\varphi}\,\Psi_{\mathrm{R}}-R_{\mathrm{R}}\frac{\Psi_{\mathrm{R}}-L_{\mathrm{h}}\, i_{\mathrm{S}}}{L_{\mathrm{h}}+L_{\mathrm{R}\sigma}}}\frac{L_{\mathrm{h}}}{L_{\mathrm{h}}+L_{\mathrm{R}\sigma}}\\
u_{\mathrm{S}}^{\Psi} &= \underbrace{\left(R_{\mathrm{S}}+\frac{L_{\mathrm{h}}^2}{(L_{\mathrm{h}}+L_{\mathrm{R}\sigma})^2}\, R_{\mathrm{R}}\right)}_{R} i_{\mathrm{S}}^{\Psi}+L_\sigma\, i_{\mathrm{S}}^{\dot{\Psi}}+\mathrm{i}\,\dot{\rho} L_\sigma\, i_{\mathrm{S}}^{\Psi}+\mathrm{i}\,\dot{\varphi}\,\frac{L_{\mathrm{h}}}{L_{\mathrm{h}}+L_{\mathrm{R}\sigma}}\,\Psi_{\mathrm{R}}^{\Psi}-\frac{R_{\mathrm{R}}\, L_{\mathrm{h}}}{(L_{\mathrm{h}}+L_{\mathrm{R}\sigma})^2}\,\Psi_{\mathrm{R}}^{\Psi}
\end{aligned}$$

Splitting these terms in their real and imaginary parts results in

$$u_{\mathrm{Sd}}^{\Psi} = R\, i_{\mathrm{Sd}}^{\Psi} + L_\sigma\, \dot{i}_{\mathrm{Sd}}^{\Psi} - \dot{\rho}\, L_\sigma\, i_{\mathrm{Sq}}^{\Psi} - \frac{R_{\mathrm{R}}\, L_{\mathrm{h}}}{(L_{\mathrm{h}} + L_{\mathrm{R}\sigma})^2}\, \Psi_{\mathrm{Rd}}^{\Psi}$$
$$u_{\mathrm{Sq}}^{\Psi} = R\, i_{\mathrm{Sq}}^{\Psi} + L_\sigma\, \dot{i}_{\mathrm{Sq}}^{\Psi} + \dot{\rho}\, L_\sigma\, i_{\mathrm{Sd}}^{\Psi} + \dot{\varphi}\, \frac{L_{\mathrm{h}}}{L_{\mathrm{h}} + L_{\mathrm{R}\sigma}}\, \Psi_{\mathrm{Rd}}^{\Psi} \quad .$$

Also, the torque of the induction motor (eq. (A.29)) can be expressed in terms of i_{S} and Ψ_{R}, according to [46, eq. 13.114].

$$T_{\mathrm{motor}} = \frac{3}{2}\, p\, \Im\left\{\Psi_{\mathrm{h}}\, i_{\mathrm{S}}^{*}\right\} \qquad \Psi_{\mathrm{h}} = L_{\mathrm{h}}\,(i_{\mathrm{S}} + i_{\mathrm{R}})$$
$$T_{\mathrm{motor}} = \frac{3}{2}\, p\, \Im\left\{\Psi_{\mathrm{h}}\left(\frac{\Psi_{\mathrm{h}}^{*}}{L_{\mathrm{h}}} - i_{\mathrm{R}}^{*}\right)\right\} = -\frac{3}{2}\, p\, \Im\left\{\Psi_{\mathrm{h}}\, i_{\mathrm{R}}^{*}\right\} \qquad \Psi_{\mathrm{h}} = \Psi_{\mathrm{R}} - L_{\mathrm{R}\sigma}\, i_{\mathrm{R}}$$
$$T_{\mathrm{motor}} = -\frac{3}{2}\, p\, \Im\left\{(\Psi_{\mathrm{R}} - L_{\mathrm{R}\sigma}\, i_{\mathrm{R}})\, i_{\mathrm{R}}^{*}\right\} = -\frac{3}{2}\, p\, \Im\left\{\Psi_{\mathrm{R}}\, i_{\mathrm{R}}^{*}\right\} \qquad \Psi_{\mathrm{R}} = L_{\mathrm{h}}\, i_{\mathrm{S}} + (L_{\mathrm{h}} + L_{\mathrm{R}\sigma})\, i_{\mathrm{R}}$$
$$T_{\mathrm{motor}} = -\frac{3}{2}\, p\, \Im\left\{\Psi_{\mathrm{R}}\left(\frac{\Psi_{\mathrm{R}}^{*} - L_{\mathrm{h}}\, i_{\mathrm{S}}^{*}}{L_{\mathrm{h}} + L_{\mathrm{R}\sigma}}\right)\right\} = \frac{3}{2}\, p\, \frac{L_{\mathrm{h}}}{L_{\mathrm{h}} + L_{\mathrm{R}\sigma}}\, \Im\left\{\Psi_{\mathrm{R}}\, i_{\mathrm{S}}^{*}\right\} \qquad \Im\left\{\Psi_{\mathrm{R}}\right\} = 0$$
$$T_{\mathrm{motor}} = \frac{3}{2}\, p\, \frac{L_{\mathrm{h}}}{L_{\mathrm{h}} + L_{\mathrm{R}\sigma}}\, \Psi_{\mathrm{Rd}}\, i_{\mathrm{Sq}}$$

To summarise, the differential equations of the induction machine in the rotor flux oriented coordinate system and some comments are listed below.

- Ψ_{Rd} and ρ cannot be measured directly in a simple way. In this work, they are obtained by integration [77, Chapter 12] of eqs. (A.44) and (A.45). However, many other methods have been proposed in literature, e.g. [78].

  That means, while operating the machine these differential equations are solved permanently [79] using the simple *Euler method* to give an online estimation of the rotor flux $\Psi_{\mathrm{Rd}}^{\Psi}$, needed in the machine's controller. There is a high parameter sensitivity relating to the rotor time constant, which may vary for different operational states in practice. For that reason, again, an adequate knowledge of the equivalent circuit parameters of the machine is required.

- Subtracting the compensating voltages $u_{\mathrm{d,\,comp}}$ and $u_{\mathrm{q,\,comp}}$, eqs. (A.42) and (A.43) simplify to

  $$\frac{d\, i_{\mathrm{Sd}}^{\Psi}}{dt} = \frac{1}{L_\sigma}\left(u_{\mathrm{Sd}}^{\Psi} - R\, i_{\mathrm{Sd}}^{\Psi}\right) \quad \text{and} \quad \frac{d\, i_{\mathrm{Sq}}^{\Psi}}{dt} = \frac{1}{L_\sigma}\left(u_{\mathrm{Sq}}^{\Psi} - R\, i_{\mathrm{Sq}}^{\Psi}\right) \quad , \tag{A.41}$$

  which gives a linear control path for the currents.

- As a result of the transformation, the torque and the rotor flux decouple (eqs. (A.44) and (A.46)), so that they can be controlled independently of each other using an extra control circuit for i_{Sd}^{Ψ} and i_{Sq}^{Ψ} and accordingly a superposed control circuit for the flux and torque or speed.

$$u_{\mathrm{Sd}}^{\Psi} = R\, i_{\mathrm{Sd}}^{\Psi} + L_{\sigma}\, i_{\mathrm{Sd}}^{\dot{\Psi}} \underbrace{-\dot{\rho}\, L_{\sigma}\, i_{\mathrm{Sq}}^{\Psi} - \frac{R_{\mathrm{R}}\, L_{\mathrm{h}}}{(L_{\mathrm{h}} + L_{\mathrm{R}\sigma})^2}\, \Psi_{\mathrm{Rd}}^{\Psi}}_{u_{\mathrm{d,\,comp}}} \tag{A.42}$$

$$u_{\mathrm{Sq}}^{\Psi} = R\, i_{\mathrm{Sq}}^{\Psi} + L_{\sigma}\, i_{\mathrm{Sq}}^{\dot{\Psi}} \underbrace{+\dot{\rho}\, L_{\sigma}\, i_{\mathrm{Sd}}^{\Psi} + \dot{\varphi}\, \frac{L_{\mathrm{h}}}{L_{\mathrm{h}} + L_{\mathrm{R}\sigma}}\, \Psi_{\mathrm{Rd}}^{\Psi}}_{u_{\mathrm{q,\,comp}}} \tag{A.43}$$

$$\dot{\Psi}_{\mathrm{Rd}}^{\Psi} = \frac{R_{\mathrm{R}}}{L_{\mathrm{h}} + L_{\mathrm{R}\sigma}} \left(L_{\mathrm{h}}\, i_{\mathrm{Sd}}^{\Psi} - \Psi_{\mathrm{Rd}}^{\Psi} \right) \tag{A.44}$$

$$\dot{\rho} = \dot{\varphi} + \frac{R_{\mathrm{R}}\, L_{\mathrm{h}}}{L_{\mathrm{h}} + L_{\mathrm{R}\sigma}}\, \frac{i_{\mathrm{Sq}}^{\Psi}}{\Psi_{\mathrm{Rd}}^{\Psi}} \tag{A.45}$$

$$T_{\mathrm{motor}} = \frac{3}{2}\, p\, \frac{L_{\mathrm{h}}}{L_{\mathrm{h}} + L_{\mathrm{R}\sigma}}\, \Psi_{\mathrm{Rd}}^{\Psi}\, i_{\mathrm{Sq}}^{\Psi} \tag{A.46}$$

Appendix B

Synchronous Reluctance Machine - FEA Results

The results of the FEM computations for the SynRM are obtained via transient simulations with fixed current and speed. The dependencies of the magnetising inductances L_d and L_q on the current, used for the speed controller (c.f. Section 3.3.2), are illustrated in Fig. B.1. The two-dimensional lookup tables to simulate d-q-model eqs. (3.44) are shown in Fig. B.2.

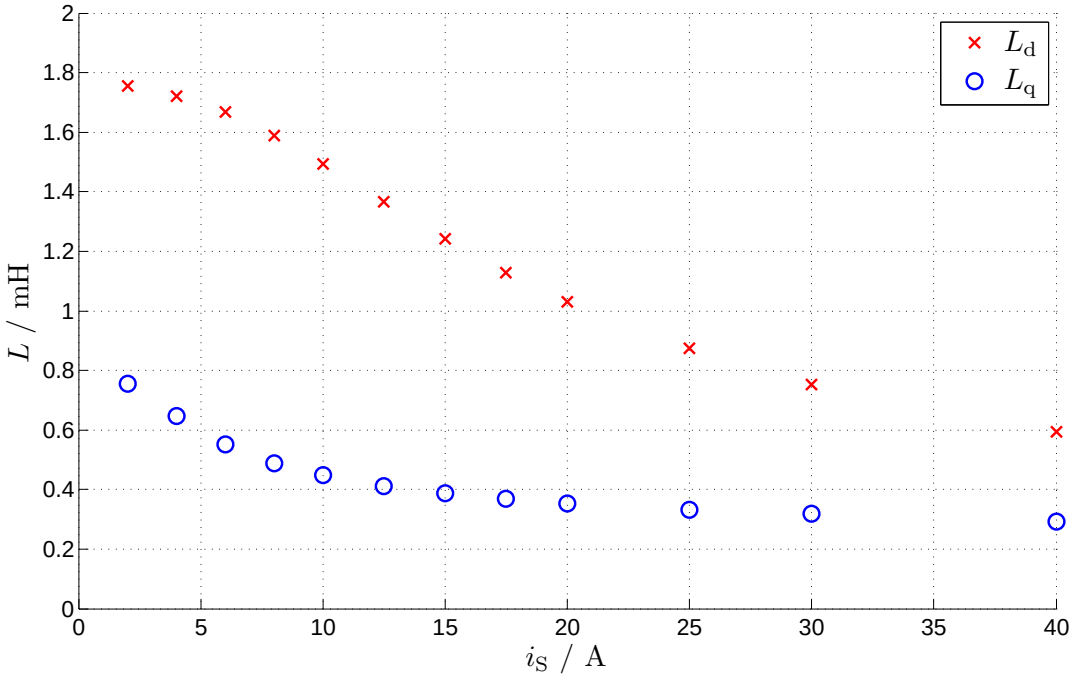

Figure B.1: Dependencies of the simulated magnetising inductances L_d and L_q on the current, used for the speed controller (c.f. Section 3.3.2).

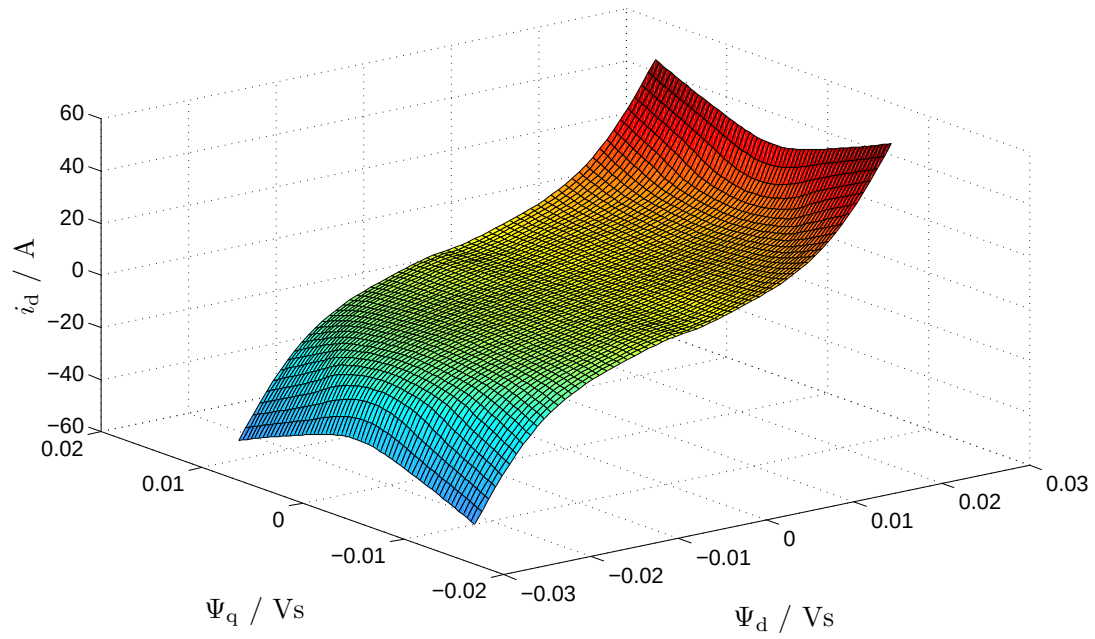

(a) d-axis current i_d as a function of of Ψ_d and Ψ_q used for the two-dimensional lookup table in the simulations.

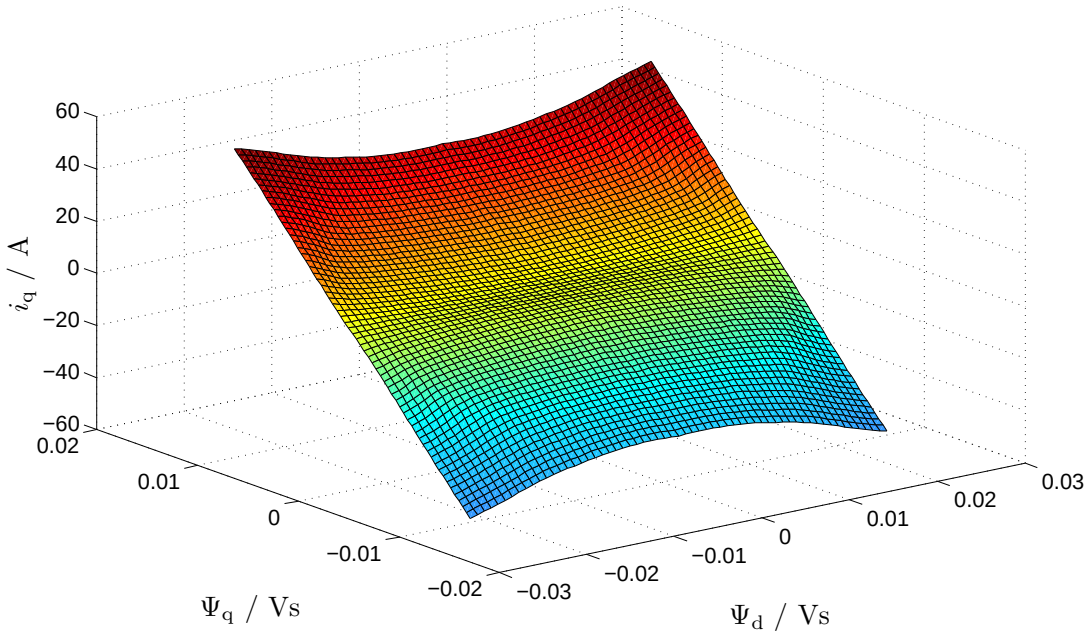

(b) q-axis current i_q as a function of of Ψ_d and Ψ_q used for the two-dimensional lookup table in the simulations.

Figure B.2: Two-dimensional lookup tables, resulting from FEA (c.f. Fig. 3.8), to simulate d-q-model eqs. (3.44).

Appendix C

Influence of Magnetisation Characteristic

The magnetisation characteristic used for the computations of the machine design was obtained by fitting a function, containing a linear and an arctan term [80], to a no-load characteristic of an IM of a benchmark study.

Fig. C.1 illustrates the differences between the result of the fit and the magnetisation characteristics specified by the steel producer, which might by explained by the degradation of the magnetic properties caused by the laser cutting process

The effect on the computation performed using the modelling approach of Section 2.2.1 and a geometry, according to Fig. 4.3, of the main inductance L_h of the IM is shown in Fig. C.2. It can be assumed that the magnetisation curve of the manufactured machine is located between these two extremes.

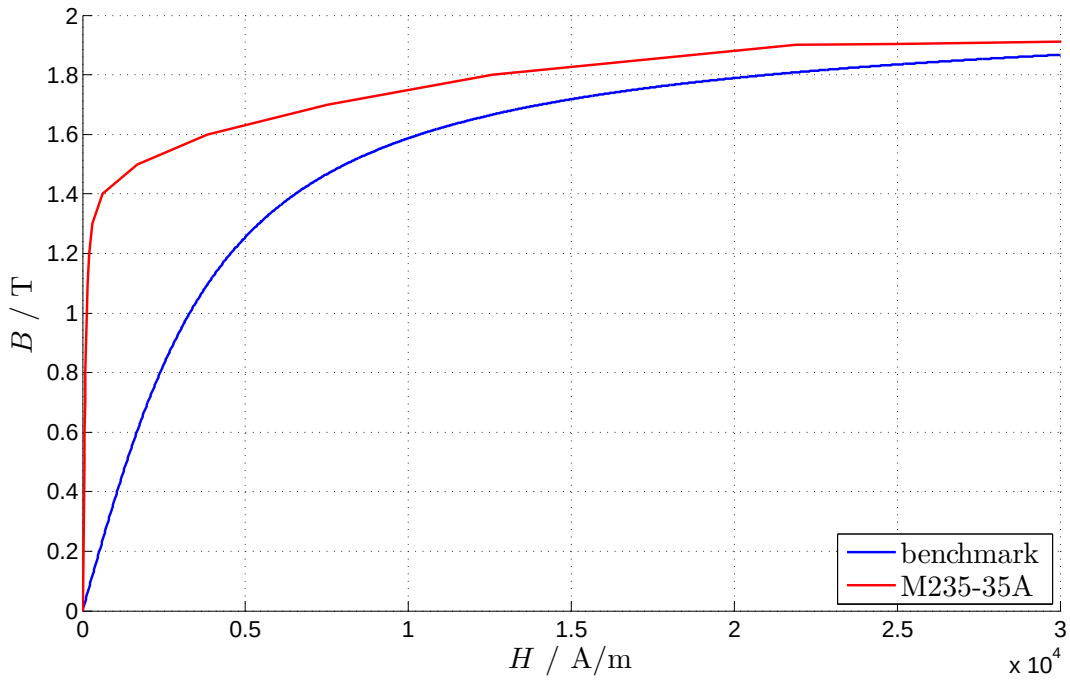

Figure C.1: Comparison of the magnetisation curve derived from a machine from a benchmark study (blue) and the specification of the steel producer (red, M235-25A).

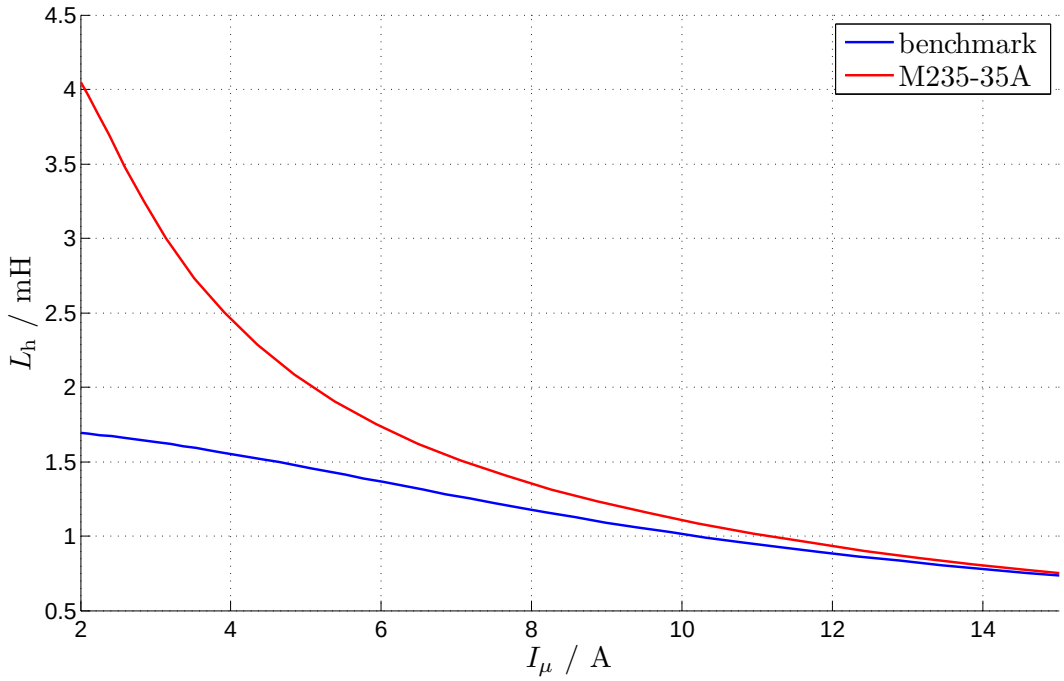

Figure C.2: Comparison of the computed main inductance L_h as a function of the magnetising current I_μ, using the magnetisation curve derived from a machine from a benchmark study (blue) and the specification of the steel producer (red, M235-25A).

Appendix D

Pseudo Cycle

The original cycle, defined in Fig. 1.2, was specified by a customer and we were not allowed to publish it for the reason of confidentiality. For that reason, we defined a so called pseudo cycle with a similar load profile, also including two step function responses of position, slow movement and resting times.

This cycle, pictured in Fig. D.1, was used for the publications [72, 73] and to measure the temperature increase of the actuator, shown and discussed in Section 6.2.

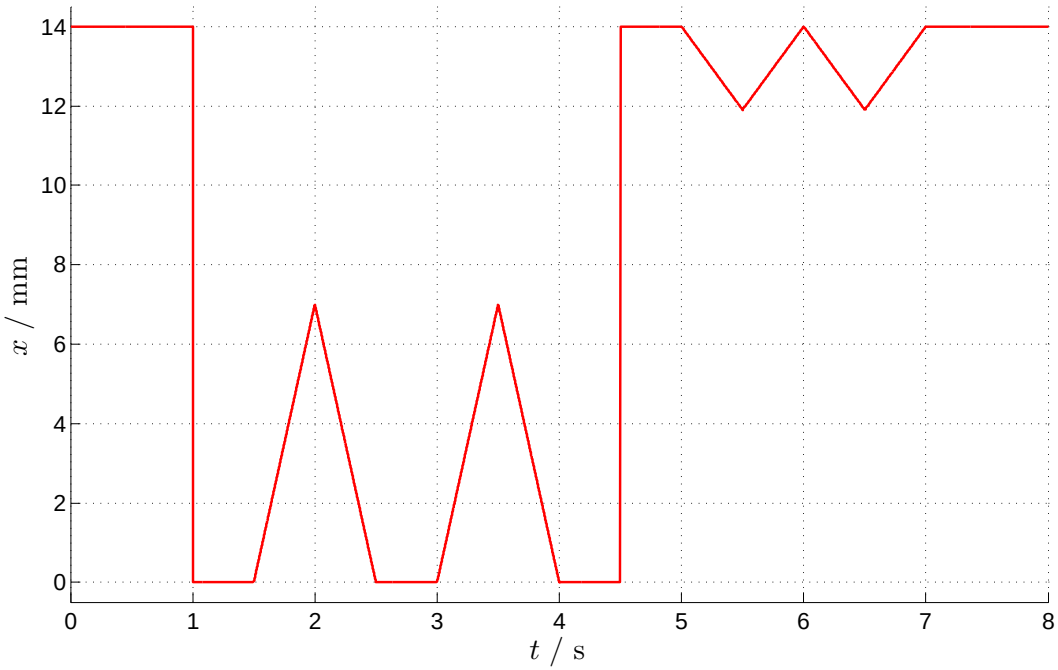

Figure D.1: A pseudo cycle, used for publications and to measure the temperature increase of the actuator.

Fig. D.2 shows the simulated mean copper losses $\overline{P}_{\mathrm{Cu}}$ to run through the cycle, shown in Fig. D.1, for the final design of the IM and SynRM (see Section 4), assuming a winding temperature of $T_{\mathrm{winding}} = 100\,^{\circ}\mathrm{C}$ and $T_{\mathrm{winding}} = 150\,^{\circ}\mathrm{C}$, respectively. (Based on the prediction of the thermal model, the actuator will take on a steady-state temperature between these two extreme cases during operation.) Not only the total copper loss, including the copper loss of the rotor, of the IM, but also the one of the stator only are higher than those of the IM.

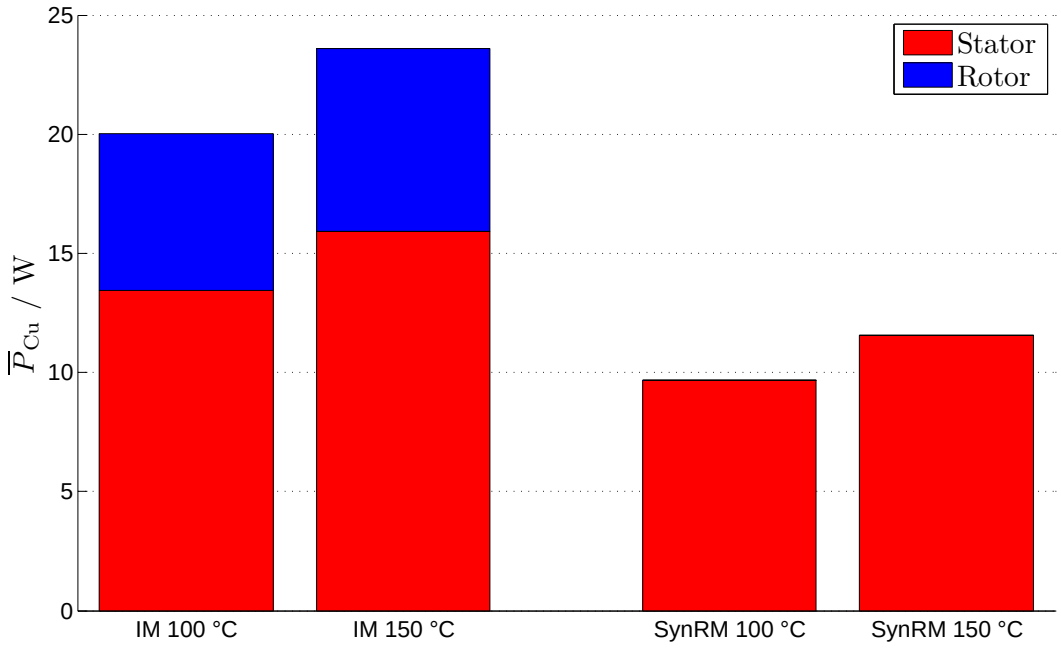

Figure D.2: Comparison of the simulated mean copper losses $\overline{P}_{\mathrm{Cu}}$ to run through the cycle for the IM and SynRM, assuming a winding temperature of $T_{\mathrm{winding}} = 100\,^{\circ}\mathrm{C}$ and $T_{\mathrm{winding}} = 150\,^{\circ}\mathrm{C}$, respectively. $\overline{P}_{\mathrm{Cu}}$ increases approximately proportionally with the temperature, due to the change of the ohmic resistance.

Bibliography

[1] I. Boldea and S. Nasar, *Linear Electric Actuators and Generators*. Cambridge University Press, 1997.

[2] S. Nasar and I. Boldea, *Linear Electric Motors: Theory, Design, and Practical Applications*. Prentice-Hall, 1987.

[3] J. Gieras, *Linear Induction Drives*. Monographs in electrical and electronic engineering, Clarendon Press, 1994.

[4] B. Gysen, K. Meessen, J. Paulides, and E. Lomonova, "Semi-analytical calculation of the armature reaction in slotted tubular permanent magnet actuators," *Magnetics, IEEE Transactions on*, vol. 44, pp. 3213–3216, Nov 2008.

[5] N. Vrijsen, J. Jansen, and E. Lomonova, "Prediction of Magnetic Hysteresis in the Force of a Prebiased E-Core Reluctance Actuator," *Industry Applications, IEEE Transactions on*, vol. 50, pp. 2476–2484, July 2014.

[6] W. Bauer and W. Amrhein, "Electrical Design Considerations for a Bearingless Axial-Force/Torque Motor," *Industry Applications, IEEE Transactions on*, vol. 50, pp. 2512–2522, July 2014.

[7] J. Ouyang and Y. Zhu, "Z-Shaped MEMS Thermal Actuators: Piezoresistive Self-Sensing and Preliminary Results for Feedback Control," *Microelectromechanical Systems, Journal of*, vol. 21, pp. 596–604, June 2012.

[8] W. Leonhard, "Controlled AC drives, a successful transition from ideas to industrial practice," *Control Engineering Practice*, vol. 4, no. 7, pp. 897–908, 1996.

[9] A. Vagati, "The synchronous reluctance solution: a new alternative in AC drives," in *Industrial Electronics, Control and Instrumentation, 1994. IECON '94., 20th International Conference on*, vol. 1, pp. 1–13, Sept. 1994.

[10] E. Howard, M. Kamper, and S. Gerber, "Flux barrier and skew design optimisation of reluctance synchronous machines," in *Electrical Machines (ICEM), 2014 International Conference on*, pp. 1186–1192, Sept. 2014.

[11] M. Gamba, G. Pellegrino, and F. Cupertino, "Optimal number of rotor parameters for the automatic design of Synchronous Reluctance machines," in *Electrical Machines (ICEM), 2014 International Conference on*, pp. 1334–1340, Sept. 2014.

[12] J. Barta and C. Ondrusek, "Design and optimization of synchronous reluctance machine," in *Mechatronics - Mechatronika (ME), 2014 16th International Conference on*, pp. 60–64, Dec. 2014.

[13] K. Wang, Z. Zhu, G. Ombach, M. Koch, S. Zhang, and J. Xu, "Optimal slot/pole and flux-barrier layer number combinations for synchronous reluctance machines," in *Ecological Vehicles and Renewable Energies (EVER), 2013 8th International Conference and Exhibition on*, pp. 1–8, March 2013.

[14] T. Sebastian, "Temperature effects on torque production and efficiency of PM motors using NdFeB magnets," *Industry Applications, IEEE Transactions on*, vol. 31, pp. 353–357, March 1995.

[15] N. Haque, A. Hughes, S. Lim, and C. Vernon, "Rare Earth Elements: Overview of Mining, Mineralogy, Uses, Sustainability and Environmental Impact," *Resources*, vol. 3, no. 4, pp. 614–635, 2014.

[16] W. Jones, "The rare-earth-metal bottleneck," *Spectrum, IEEE*, vol. 47, pp. 80–80, Jan. 2010.

[17] R. Joetten and G. Maeder, "Control Methods for Good Dynamic Performance Induction Motor Drives Based on Current and Voltage as Measured Quantities," *Industry Applications, IEEE Transactions on*, vol. IA-19, pp. 356–363, May 1983.

[18] A. Chiba and T. Fukao, "A closed-loop operation of super high-speed reluctance motor for quick torque response," *Industry Applications, IEEE Transactions on*, vol. 28, pp. 600–606, May 1992.

[19] A. Boglietti and M. Pastorelli, "Induction and synchronous reluctance motors comparison," in *Industrial Electronics, 2008. IECON 2008. 34th Annual Conference of IEEE*, pp. 2041–2044, Nov. 2008.

[20] A. Vagati, A. Fratta, G. Franceschini, and P. Rosso, "AC motors for high-performance drives: a design-based comparison," *Industry Applications, IEEE Transactions on*, vol. 32, pp. 1211–1219, Sept. 1996.

[21] T. Miller, A. Hutton, C. Cossar, and D. Staton, "Design of a synchronous reluctance motor drive," *Industry Applications, IEEE Transactions on*, vol. 27, pp. 741–749, Jul 1991.

[22] A. Boglietti, A. Cavagnino, M. Pastorelli, and A. Vagati, "Experimental comparison of induction and synchronous reluctance motors performance," in *Industry Applications Conference, 2005. Fourtieth IAS Annual Meeting. Conference Record of the 2005*, vol. 1, pp. 474–479, Oct. 2005.

[23] A. Boglietti, A. Cavagnino, M. Pastorelli, D. Staton, and A. Vagati, "Thermal analysis of induction and synchronous reluctance motors," *Industry Applications, IEEE Transactions on*, vol. 42, pp. 675–680, May 2006.

[24] A. de Almeida, F. Ferreira, and G. Baoming, "Beyond Induction Motors - Technology Trends to Move Up Efficiency," *Industry Applications, IEEE Transactions on*, vol. 50, pp. 2103–2114, May 2014.

[25] R. Wang, D. Boroyevich, P. Ning, Z. Wang, F. Wang, P. Mattavelli, K. Ngo, and K. Rajashekara, "A High-Temperature SiC Three-Phase AC - DC Converter Design for $> 100\,^{\circ}C$ Ambient Temperature," *Power Electronics, IEEE Transactions on*, vol. 28, pp. 555–572, Jan. 2013.

[26] P. Ning, F. Wang, and K. Ngo, "High-Temperature SiC Power Module Electrical Evaluation Procedure," *Power Electronics, IEEE Transactions on*, vol. 26, pp. 3079–3083, Nov. 2011.

[27] T. Funaki, J. Balda, J. Junghans, A. Kashyap, H. Mantooth, F. Barlow, T. Kimoto, and T. Hikihara, "Power Conversion With SiC Devices at Extremely High Ambient Temperatures," *Power Electronics, IEEE Transactions on*, vol. 22, pp. 1321–1329, July 2007.

[28] P. Ning, D. Zhang, R. Lai, D. Jiang, F. Wang, D. Boroyevich, R. Burgos, K. Karimi, V. Immanuel, and E. Solodovnik, "High-Temperature Hardware: Development of a 10-kW High-Temperature, High-Power-Density Three-Phase ac-dc-ac SiC Converter," *Industrial Electronics Magazine, IEEE*, vol. 7, pp. 6–17, March 2013.

[29] M. Huque, S. Islam, L. Tolbert, and B. Blalock, "A 200 °C Universal Gate Driver Integrated Circuit for Extreme Environment Applications," *Power Electronics, IEEE Transactions on*, vol. 27, pp. 4153–4162, Sept 2012.

[30] P. Kakosimos, A. Sarigiannidis, M. Beniakar, A. Kladas, and C. Gerada, "Induction Motors Versus Permanent-Magnet Actuators for Aerospace Applications," *Industrial Electronics, IEEE Transactions on*, vol. 61, pp. 4315–4325, Aug. 2014.

[31] Verein Deutscher Ingenieure, VDI-Gesellschaft Verfahrenstechnik und Chemieingenieurwesen (GVC), *VDI-Wärmeatlas, Zehnte, bearbeitete und erweiterte Auflage*. Springer, 2005.

[32] P. von Böckh and T. Wetzel, *Wärmeübertragung, Grundlagen und Praxis, 4., bearbeitete Auflage*. Springer, 2011.

[33] E. Seefried and O. Mildenberger, *Elektrische Maschinen und Antriebstechnik: Grundlagen und Betriebsverhalten ; mit 10 Tabellen*. Vieweg Verlag, Friedr, & Sohn Verlagsgesellschaft mbH, 2001.

[34] A. Boglietti, A. Cavagnino, and M. Lazzari, "Computational Algorithms for Induction-Motor Equivalent Circuit Parameter Determination - Part I: Resistances and Leakage Reactances," *Industrial Electronics, IEEE Transactions on*, vol. 58, pp. 3723–3733, Sept. 2011.

[35] A. Boglietti, A. Cavagnino, and M. Lazzari, "Computational Algorithms for Induction Motor Equivalent Circuit Parameter Determination - Part II: Skin Effect and Magnetizing Characteristics," *Industrial Electronics, IEEE Transactions on*, vol. 58, pp. 3734–3740, Sept. 2011.

[36] JSOL Corporation, "Simulation Technology for Electromechanical Design." `https://www.jmag-international.com/`. accessed on 20-04-2015.

[37] J. Pyrhonen, T. Jokinen, and V. Hrabovcova, *Design of Rotating Electrical Machines*. John Wiley & Sons, Ltd., 2008.

[38] R. Richter, *Elektrische Maschinen: Allgemeine Berechnungselemente. Die Gleichstrommaschine*. No. 1, Birkhäuser Verlag, Basel and Stuttgart, Dritte, erweiterte Auflage ed., 1967.

[39] R. Richter, *Elektrische Maschinen: Die Induktionsmaschinen*. No. 4, Birkhäuser Verlag, Basle and Stuttgart, Zweite, verbesserte Auflage ed., 1954.

[40] G. Müller, K. Vogt, and B. Ponick, *Berechnung elektrischer Maschinen*. No. Bd. 2, Wiley-VCH, 2008.

[41] R. Plato, *Numerische Mathematik kompakt: Grundlagenwissen für Studium und Praxis*. Vieweg, 2006.

[42] W. H. Press, S. A. Teukolsky, W. T. Vetterling, and B. P. Flannery, *Numerical Recipes 3rd Edition: The Art of Scientific Computing*. Cambridge University Press, 2007.

[43] K. Hasse, *Zur Dynamik drehzahlgeregelter Antriebe mit stromrichtergespeisten Asynchron-Kurzschlußläufermaschinen*. Technische Hochschule Darmstadt, 1969.

[44] F. Blaschke, *Das Verfahren der Feldorientierung zur Regelung der Drehfeldmaschine*. Technische Universität Carolo-Wilhelmina zu Braunschweig, 1974.

[45] C. Maffezzoni, N. Schiavoni, and G. Ferretti, "Robust design of cascade control," *Control Systems Magazine, IEEE*, vol. 10, pp. 21–25, Jan. 1990.

[46] D. Schröder, *Elektrische Antriebe - Regelung von Antriebssystemen*. Springer, 2009.

[47] J. Espina, A. Arias, J. Balcells, and C. Ortega, "Speed Anti-Windup PI strategies review for Field Oriented Control of Permanent Magnet Synchronous Machines," in *Compatibility and Power Electronics, 2009. CPE '09.*, pp. 279–285, May 2009.

[48] M. Koyama, M. Yano, I. Kamiyama, and S. Yano, "Microprocessor-Based Vector Control System for Induction Motor Drives with Rotor Time Constant Identification Function," *Industry Applications, IEEE Transactions on*, vol. IA-22, pp. 453–459, May 1986.

[49] J. G. Ziegler and N. B. Nichols, "Optimum Settings for Automatic Controllers," *Transactions of ASME*, vol. 64, pp. 759–768, 1942.

[50] A. Alexandridis, G. Konstantopoulos, and Q. Zhong, "Advanced Integrated Modeling and Analysis for Adjustable Speed Drives of Induction Motors Operating With Minimum Losses," *Energy Conversion, IEEE Transactions on*, vol. PP, pp. 1–10, Feb. 2015.

[51] R. Ortega, J. A. L. Perez, P. J. Nicklasson, and H. Sira-Ramirez, *Passivity-based Control of Euler-Lagrange Systems: Mechanical, Electrical and Electromechanical Applications*. Springer, 1998.

[52] I. Boldea, *Reluctance Synchronous Machines and Drives*. Clarendon Press, 1996.

[53] A. Vagati, M. Pastorelli, F. Scapino, and G. Franceschini, "Impact of cross saturation in synchronous reluctance motors of the transverse-laminated type," *Industry Applications, IEEE Transactions on*, vol. 36, pp. 1039–1046, July 2000.

[54] A. Binder, *Elektrische Maschinen und Antriebe: Grundlagen, Betriebsverhalten*. Springer, 2012.

[55] A. Vagati, A. Canova, M. Chiampi, M. Pastorelli, and M. Repetto, "Improvement of synchronous reluctance motor design through finite-element analysis," in *Industry Applications Conference, 1999. Thirty-Fourth IAS Annual Meeting. Conference Record of the 1999 IEEE*, vol. 2, pp. 862–871, 1999.

[56] V. Honsinger, "The Inductances Ld and Lq of Reluctance Machines," *Power Apparatus and Systems, IEEE Transactions on*, vol. PAS-90, pp. 298–304, Jan. 1971.

[57] X. Luo, A. El-Antably, and T. Lipo, "Multiple coupled circuit modeling of synchronous reluctance machines," in *Industry Applications Society Annual Meeting, 1994., Conference Record of the 1994 IEEE*, pp. 281–289 vol.1, Oct. 1994.

[58] J. Dankert and H. Dankert, *Technische Mechanik: Statik, Festigkeitslehre, Kinematik/Kinetik*. Springer Vieweg, 2009.

[59] K. Malekian, M. Sharif, and J. Milimonfared, "An optimal current vector control for synchronous reluctance motors incorporating field weakening," in *Advanced Motion Control, 2008. AMC '08. 10th IEEE International Workshop on*, pp. 393–398, March 2008.

[60] R. Betz, R. Lagerquist, M. Jovanovic, T. Miller, and R. Middleton, "Control of synchronous reluctance machines," *Industry Applications, IEEE Transactions on*, vol. 29, pp. 1110–1122, Nov. 1993.

[61] J. Ahn, S.-B. Lim, K.-C. Kim, J. Lee, J.-H. Choi, S. Kim, and J. Hong, "Field weakening control of synchronous reluctance motor for electric power steering," *Electric Power Applications, IET*, vol. 1, pp. 565–570, July 2007.

[62] A. Binder, "Untersuchung zur magnetischen Kopplung von Längs- und Querachse durch Sättigung am Beispiel der Reluktanzmaschine," *Archiv für Elektrotechnik*, vol. 72, no. 4, pp. 277–282, 1989.

[63] M. Kamper and A. Volsdhenk, "Effect of rotor dimensions and cross magnetisation on Ld and Lq inductances of reluctance synchronous machine with cageless flux barrier rotor," *Electric Power Applications, IEE Proceedings* -, vol. 141, pp. 213–220, Jul. 1994.

[64] A. Tessarolo, M. Degano, and N. Bianchi, "On the analytical estimation of the airgap field in synchronous reluctance machine," in *Electrical Machines (ICEM), 2014 International Conference on*, pp. 239–244, Sept. 2014.

[65] MathWorks, "Accelerating the pace of engineering and science." `http://www.mathworks.de/index.html`. accessed on 20-04-2015.

[66] D. Goldberg, *Genetic Algorithms in Search, Optimization, and Machine Learning*. Addison-Wesley, 1989.

[67] K. Kabus, *Mechanik und Festigkeitslehre: Mit 266 Lehrbeispielen und einer Beilage mit 42 Tabellen, 25 Diagrammen und zahlreichen Formeln. Hauptbd.* Hanser, 2009.

[68] M. Bali and A. Muetze, "Influences of CO2 and FKL-laser cutting as well as mechanical cutting on the magnetic properties of electric steel sheets determined by Epstein frame and stator lamination stack measurements," in *Energy Conversion Congress and Exposition (ECCE), 2014 IEEE*, pp. 1443–1450, Sept. 2014.

[69] R. Siebert, J. Schneider, and E. Beyer, "Laser Cutting and Mechanical Cutting of Electrical Steels and its Effect on the Magnetic Properties," *Magnetics, IEEE Transactions on*, vol. 50, pp. 1–4, Apr. 2014.

[70] R. Krishnan and F. C. Doran, "Study of Parameter Sensitivity in High-Performance Inverter-Fed Induction Motor Drive Systems," *Industry Applications, IEEE Transactions on*, vol. IA-23, pp. 623–635, Jul. 1987.

[71] H. Toliyat, E. Levi, and M. Raina, "A review of RFO induction motor parameter estimation techniques," *Energy Conversion, IEEE Transactions on*, vol. 18, pp. 271–283, June 2003.

[72] K. Lang, A. Muetze, R. Bauer, and W. Rossegger, "Design of PM free brushless AC machines based actuators for elevated temperature environments," in *9th IEEE International Electric Machines and Drives Conference (IEMDC), Coeur d'Alne, ID, USA*, pp. 696–702, May. 2015.

[73] K. Lang, A. Muetze, R. Bauer, and S. Pircher, "Comparison of induction and synchronous reluctance machine based actuators for elevated temperature environments," in *17th European Conference on Power Electronics and Applications, EPE'2015 ECCE Europe, Geneva, Switzerland*, Sept. 2015. To appear.

[74] F. Carter, "Air-Gap Induction," *The Electrical World and Engineer*, vol. 38, pp. 884 – 888, 1901.

[75] D. Schröder, *Elektrische Antriebe - Grundlagen*. Springer, 2009.

[76] R. Fischer, *Elektrische Maschinen*. Hanser, 2006.

[77] W. Leonhard, *Control of Electrical Drives*. Springer Berlin Heidelberg, 2001.

[78] G. C. Verghese and S. Sanders, "Observers for flux estimation in induction machines," *Industrial Electronics, IEEE Transactions on*, vol. 35, pp. 85–94, Feb. 1988.

[79] D. Muschick, R. Bauer, N. Dourdoumas, and W. Rossegger, "Effekte zeitdiskreter Ansteuerung von Asynchronmaschinen bei hohen Drehzahlen.," *Elektrotechnik und Informationstechnik*, vol. 130, no. 6, pp. 177–183, 2013.

[80] C. Perez-Rojas, "Fitting saturation and hysteresis via arctangent functions," *Power Engineering Review, IEEE*, vol. 20, pp. 55–57, Nov. 2000.

Glossary

A	linear current density, current sheet.
A_{C}	cross section area of one conductor.
A_{Cu}	cross section area of copper content in stator / rotor.
$A_{\mathrm{cyclinder}}$	surface area cylinder.
$\hat{A}$	peak value of linear current density, current sheet.
α	angle coordinate.
a_{RSO}	rotor slot opening width .
a_{SSO}	stator slot opening width.
a_{R}	tooth width rotor.
a_{S}	tooth width stator.
A_{slot}	cross section area of one slot.
B_δ	flux density in the air gap.
$\hat{B}_\delta$	peak value of flux density in the air gap.
β_{R}	electrical angle between rotor and stator reference frame.
$\hat{B}_{\mathrm{S\,slot}}$	stator slot flux density.
$\hat{B}_{\mathrm{S\,tooth}}$	stator tooth flux density.
d_{bar}	rotor bar diameter.
d_δ	diameter mid of the air gap.
δ	air gap length.
δ_{eff}	effective air gap length.
Δt	time tolerance of the cycle.
d_{RO}	rotor outer diameter.
d_{shaft}	shaft diameter.
d_{SI}	stator inner diameter.
d_{SO}	stator outer diameter.
d_{spindle}	spindle diameter.
η_{fric}	friction coefficient.
F_{load}	force of the spring.
f_{Pr}	function of Prandtl number.
g	gravity acceleration.
Gr	Grashof number.
h_{bar}	distance between the outer diameter of rotor and the rotor bar.
h_{RJ}	height rotor yoke.

h_{RT}	tooth height rotor.
h_{SJ}	height stator yoke.
h_{ST}	tooth height stator.
$H_{\mathrm{S\,tooth}}$	stator tooth magnetic field strength.
I	mass moment of inerita.
i_{d}	direct axis current.
$\hat{I}_{\mu}$	peak value of magnetising current, steady state.
i_{μ}	magnetising current.
I_{Ph}	electric phase current.
i_{q}	quadrature axis current.
$\hat{I}_{\mathrm{R}}$	peak value of rotor current, steady state.
i_{R}	rotor current.
$\hat{I}_{\mathrm{S}}$	peak value of stator current, steady state.
i_{S}	stator current.
I_{shaft}	shaft mass moment of inerita.
J_{RMS}	current density, rms-value.
k_{C}	Carter factor of the slot-teeth layer.
k_{sff}	slot fill factor.
k_{spindle}	spindle pitch.
l_{Cu}	average conductor lenght of one turn of the stator winding.
L_{d}	direct axis inductance.
l_{Fe}	active length, core length.
L_{h}	main inductance.
L_{q}	quadrature axis inductance.
L_{R}	self inductance rotor winding.
$L_{\mathrm{R}\sigma}$	leakage inductance rotor.
l_{RHJ}	average length of magnetic field line in rotor yoke.
L_{S}	self inductance stator winding.
$L_{\mathrm{S}\sigma}$	leakage inductance stator.
l_{SHJ}	average length of magnetic field line in stator yoke.
l_{stream}	streaming lenght.
M	maximal mutual inductance between stator and rotor.
m	number of phases.
μ_0	absolute permeability.
μ_{r}	relative permeability.
n	rotational speed motor.
N_{bar}	number of rotor bars.
N_{S}	number of stator slots.
Nu	Nusselt number.

ω_{mech}	mechanical angular frequency.
ω_{R}	electrical angular frequency in rotor reference frame.
ω_{S}	stator voltage angular frequency.
p	number of pole pairs.
P_{Cu}	copper losses, resistive losses.
$\ddot{\varphi}$	angular acceleration.
Φ_{SSP}	magnetic flux entering the stator slot pitch.
Φ_{J}	yoke magnetic flux.
Φ_{p}	magnetic flux per pole.
ψ_{R}	phase angle of rotor current.
$\Phi_{\text{S slot}}$	stator slot magnetic flux.
$\Phi_{\text{S tooth}}$	stator tooth magnetic flux.
Pr	Prandtl number.
Ψ_{d}	flux in direct axis.
Ψ_{h}	main flux linkage.
Ψ_{q}	flux in quadrature axis.
Ψ_{R}	flux linkage of rotor.
Ψ_{S}	flux linkage of stator.
q	number of slots per pole.
$\dot{Q}$	heat flow.
Ra	Rayleigh number.
ρ_{Cu}	specific resistance of copper.
R_{Ph}	ohmic resistance of one phase.
R_{R}	rotor ohmic resistance.
R_{S}	stator ohmic resistance.
R_{therm}	thermal resistance of the heat conduction.
s	slip.
T	torque.
t	time.
T_{amb}	ambient temperature.
τ_{p}	pole pitch.
τ_{RSP}	rotor slot pitch.
τ_{SSP}	stator slot pitch.
T_{fric}	friction torque of the system.
Θ	current linkage.
$\hat{\Theta}$	peak value of current linkage.
T_{load}	load torque.
T_{mech}	mechanical torque.
T_{motor}	motor torque.
T_{winding}	winding temperature.
$\hat{U}_{\delta\,\text{slot tooth}}$	peak value magnetic voltage of slot-tooth layer.
u_{d}	direct axis voltage.
U_{DC}	intermediate circuit voltage, DC link voltage.

$\hat{U}_\delta$	peak value magnetic voltage of air gap.
$\hat{U}_\mathrm{p}$	peak value magnetic voltage of a pole pair.
u_q	quadrature axis voltage.
u_R	rotor voltage.
$\hat{U}_\mathrm{RJ}$	peak value magnetic voltage of rotor yoke.
$\hat{U}_\mathrm{RT}$	peak value magnetic voltage of rotor teeth.
$\hat{U}_\mathrm{S}$	peak value of stator voltage, steady state.
u_S	stator voltage.
$\hat{U}_\mathrm{SJ}$	peak value magnetic voltage of stator yoke.
$\hat{U}_\mathrm{ST}$	peak value magnetic voltage of stator teeth.
w_barrier	width of flux barrier.
w_bridge	width of flux bridge.
w_path	width of flux path.
w_slot	number of conducters in a slot.
w_str	number of turns of one phase in series.
x	linear coordinate.
ξ	winding factor.
x_max	maximum linear adjusting range of the actuator.
α_heat	heat-transfer coefficient.
β_exp	thermal expansion coefficient.
ϵ	emissivity coefficient.
λ_fluid	thermal conductivity of the fluid (air).
ν_kin	kinematic viscosity.
σ_B	Stefan - Boltzmann constant.